# MODELLING AND SIMULATION OF SURFACE PLASMONIC RESONANCE IN PHOTONIC CRYSTAL FIBER

**RIFAT AHMMED AONI**

**FACULTY OF ENGINEERING
UNIVERSITY OF MALAYA
KUALA LUMPUR**

**2015**

# MODELLING AND SIMULATION OF SURFACE PLASMONIC RESONANCE IN PHOTONIC CRYSTAL FIBER

## RIFAT AHMMED AONI

## DESSERTATION SUBMITTED IN FULFILMENT OF THE REQUIREMENTS FOR THE DEGREE OF MASTER OF ENGINEERING SCIENCE

## FACULTY OF ENGINEERING
## UNIVERSITY OF MALAYA
## KUALA LUMPUR

## 2015

# ABSTRACT

Surface Plasmon Resonance (SPR) refers to the coupling between the electromagnetic wave and the surface plasmonic wave (SPW) on the surface between a metal and a dielectric medium. Since last decade, the SPR behavior is widely applied in prism based SPR sensor, which is bulky and not suitable for remote monitoring applications. To overcome this limitation, photonic crystal fiber (PCF) based SPR sensor had attained great attention with the advantages of easily launching light through the fiber, small-size and design flexibility. To establish the SPR phenomena, metal deposition is necessary. Nowadays, in most of the PCF-SPR sensors, metal is selectively deposited inside the air-holes with numerous selective metallic and liquid channels, which made fabrication of such sensors impractical or very challenging.

In this dissertation, four different PCF-SPR sensors are introduced with relatively high or comparable sensing performance. The proposed sensors are numerically investigated using the commercial Multiphysics COMSOL software. First study presents the PCF-SPR sensor with only one graphene-silver deposited channel and two high refractive index (RI) liquid channels. It shows the amplitude sensitivity as high as 418 $RIU^{-1}$ and the wavelength interrogation sensitivity of 3000 nm/RIU. In the second study, focusing on the metal deposition problem, a flat structure PCF-SPR sensor is developed where, the metal layer is deposited outside the fiber structure and the sensor will perform the external sensing scheme to detect the analytes. The proposed flat SPR sensor enhances the evanescent field resulting the amplitude sensitivity as high as 820 $RIU^{-1}$ and the remarkable wavelength interrogation sensitivity of 23,000 nm/RIU. In the third study, a practically simple PCF SPR sensor is proposed. The metallic layer and sensing layer are placed outside the fiber structure which makes the sensor configuration simple and the analyte detection process easier. The proposed sensor shows the amplitude and wavelength interrogation sensitivity of 320 $RIU^{-1}$ and 4000 nm/RIU, respectively. In the

last work, copper is utilized in PCF SPR sensor for the first time due to its long-term stable sensing performance; and graphene is used to prevent copper oxidation and enhance the sensor performance. Similar to the third design, here the metallic layer and sensing layer are positioned outside the fiber structure resulting easy detection mechanism. It shows the wavelength interrogation sensitivity of 2000 nm/RIU with the sensor resolution of $5\times10^{-5}$ RIU. Due to the promising sensitivity, the proposed sensors would be potential candidates for chemical, bio-chemical, organic chemical and organic molecule analytes detection with realizable structure.

# ABSTRAK

Resonan Plasmon Permukaan (SPR) merujuk kepada gandingan antara gelombang elektromagnetik dan gelombang plasmonic permukaan (SPW) di antara permukaan logam dan medium dielektrik. Sejak sedekad lalu, ciri SPR digunakan secara meluas dalam sensor SPR berdasarkan prisma, di mana saiznya sangat besar dan tidak sesuai untuk aplikasi pemantauan jarak jauh. Untuk mengatasi limitasi ini, sensor SPR berasaskan gentian kristal fotonik (PCF) mendapat banyak perhatian dengan kelebihannya seperti kemudahan pelancaran cahaya melalui gentian, saiz yang kecil serta reka bentuk yang fleksibel. Untuk mewujudkan fenomena SPR, pemendapan logam ke atas permukaan gentian adalah diperlukan. Pada masa kini, di kalangan sensor PCF-SPR, logam disalut ke dalam udara-lubang tertentu dengan pelbagai pilihan logam dan saluran cecair, di mana fabrikasi pengesan ini adalah tidak praktikal atau sangat mencabar.

Dalam disertasi ini, empat jenis sensor PCF-SPR yang berbeza diperkenalkan dengan kurang kesukaran dalam fabrikasi dan prestasi pengesanan yang setanding atau lebih tinggi. Sensor yang dicadangkan dikaji dengan kaedah berangkadengan menggunakan perisian komersial Multiphysics COMSOL. Kajian pertama membentangkan sensor PCF-SPR dengan hanya satu saluran graphene-perak dan dua saluran cecair indeks biasan yang tinggi (RI) Ia menunjukkan kepekaan amplitud setinggi 418 RIU$^{-1}$ dan sensitiviti pembacaan panjang gelombang 3000 nm/RIU. Dalam kajian kedua, untuk mengatasi masalah pemendapan logam, sensor PCF-SPR struktur rata dibangunkan di mana, lapisan logam disalut di luar struktur gentian dan melaksanakan pengesanan luar untuk mengesan analit. Sensor SPR rata meningkatkan medan laluan cepat dan meningkatkan kepekaan amplitud setinggi 820 RIU$^{-1}$ dan kepekaan pembacaan panjang gelombang setinggi 23,000 nm/RIU. Dalam kajian ketiga, sensor PCF SPR mudah yang praktikal dicadangkan. Lapisan logam dan lapisan pengesanan diletakkan di luar struktur serat memudahkan konfigurasi sensor dan proses pengesanan analit. Sensor yang dicadangkan masing-masing menunjukkan kepekaan amplitud dan pembacaan panjang gelombang 320 RIU$^{-1}$ dan 4000 nm/RIU. Dalam kajian keempat, tembaga digunakan dalam sensor PCF SPR oleh kerana prestasi jangka panjang pengesanan yang stabil; graphene digunakan untuk mencegah pengoksidaan tembaga dan juga meningkatkan prestasi pengesanan. Untuk memudahkan process mekanisme pengesanan, lapisan logam dan lapisan pengesanan ini diletakkan pada luar struktur serat. Dengan ini, ia menunjukkan kepekaan gelombang panjang sentinggi 2000 nm/RIU dengan resolusi $5\times10^{-5}$ RIU. Oleh kerana kepekaan yang menjanjikan, sensor yang dicadangkan mempunyai potensi tinggi

dalam pengesanan kimia, bio-kimia, kimia organik dan molekul organik analytes dengan struktur yang boleh direalisasikan.

# ACKNOWLEDGEMENTS

# TABLE OF CONTENTS

# LIST OF FIGURES

# LIST OF TABLES

# LIST OF ABBREVIATIONS

| | | |
|---|---|---|
| PCF | : | Photonic Crystal Fiber |
| MCFF | : | Multi-Core Flat Fiber |
| SPR | : | Surface Plasmon Resonance |
| SPW | : | Surface Plasmon Wave |
| SP | : | Surface Plasmon |
| SPP | : | Surface Plasmon Polariton |
| RIU | : | Refractive Index Unit |
| RI | : | Refractive Index |
| CVD | : | Chemical Vapor Deposition |
| NIR | : | Near-infrared Region |
| EMI | : | Electromagnetic Interference |
| TIR | : | Total Internal Reflection |
| SEM | : | Scanning Electron Microscopy |
| TE | : | Transverse Electric |
| TM | : | Transverse Magnetic |
| FEM | : | Finite Element Method |
| PWEM | : | Plane Wave Expansion Method |
| MM | : | Multipole Method |
| EME | : | Eigenmode Expansion Method |
| PML | : | Perfectly Matched Layer |
| PEC | : | Perfectly Electric Conductor |
| PMC | : | Perfectly Magnetic Conductor |

# CHAPTER 1: INTRODUCTION

## 1.1 Introduction

Biomolecular interactions are the key factors of drug-discovery technique. By analyzing the molecular interactions, it is possible to diagnose the facts about the diseases. Generally, biosensors are used to analyze the molecular interactions (Cooper, 2002; Fang, 2006). Since last few decades, optical biosensors are widely used to analyze the molecular interactions. Due to advance optical instrumentations, optical sensors have attracted much attention for its easy instant detection capability. In the late 1980s, first optical biosensor had been commercialized (Cooper, 2002; Myszka, 1999). Optical sensors are related to the light matters where the light intensity or electromagnetic fields have changed due to the presence of samples. A sophisticated device that converts the light rays into electrical signals which can detect the change and response of ambient condition or can measure the intensity of electromagnetic waves called an optical sensor. A number of optical sensor techniques are available such as micro-ring resonator, surface plasmon resonance, resonant mirrors, photoluminescence and evanescent wave absorption spectroscopy (Fang, 2006; Jiří Homola, 2003; Sharma, Jha, & Gupta, 2007; Yuan et al., 2014). Apart from all sensing techniques, surface plasmon resonance sensor has been given great attention due to its high sensitive nature and wide range of applications. SPR effects are not limited to sensing applications. Researchers also found the applications in optoelectronics devices including optical tunable filter (Kajenski, 1997; Wang, 1995), modulators (Schildkraut, 1988; Sincerbox & Gordon, 1981), SPR image (Su, Chen, & Yeh, 2005), thin-film thickness monitor (Akimoto, Sasaki, Ikebukuro, & Karube, 1999; Johnston, Karlsen, Jung, & Yee, 1995), liquid sensors (Cahill, Johnston, & Yee, 1997; Y.-C. Cheng, Su, & Liou, 2000), gas sensors (Ashwell & Roberts, 1996; Niggemann et al., 1996) and biosensors (Berger & Greve, 2000; Stemmler, Brecht, & Gauglitz, 1999).

Surface plasmons (SPs) phenomena was first theoretically introduced by Ritchie (1957). Later, based on SPs idea using the attenuated total reflection (ATR) method prism based SPR Otto configuration was reported by Otto (1968), where the prism and plasmonic metal layer were separated by a dielectric (sample) medium. This sensing technique was quiet difficult as its need to maintain a finite gap between the prism and metallic layer. Updating the Otto configuration, Kretschmann setup was introduced where the prism and metallic layer are attached together (KretschmannE, 1968). To date, Kretschmann and Otto configuration are much popular techniques to generate the surface plasmon waves (SPWs). In 1983, for the first time SPR sensor had been practically demonstrated for chemical and biological applications (Liedberg, Nylander, & Lunström, 1983).

While the p-polarization or transverse magnetic (TM) incident light frequency of incoming photons and surface electrons are matched resulting the free electrons of the metal surface start to resonate and finally surface plasmon wave (SPW) is generated which propagates along the metal-dielectric interface. SPR sensors require a metallic component carries large amount of free electrons. These free electrons provide the real part of a negative permittivity which are essential for plasmonic materials. Conventional prism based Kretschmann set-up is widely used for SPR sensor where the p-polarization or transverse magnetic light is incident on a prism coated with plasmonic materials (Au, Ag, Cu, etc.) and generate the surface plasmon polaritons (SPP) wave that propagate along the surface (Gupta & Verma, 2009). A change in dielectric refractive index causes a change in propagation constant of the surface plasmon (SP) mode. This change consequently alters the coupling condition of the light wave and the SP wave, and the changes can be monitored from one of the characteristics of optical wave interacting with the SP mode (Jiri Homola, 2008). Based on the characteristic, these sensors can be classified with coupling angle, coupling wavelength, phase, intensity, or polarization change as presented in Figure 1.1 (Jirí Homola, 2006).

2
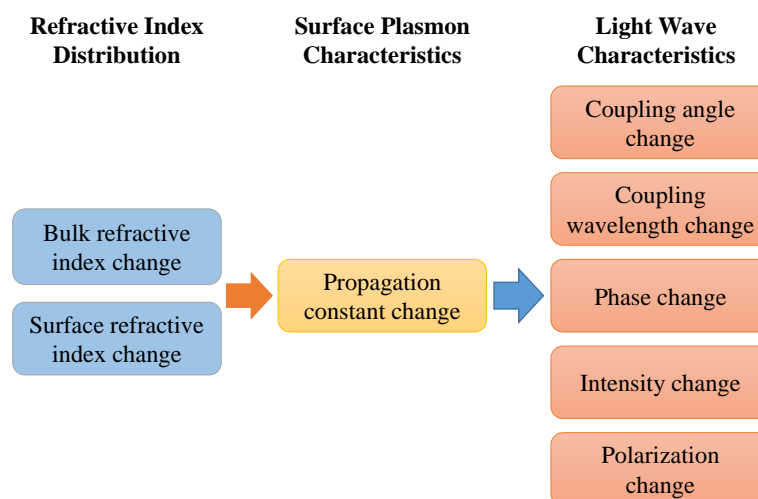
**Figure 1.1:** Variety classifications of the surface plasmon resonance sensors (Jirí Homola, 2006).

Although prism based SPR sensor (Kretschmann set-up) performance is robust, its structural configuration is bulky due to many required optical and mechanical components therefore not suitable for remote sensing (Gupta & Verma, 2009). In 1993, optical fiber based SPR sensor was introduced for chemical sensing (Jorgenson & Yee, 1993). Various optical fiber based SPR sensors have been reported due to their applications as well as enhanced sensing range and the sensing accuracy. In last decades, microstructured optical fiber (MOF) based SPR sensor has been reported for the first time (A Hassani & Skorobogatiy, 2006). Photonic crystal fiber (PCF) based SPR sensing technique is considered as a possible route to sensor miniaturization. PCF has been proven as a good replacement of prism. By harnessing its advantages such as small size, easier light launching, single mode propagation and ability in controlling evanescent field penetration, PCF turns out to be a promising candidate for SPR sensor.

## 1.2    Problem Statements

To date, numerous PCF SPR sensors have been reported. Most of the reported sensors structure are difficult to be fabricated due to selective coating of metal layers and liquid infiltration inside the air-hole surface (Dash & Jha, 2014b; Gao, Guan, Wen, Zhong, &

3

Yuan, 2014; Qin, Li, Yao, Xin, & Xue, 2014; Shuai, Xia, & Liu, 2012). Additionally, these reported sensors performance are observed by following the inside sensing operation. Recently, to reduce the metal coating problem, D-shaped PCF SPR sensors were demonstrated to eliminate the liquid infiltration and metal coating problems. However, accurate polishing effort is required to precisely remove a predetermined portion of the PCF to produce the D-shape structure (Dash & Jha, 2015a; Shi et al., 2015; Tan, Li, Chen, & Fan, 2014; Tian, Lu, Chen, Lv, & Liu, 2012). Several PCF SPR sensors were reported where the metallic and sensing layer are placed outside the fiber structure to simplify the sensor configuration. However, to control the light propagation in specific direction these sensors introduced elliptical air-holes (Akowuah et al., 2012; Otupiri, Akowuah, & Haxha, 2015), and also several small air-holes are selectively placed in the specific position which makes the sensors structure complex in terms of fabrication (Dash & Jha, 2014a; Otupiri et al., 2014). To sum up, the reported PCF SPR sensors following limitations are observed:

1. Selectively liquid infiltration inside the micron scale air-holes.

2. Selectively plasmonic metal coating inside the air-holes surface.

3. Inside sensing operation.

## 1.3 Research Objectives

The aims of the study are to design a simple PCF based SPR sensor and numerically investigate the characteristics and behaviors of the proposed sensors. In particular, the objectives of the research are follows:

(i) To design a simple PCF based SPR sensor to solve the selectively metal coating, liquid infiltration and inside sensing problems.

(ii) To analyze performance of the proposed sensors based on wavelength and amplitude interrogation method.

## 1.4    Scope of Study

This study is fully based on simulation works. All proposed sensors are investigated with the commercial COMSOL software and performances are optimized with wavelength and amplitude interrogation methods. The accuracy of the simulation methods are verified with the reported literature before analyzing the proposed sensors. Proposed PCF SPR sensors are developed by considering the selectively metal coating, liquid infiltration and internal sensing problems.

## 1.5    Dissertation Outline

This dissertation report is organized into eight chapters. A brief summary of the next seven chapters are given in this section.

Chapter 2 gives an overview of surface plasmon resonance, solution of Maxwell's eigenvalue problem and the conventional SPR sensing techniques. Drawbacks of these conventional techniques and the solutions are reviewed in this chapter. PCF SPR sensing schemes are discussed with the details of advantages and sensing technique. A details clarification of PCF structure implementation as well as combination of PCF SPR for sensing are specified. Accuracy of the numerical methods are described and finally reproduce the results which have already been reported in well-reputed journal to validate the following method. A brief overview of reported PCF SPR sensors are given for the actual picture of this sensing scheme. Finally, importance of plasmonic materials are discussed.

In Chapter 3, silver-graphene coated PCF SPR sensor is introduced. A brief technical review is carried out with the reported works. Possible methods are described for the realization of the proposed sensor. Sensor performance is investigated based on the wavelength interrogation method and amplitude interrogation method.

In Chapter 4, flat fiber based SPR sensor is introduced where metallic layer and sensing layer are placed top of the flat surface to reduce the sensing complexity. A brief

technical review is outlined with details sensing mechanism. Sensor performance is investigated based on sensitivity, sensor resolution, detection accuracy and linearity.

In Chapter 5, a simple PCF SPR sensor is proposed where the metallic layer and sensing layer are placed outside the fiber structure. Sensor performance is investigated by wavelength and amplitude interrogation method. Additionally, fabrication tolerance of the proposed sensor is investigated.

In Chapter 6, Copper-Graphene based PCF SPR sensor is introduced. A short description is given by critically analyse the plasmonic materials. Sensor performance is observed by wavelength and amplitude interrogation method.

Finally, Chapter 7 presents research conclusion and other proposed future works.

# CHAPTER 2:  LITERATURE REVIEW AND TECHNICAL BACKGROUND

## 2.1     Introduction

Surface plasmon resonance is a new technology which involves and fascinating the light-matters interaction involved at a metal-dielectric interface. In this chapter, fundamental of surface plasmons and the plasmon excitation condition is outlined. Working principle of the conventional SPR sensors are described in details and their drawbacks are encountered. Advantages of PCF over prism for SPR sensing are labeled and PCF SPR sensors reported in the literatures are reviewed critically. In the following, proposed PCF SPR sensors are numerically investigated. Maxwell's equations are derived to formulate the eigenvalue problem for PCFs. Different numerical methods are studied for the mode propagation analysis. A detail overview on PCF structure implementation is given. Additionally, convergence test for the simulated structure is described which enhance the result accuracy; and finally, verify the simulation method. The detail of every PCF SPR sensor structural design developed in this study are demonstrated in the results chapters, Chapter 3 to 6, together with the specification characteristics of the proposed sensor.

## 2.2     Surface Plasmons and Surface Plasmon Resonance

### 2.2.1   Surface Plasmons

Inside a conductor (metal) there are a lot of free electrons and an assembly of the electron can be considered as plasma particle. At the same time there are equal numbers of positive charged ions from lattice so the total charge density in the conductor is zero. Now if an external field is applied then the electrons will be moving towards the positive

region and at the same time the positive ion will be moving as opposite to the electrons as shown in Figure 2.1.
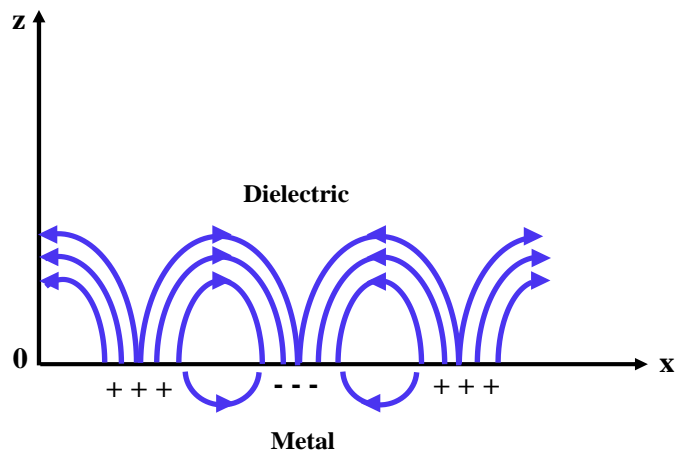


**Figure** 2.1: Plasmon oscillation in the metal (Jirí Homola, 2006).

Due to this moving mechanism a longitudinal oscillation will be introduced in the conductor and this is known as the plasma oscillation which is known as surface plasmons (Jiří Homola, 2003; Khan, 2012).

### 2.2.2 Surface Plasmon Resonance

To support the surface plasmons, a conductor and dielectric interface is required. In general a metal and dielectric interface is used to support the surface plasmon oscillation. Due to this oscillation and a certain resonance condition, surface plasmon wave is generate which propagate along the surface (Figure 2.2). This surface plasmon is only TM polarized electromagnetic field because for TE polarized case there is no solution of the Maxwell's equation. So for surface plasmon wave only the transverse magnetic (TM) polarized electric field exists. This wave is decayed exponentially in the metal. This Surface Plasmon Wave (SPW) is characterized by the propagation constant as (Jiří Homola, 2003; Sharma et al., 2007);

$$\beta = \frac{\omega}{c} \sqrt{\frac{\varepsilon_M \varepsilon_D}{\varepsilon_M + \varepsilon_D}} \qquad (2.1)$$

where $\omega$ is the angular frequency, $c$ is the speed of light in vacuum and $\varepsilon_M$, and $\varepsilon_D$ are the dielectric permittivity's of metal and dielectric medium, respectively.

According to the above equations, property of the SPW is dependent on the property of two materials i.e. the metal and dielectric media.
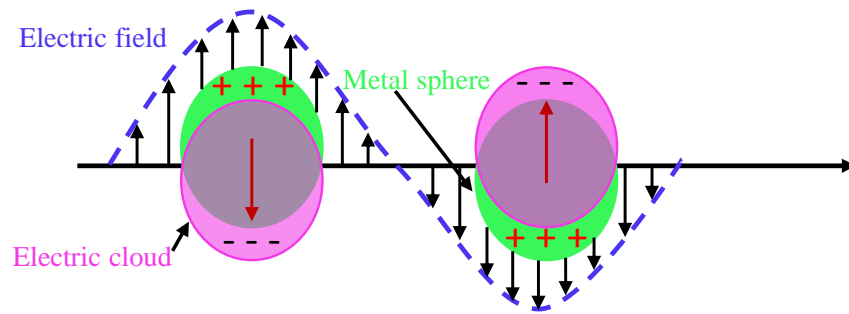


**Figure 2.2:** Localized SPR when field (light) interacts with the plasmons (Jirí Homola, 2006).

Now to create the surface plasmon oscillation need to excite the electrons in the conductor. So, impose the light (EM field) is necessary on the surface. We know that the electrical permittivity for the conductor (metal) is negative and the electrical permittivity for the dielectric is positive. In the dielectric medium the propagation constant (maximum) can be written as (Emmerich; Sharma et al., 2007),

$$\beta = \frac{\omega}{c}\sqrt{\varepsilon_S} \tag{2.2}$$

So it is stated that the propagation constant for surface plasmon wave is higher than the propagation constant of light in the dielectric medium. As a result, surface plasmon can't be excited with the normal light; it requires the light with extra momentum or energy with the same polarization state as the surface plasmon wave. Moreover, the propagation constant should be matched with the surface plasmon wave.

## 2.3    The Maxwell's eigenvalue problem

Light can be observed as two aspects: it is an electromagnetic wave and it has particle like property. Electromagnetic wave propagation in PCFs are based on the Maxwell's equations (D. K. Cheng, 1989). The analysis of the cylindrical coordinate system is given below:

$$\nabla.B = 0 \tag{2.3}$$

$$\nabla.D = \rho \tag{2.4}$$

$$\nabla \times E + \frac{\partial B}{\partial t} = 0 \tag{2.5}$$

$$\nabla \times H + \frac{\partial D}{\partial t} = j \tag{2.6}$$

Here, the electric and magnetic fields are represented by $E$ and $H$, respectively. Electric and magnetic flux densities are represented by $D$ and $B$, respectively.

The flux densities can be expressed as,

$$D(r) = \varepsilon_0 \varepsilon(r) E(r) \tag{2.7}$$

$$B(r) = \mu_0 \mu(r) H(r) \tag{2.8}$$

Here, $\varepsilon(r)$ and $\mu(r)$ are known as the relative permittivity and permeability of the medium and these properties are dimensionless. In contrast, $\varepsilon_0$ and $\mu_0$ are the relative permittivity and permeability in a free space where the values are $\varepsilon_0 = 8.854 \times 10^{-12}$ ($F/m$) and $\mu_0 = 4\pi \times 10^{-7}$ ($H/m$).

Generally, permeability, $\mu(r)$ of the dielectric material is close to unity resulting the Eq. 2.8 can be written as $B(r) = \mu_0 H(r)$. The imaginary part of $\varepsilon$ expresses the material related losses but, for the low loss dielectric such as Silica, it is considered purely real. By assuming in a medium there have no light source, free charges or current in the system, so $\rho = 0$ and $J = 0$. By considering all assumptions, Eqs. 3.1-3.4 can be rewritten as:

$$\nabla.H(r,t) = 0 \tag{2.9}$$

$$\nabla \cdot [\varepsilon(r)E(r,t)] = 0 \tag{2.10}$$

$$\nabla \cdot E(r,t) + \mu_0 \frac{\partial H(r,t)}{\partial t} = 0 \tag{2.11}$$

$$\nabla \cdot H(r,t) + \varepsilon_0 \varepsilon(r) \frac{\partial H(r,t)}{\partial t} = 0 \tag{2.12}$$

The linearity of Eqs. 2.9-2.12 allow for the Fourier analysis. Any general solution can be expressed as the combination of a set of harmonic modes at a different specific optical frequencies. Temporal dependency can be removed from the original problem such as,

$$H(r,t) = \mathrm{Re}\{H(r)e^{jwt}\} \tag{2.13}$$

$$E(r,t) = \mathrm{Re}\{E(r)e^{jwt}\} \tag{2.14}$$

By the substitution of Eqs. 2.9-2.12 into Eqs. 2.13-2.14, following two divergence and two curl equations are obtained:

$$\nabla \cdot H(r) = 0 \tag{2.15}$$

$$\nabla \cdot [\varepsilon(r)E(r)] = 0 \tag{2.16}$$

$$\nabla \times E(r) - j\omega\mu_0 H(r) = 0 \tag{2.17}$$

$$\nabla \times H(r) + j\omega\varepsilon_0\varepsilon(r)H(r) = 0 \tag{2.18}$$

By combining two curl Eqs. 2.17 and 2.18, the master equation is obtain where the only unknown parameter is *H(r)*,

$$\nabla \times \left( \frac{1}{\varepsilon(r)} \nabla \times H(r) \right) = \left( \frac{\omega}{c} \right)^2 H(r) \tag{2.19}$$

In a system if the *ε(r)* is known then by following this master equation *H(r)* can be obtained. Considering the z-invariant, system can be expressed as,

$$H(r) = H(x,y)e^{-j\beta z} \tag{2.20}$$

Here, along the *z*-direction propagation constant is *β*, Eigenvalue problem can be solved by using the eigenvalue of *β* or *ω*. Considering the medium is homogenous such as *ε(r, ω)* =

$\varepsilon(\omega)$, the master equation Eq. 2.19 becomes a well-known scalar Helmholtz equation which is able to analytically solve the single coordinate either cylindrical or cartesian coordinates. Generally, the step index fiber, waveguide slab (Snyder & Love, 2012) and Bragg fiber (Yeh, Yariv, & Hong, 1977) and structure could be analytically solved by the master equation Eq. 2.19 whereas PCFs analytical expression of boundary condition is quite complex due to the spatial refractive index profile resulting the analytical solution is not possible to investigate the optical properties of the PCFs. Finally, to investigate the optical properties of PCFs structures, numerical methods need to be applied to solve the master Eq. 2.19.

## 2.4    Overview of Numerical Methods

A lot of numerical works already been carried out for the PCFs simulation. To investigate the PCFs properties, several numerical methods are available. Accuracy of these numerical methods are depends on some basic properties as describe below:

- ✓ **Full vector formulation:** Full vector formulation allows the study of fibers with arbitrary structural parameters as well as arbitrary refractive index contrast. Based on the applications, structural parameters can be changed and controlled light guiding.

- ✓ **Direct insertion:** It facilitates for getting the results more accurate and comparable with the experimental result. It permits the dependency on wavelength with respect to refractive index. This property is important for dispersion and confinement loss calculation.

- ✓ **Confinement loss (CL) measurement:** Confinement loss measurement is one of the most important property among all other PCFs properties. PCFs applications are related to the light matters. If the loss is high then the launching light will disappear immediately. It will not able to pass through the fiber as a result, it will not be applicable for any of the applications.

✓ **Capacity to calculate the arbitrary cross-section:** It is an important criteria which allows to do the simulation and characterization using the fabricated scanning electron microscopy (SEM) images. It helps to compare the experimental and simulation results.

✓ **Symmetry exploitation:** Taking account the symmetrical structure advantages, this property allows to make the simulation faster. Only one part of the symmetrical structure is able to provide the accurate result which makes the computation faster and reduce the high configuration computer's requirements.

For the following research works, mode guiding property of the PCFs is needed. Considering the mode solving property several well-known methods are available such as plane wave expansion method (PWEM), multipole method (MM), eigenmode expansion method (EME) and finite element method (FEM).

PWEM is based on the frequency domain which conveys the eigenvalue problem from the Maxwell's equations (Johnson & Joannopoulos, 2001). The PWEM method is useful for the periodic photonic crystal structure analysis. Using this method tuning the air-filling fraction is possible which helps to control the propagation. Moreover, to insert the fabricated SEM images and analysis the properties of these images are possible. However, the main drawback of this method is inefficient wavelength dependency with respect to effective index which gives the false result of dispersion as well as confinement loss (Kotynski, Antkowiak, Berghmans, Thienpont, & Panajotov, 2005; Pearce, Hedley, & Bird, 2005). Dispersion and confinement loss are the important properties of the PCF.

MM is based on the mathematical series of a function which depends on angles. This method is able to provide the propagation constant of real and imaginary part of PCFs which helps to calculate the dispersion and confinement loss properties (Botten et al., 2005). The main problem of this method is, it cannot take the input circular structure of SEM image resulting the SEM image of PCFs cannot be analyzed using this method.

Moreover, this method cannot take the advantages of symmetrical structure. As a result, partial part computational cannot give the accurate result (White et al., 2002).

EME is based on the frequency domain. It decomposes the electric field and make a set of local eigenmodes which is exist in the cross-section of waveguide. EME algorithm is bi-directional even it could be worked as omnidirectional if the adequate modes are used. It is full-vectorial algorithm which facilitate the parameter variation as well the effective index contrast variation. This method is useful to simulate the propagation of twisted waveguide structure and it can simulate even 90 degree angle of propagation. This method allows taking the advantages of symmetrical structure which reduces the computational time. Using this EME method with interactive techniques nonlinear problems can be modeled but this method is limited to the linear problems (Gallagher & Felici, 2003).

FEM is a technique which is able to find the solution of partial differential equation (PDE) to handle the boundary-value problem (Koshiba, 1992). The main advantage of this method is that, it divides the computational area in a small finite region such as triangles, rectangles etc., which allows to precisely analyze the structure. This method allows to change the air-fill fraction and able to calculate the complex and real effective index of the structure which gives the approximation of PCFs dispersion and propagation behavior. Additionally, it is able to import and analyze the SEM image of fabricated PCFs (Koshiba & Saitoh, 2001). In this research work, FEM based commercial COMSOL software is used to develop the sensors as well as analyzing the sensor performance.
Table 2.1 shows a summary comparison between the PWEM, MM, EME and FEM methods.

**Table 2.1:** Comparison among the numerical methods for the study of MOFs.

| Properties | PWEM | MM | EME | FEM |
|---|---|---|---|---|
| Fully vectorial | √ | √ | √ | √ |
| Material dispersion | × | √ | √ | √ |
| CL calculation | × | √ | × | √ |
| Arbitrary cross-section | √ | × | √ | √ |
| Symmetry exploitation | × | × | √ | √ |
| References | (Johnson & Joannopoulos, 2001; Pearce et al., 2005) | (White et al., 2002) | (Gallagher & Felici, 2003) | (Koshiba, 1992; Koshiba & Saitoh, 2001) |

## 2.5 Conventional Sensing Techniques of Surface Plasmon Resonance

Conventional SPR sensors are utilized using prism. Prism is used to concentrate the incident light. When the p-polarized or TM light is incident on prism-metal dielectric interface and the reflectance is measured as a function of angle of incidence, a sharp dip is obtained at a particular angle called the resonance angle. The unknown analyte (analyte is a substance or chemical component that is undergoing analysis) could be detected by measuring the shift of resonance angle. This method is called the angular interrogation method. Based on this sensing mechanism two sensing methods are developed, such as (1) Otto-configuration, and (2) Kretschmann-configuration.

### 2.5.1 Otto-configuration for SPR sensing

In 1968, Otto introduced a prism coupling technique where the prism and metal were placed in a gap and the gap was filled with the sample liquid (Figure 2.3) (Otto, 1968). The sample liquid refractive index should be smaller than the prism. Otto configuration is followed the attenuated total reflection (ATR) method. When the p-polarization light is incident on the prism-dielectric interface it produces the evanescent wave (EW), at a

15

particular angle this evanescent wave excite the surface plasmon wave on the metal-dielectric interface.
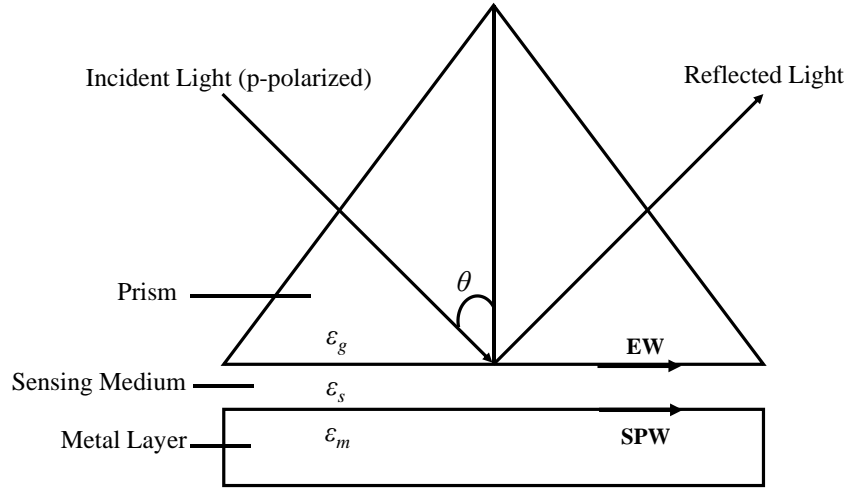


**Figure 2.3:** Otto-configuration for SPR sensor (Jirí Homola, 2006).

At a particular angle wave-vector of evanescent wave and surface plasmon waves are matched together, at this angle a dip in reflected wave intensity can be observed. At this condition, energy transfer from the EW to SPW. At the prism-dielectric interface wave vector $K_{ev}$ of the evanescent field is given as,

$$k_{ev} = \frac{\omega}{c} \sqrt{\varepsilon_g} \sin \theta \qquad (2.21)$$

where $\omega$ is the frequency of incident light, $c$ is the speed of light, $\varepsilon_g$ is the dielectric constant of the material of the prism and the incident angle is $\theta$.

Otto-configuration has been found interesting for studying single crystal metal surfaces and absorption on them. To utilize this prism-coupling, prism and metal layer should be placed with a finite gap which is a drawback of Otto-configuration. By solving this problem a modified configuration is introduced which is known as Kretschmann-configuration.

### 2.5.2 Kretschmann-configuration for SPR sensing

In 1968, Kretschmann-configuration had been introduced where the prism and metal layer was attached together (KretschmannE, 1968), between the prism and metal layer there was no gap; sample liquids were placed outside the metal layer (Figure 2.4).
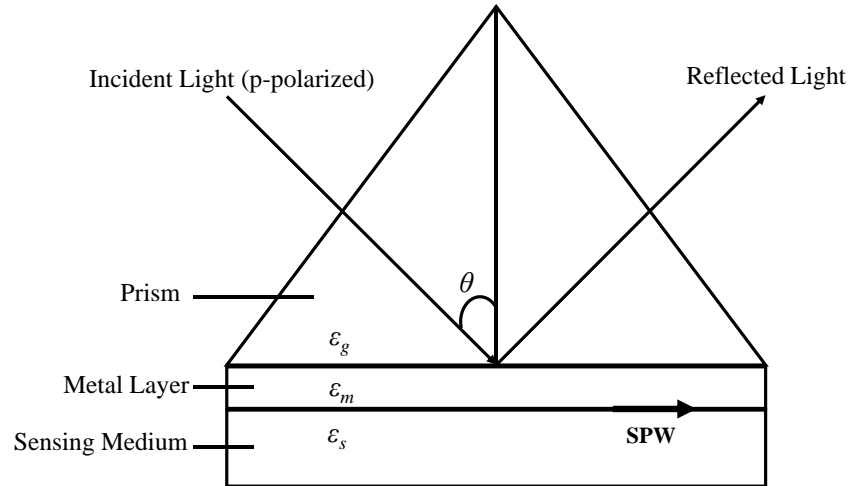


**Figure 2.4:** Kretschmann-configuration for SPR sensor (Jirí Homola, 2006).

In this method, surface plasmons also excited by the evanescent wave like as Otto-configuration. At a specific angle when the wave vector of evanescent wave and the surface plasmon wave matched then the resonance was occurred, at this resonance condition a dip reflected light intensity was also appeared. Incident light wave vector which travelling along the prism surface is $k_g$ and the evanescent field wave vector, $k_{ev}$ is defined as;

$$k_{ev} = k_g \sin \theta = \frac{\omega}{c} \sqrt{\varepsilon_g} \sin \theta \tag{2.22}$$

The main drawback of Kretschmann-configuration is metal layer should be parallel to prism surface, thereby, this technique is not applicable for curved surfaces such as a metal cylinder or metal sphere. This is one of the reasons why this configuration has not been widely used (Knoll, 1998).

### 2.5.3 Problems Encountered

Otto and Kretschmann configurations are well developed for SPR sensor. Their practical implementation are simple due to outer metal coating and also the plain surface which is quite straight-forwat for metal deposition. However, prism based SPR sensor has a lot of drawbacks such as it is bulky in size and it has a various optical and mechnical moving parts which limits optimization and commercialization in a large scale (Dash & Jha, 2014b). Due to its optical and mechanical moving parts, it is not suitable moving the setup configuration outside the laboratory to detect the sample, which limits the commercialization. Additionally, prism based SPR sensor couldn't applicable for remote sensing applications (Gupta & Verma, 2009).

### 2.6 Prism based SPR Sensing Mechanism

As described in previous section, prism based SPR sensor resonance is occurred when the propagation constant of evanescent wave and the propagation constant of the surface plasmon wave are the same. According to the Kretschmann-setup propagation constant of evanescent wave is,

$$k_{ev} = k_g \sin\theta = \frac{\omega}{c}\sqrt{\varepsilon_g}\sin\theta \tag{2.23}$$

Additionally, based on the Maxwell's equation propagation constant, $k_{sp}$ of surface plasmon waves which propagate along the metal-dielectric interface can be expressed as (Jie, Dakai, & Zhenwu, 2007);

$$k_{sp} = \frac{\omega}{c}\sqrt{\frac{\varepsilon_m\varepsilon_s}{\varepsilon_m + \varepsilon_s}} \tag{2.24}$$

where $\varepsilon_m$ is the dielectric constant of the dielectric medium or sensing medium and $\varepsilon_s$ is the dielectric constant of the metal.

At the resonance condition, equation (2.3) will be $k_{ev}=k_g$. Based on the previous discussion the resonance will occur at the following condition (Zhao, Deng, & Li, 2014),

$$\frac{\omega}{c}\sqrt{\varepsilon_g}\sin\theta_{res} = \frac{\omega}{c}\sqrt{\frac{\varepsilon_m\varepsilon_s}{\varepsilon_m + \varepsilon_s}} \tag{2.25}$$

Resonance condition is also clearly understandable in the Figure 2.5. Figure 2.5 shows the incident light wave in dielectric medium ($k_{inc}$), evanescent wave ($k_{sp}$) and the dispersion curve for metal-prism and metal-dielectric. According to the Figure 2.5, it is clearly visible that at the resonance angle $k_{ev}=k_g$ and the propagation constant of evanescent wave ($k_{ev}$) could be coincide with the SPW of metal-dielectric interface. It is noted that, $k_{ev}$ never be coincide with the SPW of metal-prism interface.
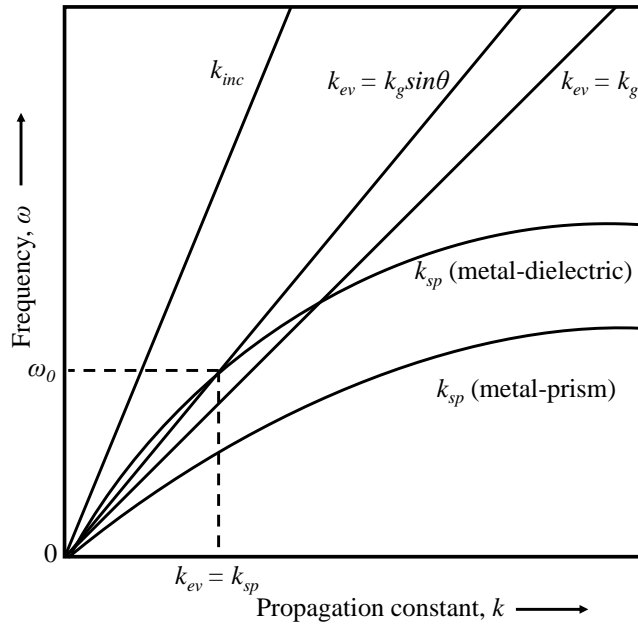


**Figure 2.5:** Incident light wave in dielectric medium ($k_{inc}$), evanescent wave ($k_{sp}$) and the dispersion curve for metal-prism and metal-dielectric (Zhao et al., 2014).

## 2.7 Photonic Crystal Fiber Surface Plasmon Resonance

Photonic crystal fiber (PCF) is a special class of optical fiber. It consists core and cladding as like the conventional optical fiber, but in PCF, the cladding region is consist with periodic air-holes, which can control the light propagation. PCFs also known as holey-fibers (HFs) or microstructured optical fibers (MOFs). Light propagate through the

PCFs follow the modified total internal reflection (M-TIR) or photonic band gap (PBG) effects.

Since last decade, PCF SPR sensor has been shown great attention. PCF SPR sensor is the combination of PCF technology and the plasmonic science. SPR sensors require a metallic component carrying large amounts of free electrons. These free electrons provide the real part of a negative permittivity which is essential for plasmonic materials. By introducing the plasmonic metal layer coating inside the air-holes surface or the outer surface of the PCFs structure SPR effects could be realized.

### 2.7.1 Advantages of Photonic Crystal Fiber Over Prism

Prism based SPR sensors are worked based on angle interrogation method. At a specific angle when the wave vector of EW and SPW are matched then the resonance is occurred and a reflected wave is generated. In practice, light lunching in a specific angle is difficult. Moreover, its structure also bulky. To solve those problems PCFs have shown great attention since last few decades. By harnessing the advantages of PCFs such as small-size and design flexibility, it is possible to control the evanescent field. Based on the applications, core-guided leaky-mode propagation can be controlled by using different types of PCF's structures such as hexagonal, square, octagonal, decagonal, hybrid, etc.; and also their guiding properties can be controlled by optimizing the structural parameters (Ahmmed, Ahmed, & Razzak, 2013; Aoni, Ahmed, & Razzak, 2013). Optimizing core-clad diameter or position, light propagation in single mode as well as launching light at zero incidence angle into the core to excite SPs are possible. Single mode PCFs show very sharp resonance peak, which enhance the detection accuracy (Slavík, Homola, & Čtyroký, 1999). Besides, sensitivity and sensing range could be increased by optimizing the structural parameters.

### 2.7.2    Sensing Mechanism of PCF SPR Sensor

PCF based SPR sensors are working based on evanescent field. When the light propagates through the core by following the total internal reflection then a part of the electromagnetic filed that propagates from the cladding is called the evanescent field. In PCF SPR sensor structure, evanescent field penetrate through the cladding region and hit on the plasmonic metal surface which excite the free electrons of the metal surface. When the frequency of the incident photon and the frequency of the free electrons are matched, the electrons start to resonate and at this condition surface plasmon wave is generated on the metal-dielectric interface, this is called the resonance condition. At this resonance condition, a sharp loss peak is appear which is very sensitive with the adjacent dielectric layer of metal layer. Mathematically, resonance will occur when the real effective refractive index ($n_{eff}$) of core-guided mode and surface plasmon polaritons (SPP) mode value are exactly the same. At the resonance condition, maximum energy transfer from the core-guided mode to the SPP mode. Due to the change of refractive index of dielectric media (sample media), $n_{eff}$ of SPP will change resulting the loss peak and the resonant wavelength shift. This indicates the phase matching wavelength changes with the change of sample/analyte refractive index. Unknown sample could be detected by observing the variation of loss peak due to change of analyte RI.

### 2.8    Implementation of PCF SPR Sensor

PCF SPR sensor is the combination of PCF technology and the plasmonic science. In practice, PCF can be fabricated by following the standard Stack-and-Draw fiber drawing method (G Amouzad Mahdiraji et al., 2014) and plasmonic metal layer coating can be carried out by following the high pressure chemical vapor deposition (CVD) method (Sazio et al., 2006) or sputtering method (Malinský, Slepička, Hnatowicz, & Švorčík, 2012). Numerical implementation of PCF SPR sensor structure is described below.

### 2.8.1 PCF Structure Implementation

### 2.8.1.1 Geometrical Definition

First step is to design the PCFs according to the design rules such as for the hexagonal PCFs structure, the vertex angle of triangle (triangle has two legs in equal distance) would be $60^0$ while for the octagonal and decagonal PCFs this angles would be $45^0$ and $30^0$ shown in Figure 2.6. In the PCFs, air-holes are arranged in a periodic form with the diameter of d. Two adjacent air-holes distance is known as pitch and defined as $\Lambda$.
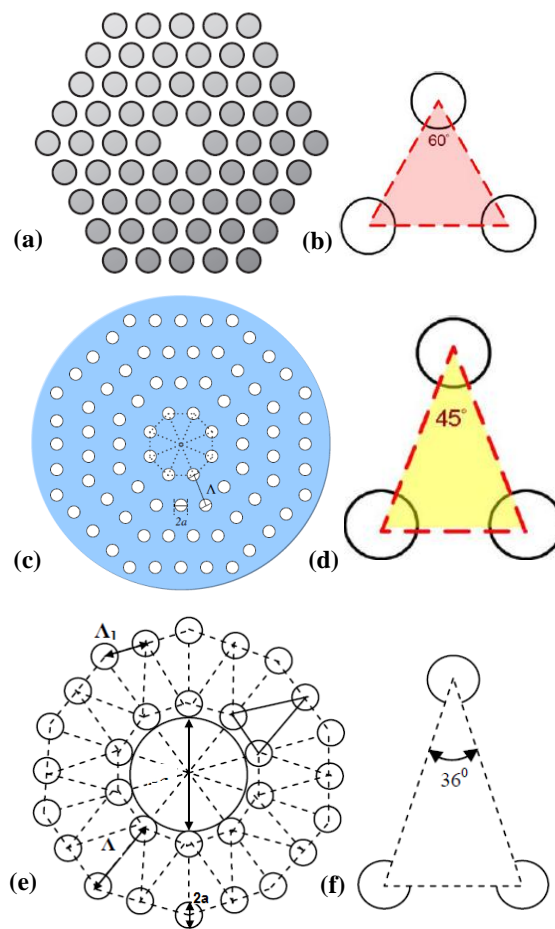


**Figure 2.6:** (a) and (b) Cross-section view and unit triangle of hexagonal PCF respectively; (c) and (d) cross-section view and unit triangle of octagonal PCF respectively; (e) and (f) cross-section view and unit triangle of decagonal PCF, respectively.

For the realization of PCF SPR sensor phenomenon, plasmonic metal layer and a sensing layer have to be considered. Metal layer thickness can be defined by t and the sensing

layer thickness $t_{na}$. In this stage, a Perfectly Matched Layer (PML) boundary region need to be considered.

## 2.8.1.2  Material Define

After designing the PCF, next step is to define the materials. For a standard PCF (considering solid core PCF), the cladding region such as air-holes refractive index is defined as 1. Generally, fused Silica (SiO$_2$) is used for the background material as well as the core material. Refractive index profile of silica is wavelength dependent resulting the use of Sellmeier equation that is defined (Akowuah et al., 2012);

$$n^2(\lambda) = 1 + \frac{B_1\lambda^2}{\lambda^2 - C_1} - \frac{B_2\lambda^2}{\lambda^2 - C_2} - \frac{B_3\lambda^2}{\lambda^2 - C_3} \qquad (2.26)$$

where refractive index of the silica is n and wavelength, $\lambda$ is in μm. Moreover, Sellmeier coefficient, $B_1 = 0.69616300$, $B_2 = 0.407942600$, $B_3 = 0.897479400$, $C_1 = 4.67914826 \times 10^{-3}$ μm$^2$, $C_2 = 1.35120631 \times 10^{-2}$ μm$^2$ and $C_3 = 97.9340025$ μm$^2$.

Besides, as described in previous section, for the PCF SPR sensor, metallic layer is necessary. Complex optical properties of the materials are defined by following the well-known Drude-Lorentz model or interpolating the experimental data of plasmonic materials (DeVore, 1951; Vial, Grimault, Macías, Barchiesi, & de La Chapelle, 2005).

## 2.8.1.3  Boundary Setting

Boundary setting is an essential issue for the numerical simulation. For the realization of SPR sensor in PCF, propagation loss is an important factor. Propagation loss is calculated by using the imaginary part of effective refractive index, Im[$n_{eff}$] value. During the propagation some of light are scattered towards the surface and reflected back which interrupt the results. As a result to absorb the radiated light towards the outer surface as well as diminish the reflection from the surface PML boundary condition is widely used (Dular et al., 2008; Viale, Février, Gérôme, & Vilard, 2005). By taking the symmetrical

structural benefits full structure can be divided by quarterly, and only one quarter able to provide the accurate result which reduce the computational time. In such partial structure artificial boundary condition such as electric field along the x-axis and magnetic field along the y-axis can be used to determine the fundamental mode.

### 2.8.1.4 Meshing

Computational area can be divided into finite number of small triangular or rectangular region which is known as mesh. Meshing is an important parameter to precisely investigate the mode profile. In computational region where the light propagates, precisely analyzing the propagation can be performed by increasing the mesh density of the area. Number of mesh size indicates, how many mesh elements are used. Higher number of mesh elements are better for the numerical simulation which indicates the computational region is divided into the small region which increases the probability of result accuracy.

### 2.8.1.5 Solving

As mentioned in previous section, commercial COMSOL multiphysics software is used in this study. After going through all described process the final stage is to compute the simulation. For the PCF SPR sensor need to find the core-guided mode and SPP mode. Before the computation take place, the operational wavelength and the number of searching modes need to be specified. Number of searching mode allow to show the core-guided fundamental mode and all the possible higher order modes. The modes over the operational wavelength range of interest can also be calculated from the latest version of COMSOL software. For calculating the confinement loss, the required data, i.e., imaginary effective index value can be extracted from COMSOL.

### 2.8.2    Combination of PCF with Plasmonic Science

By incorporating the thin metallic layer with the PCF structure, surface plasmon can be established. Thin plasmonic metal layer is used inside the air-holes surface or the outer surface of the fiber structure. Evanescent field of the core-guided mode excite the free electrons of metal layer; while the frequency of the incident photon and the free electrons frequency will matched then the surface plasmon resonance will occur. For the PCF SPR sensor, to apply this resonance mechanism in sensing, a dielectric layer (sensing medium) is considered sequentially top of the metal layer. Optical property of dielectric layer such as refractive index (RI) is used. RI value of dielectric medium is sensitive to the $n_{eff}$ of SPP mode. Due to change of dielectric RI value, $n_{eff}$ of SPP mode is change resulting the resonance wavelength shift occurs. By observing this resonance shift unknown analyte will be detected. This is the basic working principle of PCF SPR sensor.

### 2.8.3    Accuracy

To get the accurate result mesh size and PML convergence test have to be considered (Poletti, 2007). For a simple PCFs structure by considering the default extremely fine meshing elements are adequate to precisely investigate the mode profile. Nonetheless, for the complex structure mesh convergence is necessary. Besides, PML convergence is an important issue as it is use to absorb the radiation. For the PCF SPR sensors confinement loss is the main factor to be determined. To measure the confinement loss, imaginary part of the effective index ($\text{Im}(n_{eff})$) value is necessary. Initially, due to increase of PML thickness, $\text{Im}(n_{eff})$ value is change which may give the false result of confinement loss; but, after a certain PML thickness with the increase of PML thickness. It gives the constant $\text{Im}(n_{eff})$ value. As a result to calculate the accurate confinement loss of a structure, PML thickness verification is necessary. Here, a proposed sensor is considered which is described in details in Chapter 3. Cross-section of the proposed sensor is shown in Figure 2.7(a) and the meshed structure is shown in Figure 2.7(b). For the verification

of PML thickness, the optimum thickness is determined by varying the PML thickness from 0 - 20 μm. According to the Figure 2.7(c), initially with the increase of PML thickness, imaginary $n_{eff}$ values are rapidly changed, however a small variation in $n_{eff}$ value is observed by changing the PML thickness from 4 μm to 20 μm. As we know to measure the loss of a PCF, $Im(n_{eff})$ value is the main parameter. In this range of PML thickness (i.e., 4-20 μm), a very small $Im(n_{eff})$ variation of about $\pm 2$ dB/cm is observed. Thus, a PML thickness of 5 μm seems to be optimized for this structure for the better radiation absorption. However, if a thicker PML region is considered compare to the structure size then the core-guided light propagation is reduced. So, considering all the issues PML convergence is needed for the accurate confinement loss measurement.

It should be noted that since the optimum PML layer thickness might be different in different structures, a pre-optimization is performed per proposed designed in this study.
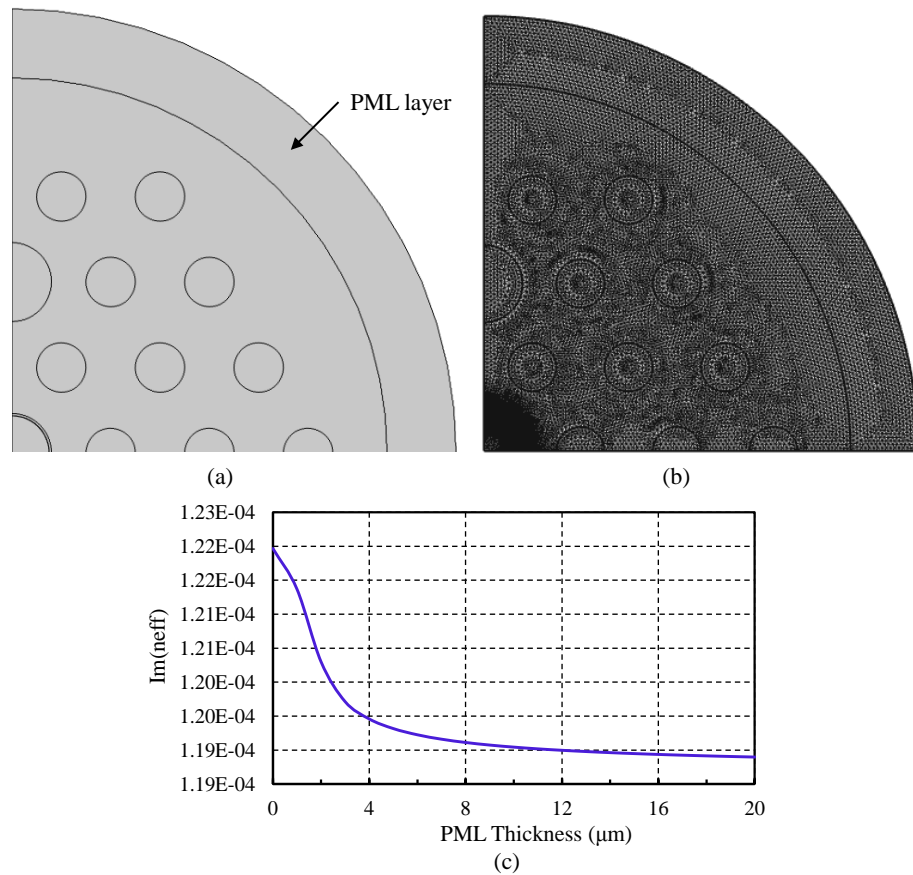


**Figure 2.7:** (a) Cross-section of the proposed PCF SPR sensor structure, (b) Meshing, & (c) Imaginary effective index versus PML thickness for the core-guided fundamental mode of the proposed PCF SPR sensor.

## 2.9 Overview of PCF SPR Sensors

In the last few decades, SPR phenomenon attracted much attention due to its broad range of sensing applications and high sensitivity. SPR sensor has shown remarkable development in biosensing applications such as biomolecular analytes detection, medical diagnostics, antibody-antigen interaction, etc. (Gupta & Verma, 2009; Jiří Homola, 2003; Jiří Homola, Yee, & Gauglitz, 1999; Wong, Krupin, Sekaran, Mahamd Adikan, & Berini, 2014). Generally, a prism coupling configuration with a thin layer of metal coating is used as SPR sensor. Transverse magnetic or p-polarized light that is launched into the prism will be coupled to the metal-dielectric interface when the phase matching condition is met (Zhao et al., 2014). SPR technique for bio-sensing and gas detection was first reported by Liedberg et al. (1983). However, prism based SPR sensor in the well-known Kretschmann set-up is bulky and not suitable for remote sensing (Dash & Jha, 2014b).

PCF based SPR sensing technique is considered a possible route to miniaturization. PCF has been proven as a good replacement of prism, having smaller footprint, easier system integration and cost effective. In 2006, MOF based SPR sensor was introduced for the first time (A Hassani & Skorobogatiy, 2006). Two ring, hexagonal PCF structure was proposed where gold layers and liquid were infiltrated selectively in the $2^{nd}$ ring, shown in Figure 2.8(a). A small central air-hole was used to establish the phase matching phenomena. Due to different guided modes three resonance peaks were appeared and the $1^{st}$ resonance peak shown the highest resonance depth with the sensor resolution of $3 \times 10^{-5}$ RIU. To prevent the selective gold coating and liquid infiltration, honeycomb MOF had been reported with the external sensing scheme, shown in Figure 2.8(b) (Gauvreau, Hassani, Fassi Fehri, Kabashin, & Skorobogatiy, 2007). In this work, gold and sensing layer has been placed outside the fiber structure to make the sensing process simple and straight forward in practice. Using the PCF SPR phenomena detection of biolayer thickness has been reported (Figure 2.8(c)) which is applicable for monitoring the

concentration of nanoparticles for the study of photodynamic cancer therapy (Alireza Hassani & Skorobogatiy, 2009).
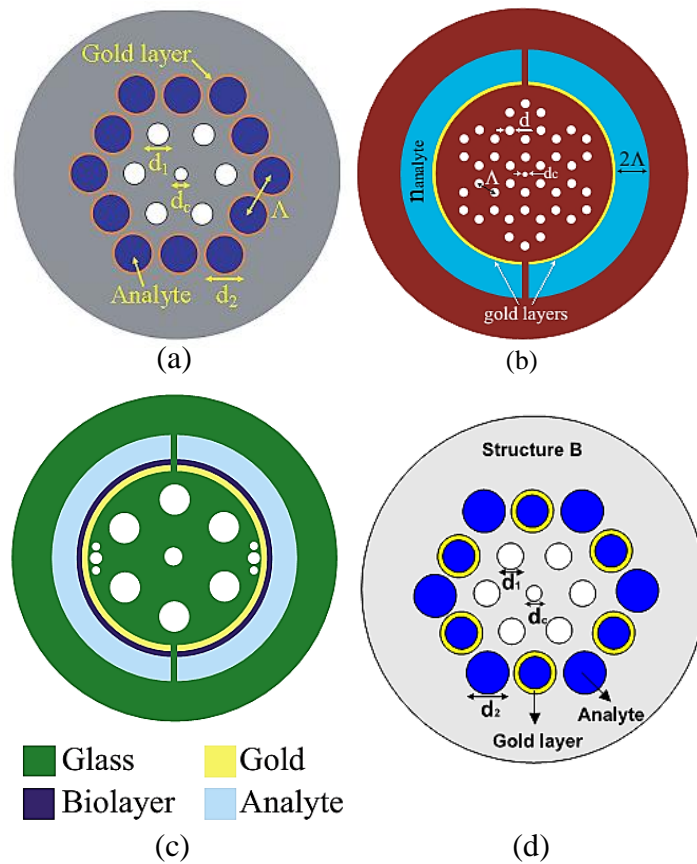


**Figure 2.8:** (a) & (d) Selectively gold coated and liquid-analyte filled PCF SPR sensors (A Hassani & Skorobogatiy, 2006; Yu et al., 2010); (b) & (c) PCF SPR sensor with external sensing approach (Gauvreau et al., 2007; Alireza Hassani & Skorobogatiy, 2009).

To enhance the phase matching between the core-mode and plasmonic mode and also to enhance the detection accuracy selectively gold coated and liquid-analyte filled PCF SPR sensor has been reported (Figure 2.8(d)) (Yu et al., 2010).

In 2011, silver nanowire based PCF SPR has been reported which overcome the metal coating problem (Figure 2.9(a)) (Fu, Lu, Huang, & Yao, 2011). To show the positive and negative refractive index sensor, liquid-core PCF has been reported (Shuai, Xia, & Liu, 2012). Six selective liquid-analyte filled core has been considered with one metallic channel to exhibit the positive and negative RI sensitivity simultaneously (Figure 2.9(b)). The maximum positive RI sensitivity of 3,600 nm/RIU in the sensing range of 1.45-1.46
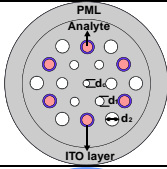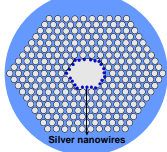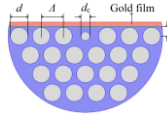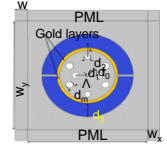
and the negative RI sensitivity of -5,500 nm/RIU has been achieved in the sensing range of 1.50 to 1.53, which is potential for high refractive index analyte detection like chemical sensing applications. Very recently, for multi-analyte detection, PCF based SPR sensor has been reported where the gold layer and sensing layer are split into four sections for utilizing the multi analyte detection (Figure 2.9(c)) (Otupiri et al., 2015). To overcome the metal coating problems inside the micron-diameter holes in PCF, several PCF SPR biosensors has been reported where the metallic layer and sensing layer are located outside the PCF structure for the ease of sensing (Akowuah et al., 2012; Dash & Jha, 2014a; Otupiri et al., 2014). D-shaped PCF SPR sensors is one example of such structure that have been proposed (Figure 2.9(d)) (Dash & Jha, 2015a; Tan et al., 2014; Tian et al., 2012), where one side of PCF is polished and the metal layer applied on the flat top.



(a)

(b)

(c)

(d)
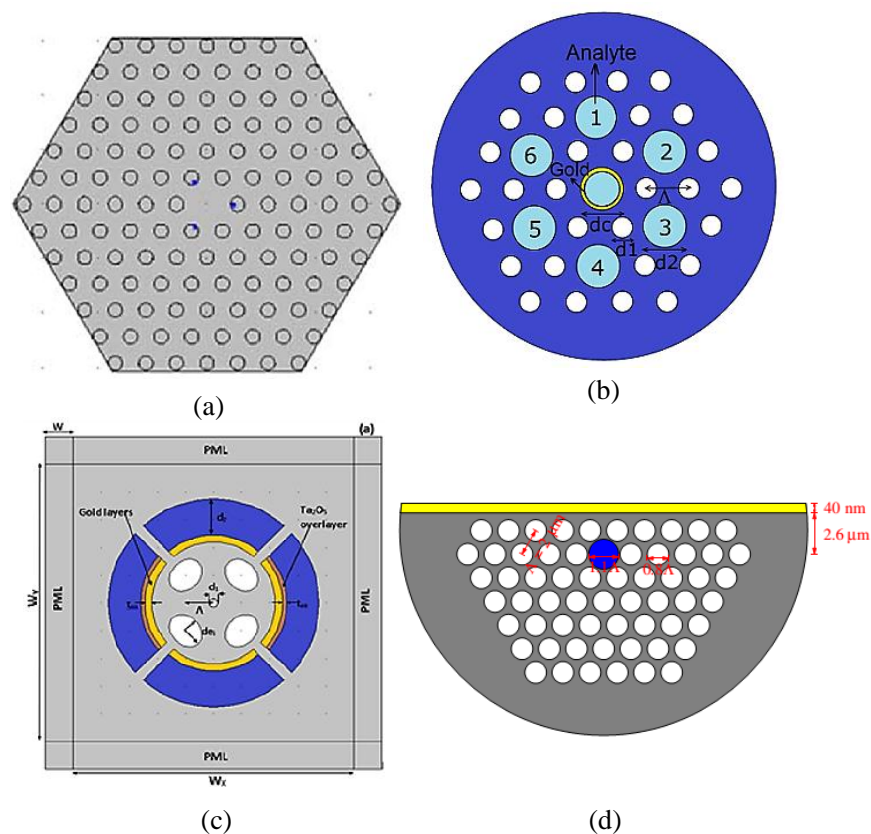
**Figure 2.9:** (a) Silver nano-wire based PCF SPR sensor (Fu et al., 2011), (b) Selectively liquid-analyte infiltration for the coexistence of positive and negative RI detection (Shuai, Xia, & Liu, 2012), (c) Splitting sensor structure for multi-analytes detection (Otupiri et al., 2015) and (d) D-shaped PCF SPR sensor (Tan et al., 2014).

This significantly improved the uniformly coating issues, however, this requires accurate polishing effort to precisely remove a predetermined portion of the PCF, which is practically difficult. Overall, complexity in the PCF structure is one of the common difficulty observed in most of the SPR sensors reported in the literature. Fabrication of such irregular PCF structures that requires different sizes of holes to be placed in specific positions in the fiber geometry would be practically challenging even with very accurate fiber preform drilling systems. Thus, a simpler and scalable structure can lead to feasible solution for ubiquitous remote SPR sensing. However, to sum up, reported PCF SPR sensors can be classified in four different types such as internal metal coating, internal nanowires filling, D-shaped and micro-fluidic slots based PCF SPR sensors. Table 2.2 shows the advantages and disadvantages of the reported PCF SPR sensors.

**Table 2.2:** Advantages and disadvantages of different type of PCF SPR sensors.

| Classification of PCF SPR sensors | Advantages | Disadvantages | Structural diagram | Ref. |
|---|---|---|---|---|
| Selectively metal coating | air-holes act as a cell and sample can flow through the air-holes | selectively metal coating is challenging as the air-holes size in micron size |  | (Dash & Jha, 2014b) |
| Internal nanowires filling | a small nanowire portion is required and sample can flow through the air-holes | selectively nanowires with liquid filling is required |  | (Lu, Yang, Wang, & Yao, 2015) |
| D-shaped | sample can flow through the outer surface which make the sensor structure simpler | accurate polishing effort is required |  | (Luan, Wang, Lv, & Yao, 2015) |
| Micro fluidic slots | able to detect multiple analyte at the time instant | create the microfluidic slot is challenging |  | (Otupiri et al., 2014) |

## 2.10    Verification of Simulation Method

Up to date, only theoretical studies on PCF SPR sensor were reported and fabrications are yet to be demonstrated, as a result, proposed numerical method was applied to

reproduce the results reported in (Shuai, Xia, & Liu, 2012), which has been published in well-known top ranked journal. Figure 2.10(a) shows the cross-section of reported PCF SPR sensor where multi liquid-analyte channels have been used with the single gold metallic channel.
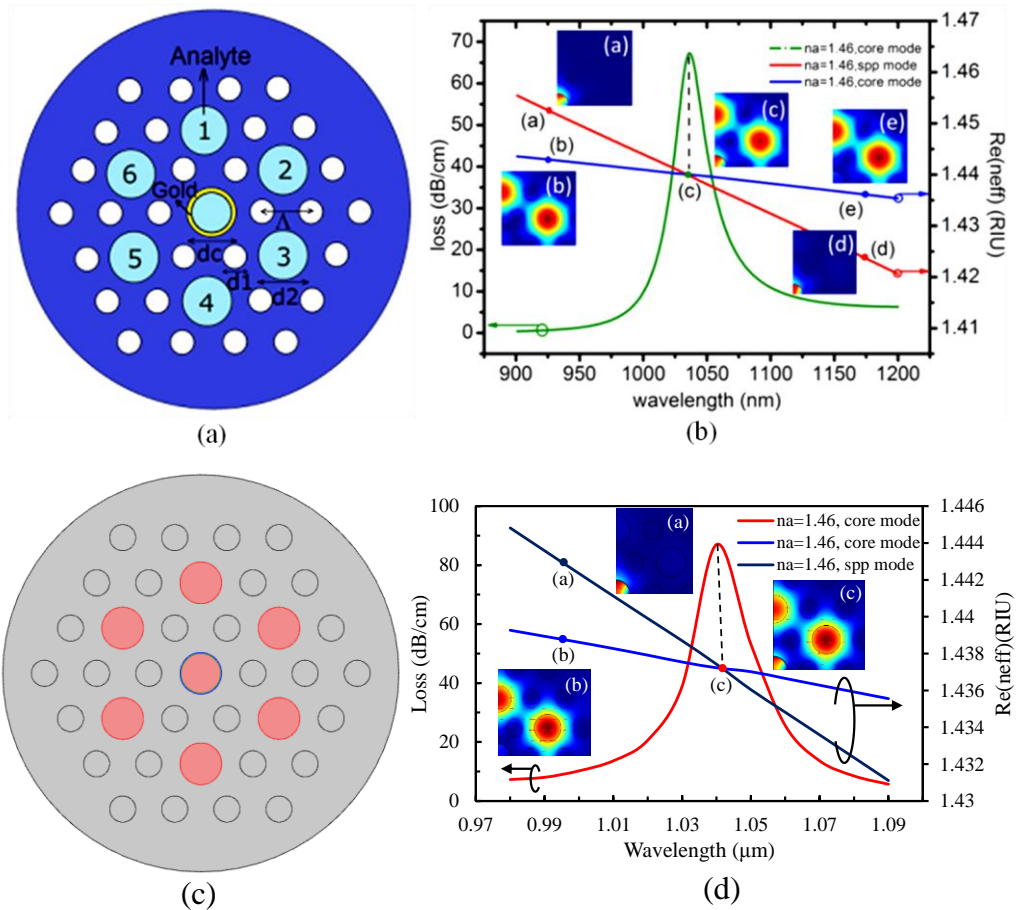


**Figure 2.10:** (a) & (b) Cross-section of the published PCF SPR sensor and the phase matching phenomena, respectively (Shuai, Xia, & Liu, 2012); (c) & (d) reproduced cross-section view and phase matching phenomena, respectively.

Figure 2.10(b) shows the phase matching phenomena between the $n_{eff}$ of core-guided mode, SPP mode and loss peak which are the main criteria of PCF SPR sensor. As shown in Figure 2.10(b), $n_{eff}$ of core-guided mode, SPP mode and loss peak are matched at the wavelength of 1040 nm while analyte $n_a$ is 1.46. As described before, unknown analyte will be detected by measuring the resonance wavelength shift due to analyte RI changes. At the resonance wavelength loss value is achieved 68 dB/cm.

Figure 2.10(c) & (d) shows the reproduced cross-section outlook of PCF SPR sensor and the phase matching phenomena respectively. According to Figure 2.10(d), phase matching wavelength is appear at 1.04 μm while the analyte $n_a$ is 1.46; this is exactly same as the reported result. According to the reproduced structure, peak loss value shows 88 dB/cm which is a little bit larger than the reported works. The peak loss value difference is occurred due to the fiber diameter and PML thickness are unknown and here convergence test has been used to reproduce the result. In Figure 2.10 (b) & (d), inset(c) shows the energy transfer from the core-guided mode to the SPP mode which is almost same, furthermore, core-guided mode and SPP mode propagation also alike both of the works. Based on the discussion and the reproduced results, the computational method which is following for this research work is correct.

## 2.11    Optical Properties and Metallic Films

As described in previous sections, metal is the important element for the plasmonic behavior. SPR sensors require a metallic component carrying large amounts of free electrons, these free electrons provide the real part of a negative permittivity which is essential for plasmonic materials. Generally, novel material gold (Au), silver (Ag), copper (Cu) and aluminum (Al) are widely used as the plasmonic material. Generally metals are prone to oxidize due to presence of aqueous environment, water, humidity, and etc. For the SPR sensing applications Au and Ag are comprehensively used. Gold is chemically stable in aqueous environment. Also, it shows a larger resonance peak. However, it shows the broaden resonance peak which may give the false positive analyte detection result as a result detection accuracy is diminish (Dash & Jha, 2014a). Besides, Ag shows a sharper resonance peak. It is utmost conductive and its material losses are less among the available materials. However, it has oxidation problem, owing presence of aqueous environment it oxidizes easily which reduces the sensing performance (Naik, Shalaev, & Boltasseva, 2013). Copper is the 2$^{nd}$ most conductive material after the silver. It is much

cheaper compared to both gold and silver. Cu material damping rate is the same as Au, and its interband transition is also close to Au (West et al., 2010). Cu also has oxidation problem which is the main reason hence it is not received great attention compared to Au and Ag. The oxidation problem can be solved by using a thin bimetallic layer coating top of the Ag or Cu surface (Zynio, Samoylov, Surovtseva, Mirsky, & Shirshov, 2002). In contrary, as the plasmonic material Al didn't receive that much of attention as its damping rate is very high as well as its material losses also high. As a result, it did not attain attention for the sensing applications (West et al., 2010).

## 2.12    Summary

In this chapter, basic properties of surface plasmon and Maxwell's master equation is derived to investigate the light traveling properties. Conventional SPR sensors working mechanism and problems are discussed. In addition, advantages of PCF over prism in SPR sensing are labelled. A brief literature review on PCF based SPR sensors are given in this chapter. Importance and the status of the plasmonic materials are outlined. Numerical methods are described and compared based on the mode propagation property of PCFs.  PCF SPR sensor implementation is carried out in details to understand the design procedure. Furthermore, design convergence is described which helps to get the accurate results and validate the proposed method by reproducing the reported literature results. To sum up, conventional prism based SPR sensor problems can be solved by using PCF. However, yet, reported PCF based SPR sensors structure are challenging in terms of fabrication point of view which limits the practical implementation.

# CHAPTER 3: GRAPHENE-SILVER DEPOSITED PLASMONIC SENSOR

## 3.1 Introduction

In this chapter a fiber Surface Plasmon Resonance sensor based on PCF with selectively filled analyte channels is proposed. Silver is used as the plasmonic material to accurately detect the analytes and is coated with a thin graphene layer to prevent oxidation. The liquid-filled cores are placed near to the metallic channel for easy excitation of free electrons to produce SPWs. Surface plasmons along the metal surface are excited with a leaky Gaussian-like core guided mode. Numerical investigation of the fiber's properties and the sensing performance is performed with FEM. The effects of fiber structural parameters on the properties of plasmonic excitation are investigated and optimized for the sensing performance as well as reducing the sensor's footprint.

## 3.2 Literature Review

In the last few decades, photonic biosensors had shown remarkable developments in various applications such as medical diagnostics, bio-chemical detection and organic chemical detection (Akowuah et al., 2012; Jiří Homola, 2003; Kim et al., 2013; Ortega-Mendoza et al., 2014). To date, several sensing techniques are available such as micro-ring resonator sensor (Yuan et al., 2014), surface plasmon resonance (SPR) sensor (Akowuah et al., 2012; Jiří Homola, 2003), evanescent wave absorption spectroscopy, etc. Surface plasmons (SPs) are the collective oscillations of free electrons that propagate along a metal-dielectric interface by satisfying certain resonance conditions (Daghestani & Day, 2010; Jiří Homola, 2003). The first SPR experiment for bio-sensing and gas detection was reported by Jorgenson and Yee (1993), since then, SPR has been given much attention due to its extremely sensitive performance. In the conventional

Kretschmann SPR configuration, a coupling prism with a thin metal-deposited base is used, in the presence of incident light at a specific angle; SPs will be excited on the metal-dielectric interface. However, the conventional SPR configuration is bulky and not suitable for remote sensing, which limits its large scale fabrication for real time application (Dash & Jha, 2014b).

To overcome these limitations, the feasibility of fiber-based SPR sensor in sensing application is explored. Besides, increasing the sensitivity and enhancing the sensing range are possible by optimizing the PCF structural parameters. Phase matching between the core-guided mode and the surface plasmon polaritons (SPPs) mode could be achieved by carefully designing the fiber structure. In general, a sharp loss peak appears at phase matching wavelength enables the sample analyte to be detected (Gupta & Verma, 2009). The sensing performance depends highly on the choice of plasmonic materials, in most cases, gold and silver are used. Gold is chemically stable and shows larger resonance peak shift as compared with the other active plasmonic materials. However, due to the large absorption coefficient, resonance band of gold is broader, which reduces the sensing accuracy. The other problems associated with gold including the formation of island in thin gold layer, band to band transition and surface roughness due to thermal evaporation (Dash & Jha, 2014b; Kanso, Cuenot, & Louarn, 2007). On the contrary, silver shows sharper resonance peak as compared with the other plasmonic materials. Nonetheless, silver is not chemically stable and could be oxidized easily (Lu et al., 2013). Silver film with graphene coating has shown to solve the problem of oxidation since graphene is impermeable to gas molecules as small as Helium and therefore inhibits the passing of oxygen (Choi, Kim, & Byun, 2011). Furthermore, graphene coating applied on the metal surface can improve the sensing performance due to its high surface to volume ratio. Besides, it increases the absorption of analyte molecules owing to the π-π stacking and possesses superior plasmonic properties that are suitable for sensing (Dash & Jha, 2014a;

Maharana & Jha, 2012; Salihoglu, Balci, & Kocabas, 2012). Fiber-based plasmonic phenomenon realized by replacing the metal film with graphene was first reported by Kim et al. (2013), where a thin graphene layer was created by using thermal chemical vapor deposition (TCVD) technique. Sensing performance improvement of SPR sensors with graphene coating on top of Au/Ag compared with the SPR sensors without graphene coating are also reported (Dash & Jha, 2014a; L. Wu, Chu, Koh, & Li, 2010). Recently, gold is used as an active plasmonic material and selectively infiltrating the core of PCF with high refractive index (RI) analyte to introduce the coexistence of positive and negative RI (Shuai, Xia, & Liu, 2012). On the other hand, different fiber structures with enhanced evanescent field in the fiber based SPR sensor were reported. They are elliptical air-hole PCF sensor with four separated microfluidic slots (Akowuah et al., 2012); multi-hole fiber SPR sensor where all the holes are coated with gold and titanium dioxide (Gao et al., 2014); selectively six metal oxide coating and liquid infiltration inside the six-air-hole with four different sizes of capillary holes in a polymer PCF (Dash & Jha, 2014b); and a seven-air-hole liquid infiltration with six metal oxide coating (Qin et al., 2014). However, the abovementioned fiber-based SPR sensors are difficult to be fabricated due to both complex fiber structure and the existence of several metallic channels.

In this chapter, a simple liquid core PCF plasmonic sensor with selectively filled analyte channels is proposed. Silver layer with graphene coating is used to improve the sensing performance. Proposed sensor shows higher amplitude sensitivity as compared with reported works in (Gao et al., 2014; Alireza Hassani, Gauvreau, Fehri, Kabashin, & Skorobogatiy, 2008) and higher wavelength interrogation sensitivity than sensors reported in (Biswas, Chattopadhyay, & Bhadra, 2014; Dash & Jha, 2014b; Lu et al., 2012). The metallic channel, liquid cores, and unique air holes arrangement of the proposed sensor introduce larger evanescent field that results in stronger coupling between the core-guided mode and the SPP mode.

### 3.3 Methodology

### 3.3.1 Structural Design and Numerical Analysis
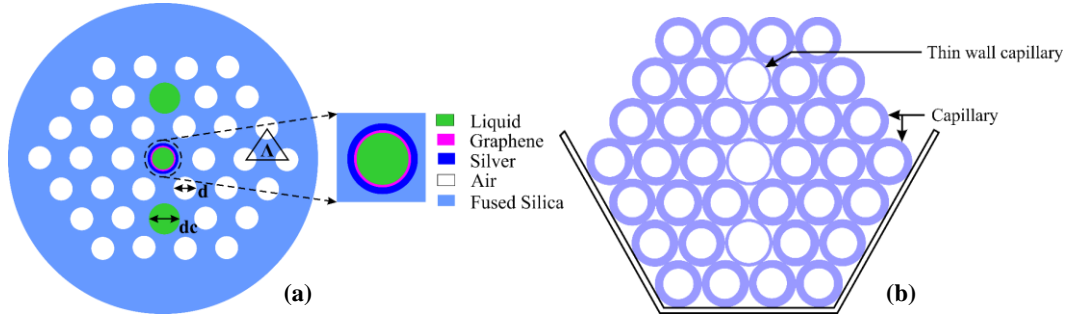


**Figure 3.1:** Cross-section of the proposed (a) sensor, (b) stacked preform.

Figure 3.1(a) shows the cross-section of the proposed fiber sensor. Two identical cores are filled with high RI liquid (analyte) and form a straight line with the center metallic channel. The proposed structure couples core-guided mode and plasmonic mode at the interface of silver-graphene layer and the analyte. The air-holes are distributed in triangular lattice where the distance between adjacent air-holes (lattice constant, pitch) is $\Lambda=1.90$ μm and the air-hole diameter is $d=0.5\Lambda$. The analyte core diameter and the metallic channel diameter are similar, $d_l=d_c=0.8\Lambda$. Liquid-filled hole diameter is larger than the other air-holes to simplify the flow of the analyte through them. Silica (SiO$_2$) RI profile is approximated by the Sellmeier equation (Otupiri et al., 2014). A graphene layer on top of a thin silver layer is used at the inner wall of the fiber central core. The silver and graphene thicknesses are set as $t_{ag}=35$ nm and $t_g=3$ nm, respectively. The RI of silver is adopted from (Palik, 1998) and the complex RI of the graphene is determined from the equation: $n_g=3+iC_l\lambda/3$, where $\lambda$ is the vacuum wavelength in μm and constant $C_l\approx5.446$ μm$^{-1}$. To analyze the guiding properties of the proposed sensor, FEM is used by considering PML boundary condition as a radiation absorber. By taking the advantage of the symmetrical structure, we compute only a quarter of the proposed structure to reduce the computation time. Perfect electric conductor (PEC) and perfect magnetic conductor

(PMC) boundary conditions are used at the horizontal and vertical outer boundaries respectively.

### 3.3.2    Realization of the Proposed Sensor

Fabrication of the proposed fiber structure is possible using the standard stack-and-draw method (G Amouzad Mahdiraji et al., 2014). The two larger cores and the central metallic channel can be realized by introducing thinner wall capillaries compared to the other capillaries during the stacking process, as illustrated in Figure 3.1(b). The deposition of metal layers on the inner surface of the air-holes in the proposed structure is possible by applying the high pressure CVD technique, thermal evaporation, sputtering technique, electroless plating technique or wet-chemistry technique (Sazio et al., 2006; Takeyasu, Tanaka, & Kawata, 2005). Deposition of graphene layer in the capillary would also be possible by using the CVD method. Ismach et al. had realized graphene layer on dielectric surface using CVD method (2010). Deposition of graphene on microfiber had also been reported by Y. Wu et al. (2014). Besides, growing graphene on silver had been demonstrated by Kiraly et al. (2013). The liquid selective infiltration of single-hole (Guo et al., 2014) and multi-holes (Vieweg et al., 2010) in PCF are also reported by using two-photon direct laser writing and direct manual gluing method.  The proposed sensor can be calibrated with a liquid with known RI and using the flow cell analyte containing process. Since a very short length of optical fiber is required for SPR sensors, the incretion and exchange of analyte inside the fiber holes are practically feasible. As proposed by C. Wu et al. (2013), this can be realized by using two short pieces of C-shape fibers placed on the two sides of the PCF SPR sensor. Based on these developed methods, the proposed sensor in this chapter is potential to be fabricated.

## 3.4    Results and Discussions

### 3.4.1    Performance Analysis with Respect to Analyte RI

The triangular lattice arrangement and the two identical cores perpendicular to the metal-coated channel ensure the polarization-independent propagation characteristic. The fundamental core-guided mode, SPP mode and the resonant spectrum for an analyte with RI, $n_a$=1.46, are shown in Figure 3.2.
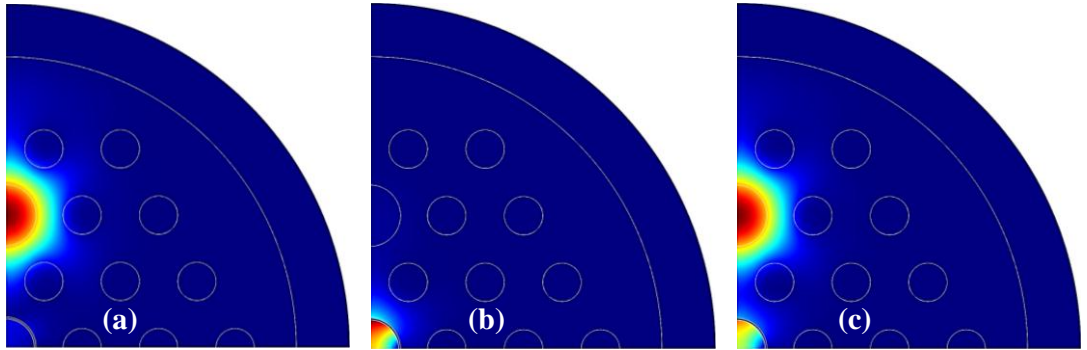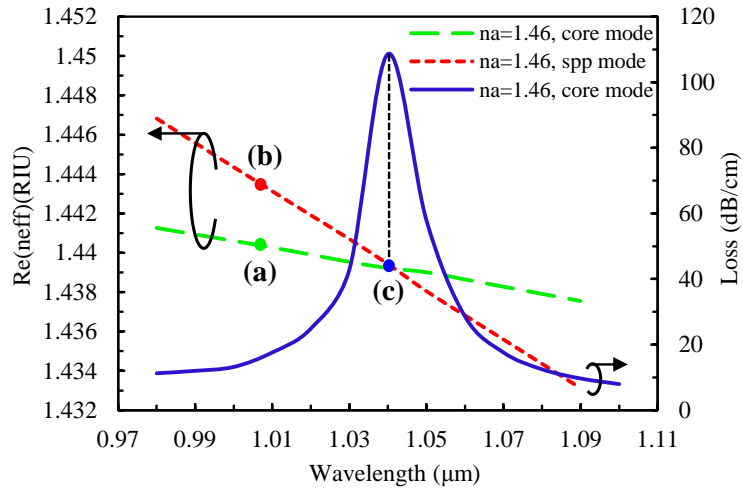


**Figure 3.2:** Dispersion relation of the core-guided mode (green), plasmonic mode (red) and the loss spectrum (blue); inset (a) and (c) show the electric field of the core-guided mode and inset (b) shows the electric field of the plasmonic mode.

The real part of effective refractive index ($n_{eff}$) of the core-guided mode and the SPP mode are represented by the green and red dash lines respectively. By using the imaginary part of $n_{eff}$, the propagation loss is determined by the following equation (Akowuah et al., 2012); $\alpha = 40\pi.Im(n_{eff})/(ln(10)\lambda) \approx 8.686 \times k_0.Im[n_{eff}]$ dB/m, where $k_0=2\pi/\lambda$ is the wave number in free space and $\lambda$ is the wavelength in μm. A sharp loss peak is found at the

resonant wavelength, 1040 nm, where the core-guided fundamental mode and the SPP mode intersect. This indicates the maximum power is transferred from the core-guided fundamental mode to the SPP mode. In Figure 3.2, for the core-guided fundamental mode (inset (a)), light is well confined in the liquid core, whereas for the SPP mode outside the resonant wavelength (inset (b)), light exists at the metal surface. As for phase matching (inset (c)), fundamental core-mode and SPP mode are coupled with a loss peak at 1040 nm. The proposed sensor is very sensitive in response to the RI of analyte, a small change in analytes RI leads to large shift in the loss peak. By varying the analyte RI from 1.46 to 1.49, the results of peak wavelength shift are shown in Figure 3.3(a).
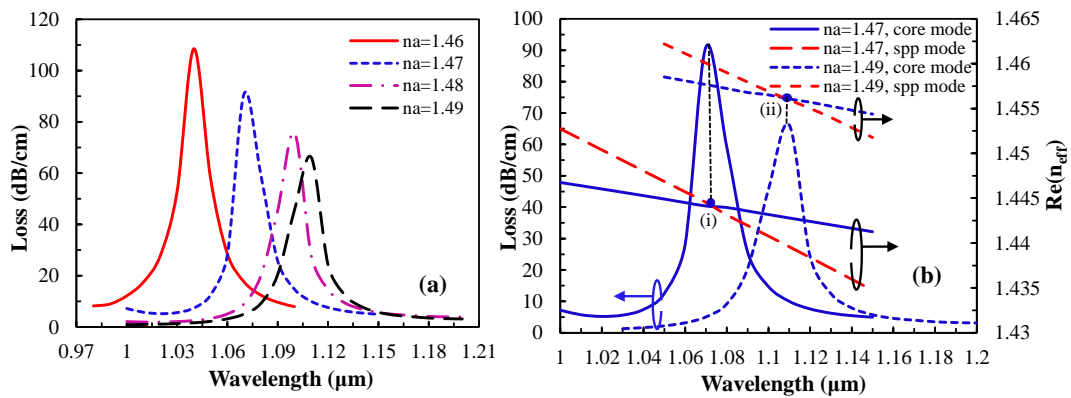


**Figure 3.3:** (a) Loss spectrum of the fundamental mode by increasing analyte RI, $n_a$, from 1.46 to 1.49, (b) dispersion relation of the core-guided mode for $n_a$=1.47 (solid lines) and $n_a$=1.49 (dashed lines). Red and blue lines indicate SPP mode and the fundamental core-guided mode respectively. Point (i) and (ii) are the phase matching points for analyte $n_a$=1.47 and 1.49.

The real part of $n_{eff}$ of plasmonic mode depends strongly on the vicinity layer of analyte RI. Due to the small change of analyte RI, real part of the $n_{eff}$ of SPP mode changes, which causes the change of phase matching wavelength between the core guided mode and the SPP mode. Mathematically, at the phase matching wavelength, $n_{eff}$ of core guided mode and the SPP mode are approximately the same (A Hassani & Skorobogatiy, 2006). In Figure 3.3(a), with the increase of analyte RI, resonance spectrum shifts toward the longer wavelength and the amplitude of loss spectrum decreases gradually, the fundamental

mode field confinement also increases. The range of resonant wavelength shift is from 1040 to 1070 nm for the change of analyte RI from 1.46 to 1.47. As such, the positive RI sensitivity is 3000 nm/RIU, which is comparable to (Dash & Jha, 2014b; Gao et al., 2014), with proposed simpler sensor structure. The sensitivity is determined by following the equation in (Akowuah et al., 2012); Sensitivity, $S_\lambda(\lambda)=\Delta\lambda_{peak}/\Delta n_a$, where $\Delta\lambda_{peak}$ is the resonant peak shift and $\Delta n_a$ is the analyte RI variation. The proposed sensor shows the sensitivity of 3000, 2900 and 1100 nm/RIU for analyte RI variation range of 1.46-1.47, 1.47-1.48 and 1.48-1.49 respectively.

Generally, PCF SPR sensors show high propagation loss, which limits the sensor's length to generate measurable signal (A Hassani & Skorobogatiy, 2006). The propagation loss of the core guided fundamental mode is a function of analyte RI and the wavelength which is define as $\alpha(\lambda, n_a)$. By considering $P_0$ as the input power launched into the fiber, the detected power after propagating through the sensor of length $L$ is $P(L, \lambda, n_a) = P_0exp(-\alpha(\lambda, n_a)L)$. By considering a small change of analyte RI $dn_a$, the relative sensitivity is define as $S(\lambda) = [P(L, \lambda, n_a+dn_a)-P(L, \lambda, n_a)]/P(L, \lambda, n_a)/dn_a$. Sensor's length $L$ could be optimized through the measurement of modal transmission loss. A reasonable choice for a sensor length is $L = 1/\alpha(\lambda, n_a)$, leading to a simple definition of sensitivity for a small change in analyte RI (Akowuah et al., 2012),

$$S_A(\lambda)[RIU^{-1}] = -\frac{1}{\alpha(\lambda,n_a)}\frac{\partial\alpha(\lambda,n_a)}{\partial n_a} \qquad (3.1)$$

In Figure 3.3(b), it is clear that with the increase of analyte RI, phase matching wavelength changes. Therefore, at the phase matching resonant wavelength, an unknown sample (analyte) could be detected (Akowuah et al., 2012). As the analyte RI is 1.47, the resonant wavelength is 1070 nm and the loss is 91 dB/cm whereas for $n_a$=1.49, the resonant wavelength is 1110 nm and the loss is 66 dB/cm. This indicates that with the increase of analyte RI, energy transfer from the core-guided mode to the SPP mode

reduces, at the same time, the resonance spectrum broadens. In addition, by varying the analyte RI, amplitude of loss peak changes as in Figure 3.4 (amplitude sensitivity). Amplitude sensitivity decreases gradually with the increase of analyte RI due to the core-cladding RI contrast. The maximum amplitude sensitivity is 418 RIU$^{-1}$ at 1070 nm wavelength for analyte of $n_a$=1.46 which is comparable to (Gao et al., 2014; Alireza Hassani et al., 2008). With this sensitivity, the resolution is $2.4 \times 10^{-5}$ RIU, assuming that the proposed sensor is able to detect a minimum 1% change of the transmitted light intensity. Amplitude sensitivity of 410 RIU$^{-1}$ and 138 RIU$^{-1}$ are achieved at 1099 nm and 1110 nm for analyte RI of 1.47 and 1.48 respectively. From the wavelength interrogation and amplitude sensitivity, the proposed sensor is possible to detect high RI liquid in the form of chemical, biochemical and organic chemical analytes.
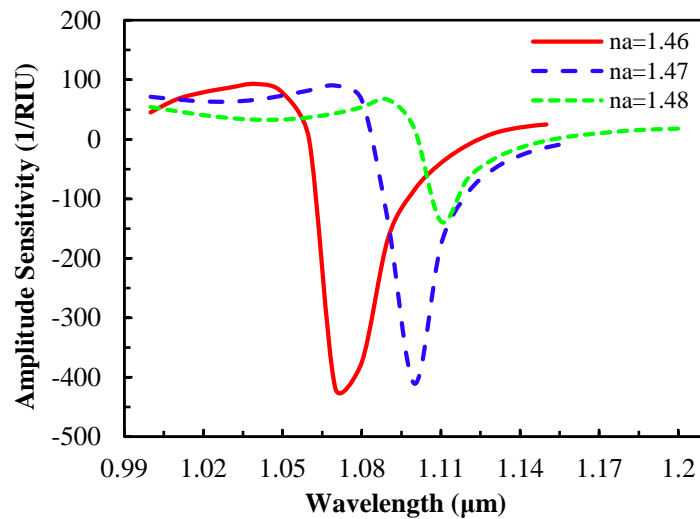


**Figure 3.4:** Amplitude sensitivity as a function of wavelength with the variation of analyte RI.

Table 3.1 shows the performance comparison of the reported PCF SPR sensors.

**Table 3.1:** Performance analyses of simulated PCF SPR sensors.

| Characteristics | RI Range | Interrogation | Sensitivity | Resolution (RIU) | Ref. |
|---|---|---|---|---|---|
| Multi-hole fiber based SPR sensor | 1.33-1.35 | Wavelength | 2,000 nm/RIU | $5\times10^{-5}$ | (Gao et al., 2014) |
| | | Amplitude | 370 RIU$^{-1}$ | $2.7\times10^{-5}$ | |
| Selectively ITO coated polymer PCF | 1.33-1.35 | Wavelength | 2,000 nm/RIU | $5\times10^{-5}$ | (Dash & Jha, 2014b) |
| Selectively filled silver nanowires | 1.330-1.335 | Wavelength | N/A | $4.55\times10^{-5}$ | (Mishra, Mishra, & Gupta, 2015) |
| | | Amplitude | 203 RIU$^{-1}$ | $4.9\times10^{-5}$ | |
| Silver-graphene deposited core | 1.46-1.49 | Wavelength | 3,000 nm/RIU | $3.33\times10^{-5}$ | (This work) |
| | | Amplitude | 418 RIU$^{-1}$ | $2.4\times10^{-5}$ | |

### 3.4.2  Performance Analysis and Optimization

The structural parameters of the fiber have huge influence on the sensing performance. The thickness of the active plasmonic material is important as it has significant effect on surface plasmon wave excitation. To observe the effect of silver layer thickness on the performance of sensor, the silver layer thickness is varied for the analyte RI at 1.46 and 1.47 while the other parameters remain constant. The loss spectrum and the amplitude sensitivity due to the change in silver layer thickness are shown in Figure 3.5. From Figure 3.5(a), the amplitude of the loss spectrum decreases gradually and shifts toward the longer wavelength with the increase of silver layer thickness from 35 nm to 45 nm, this is due to the higher damping loss for thicker silver layer (Lu et al., 2013).
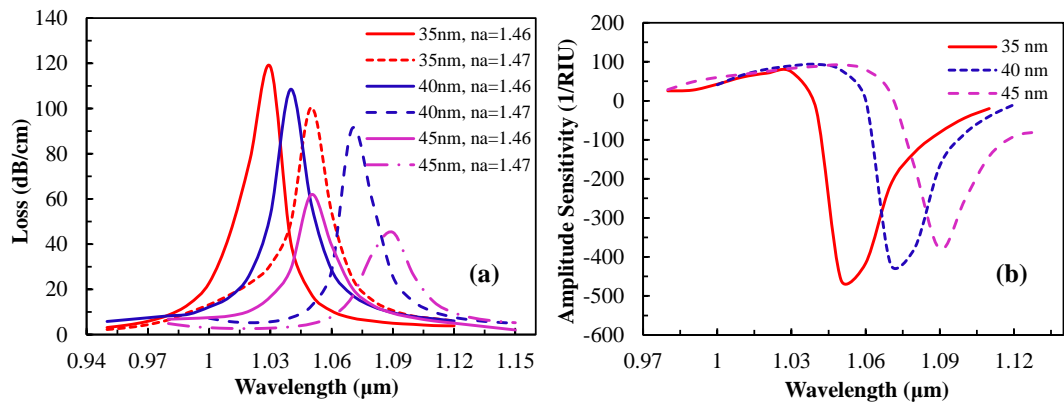
**Figure 3.5:** (a) Loss spectrum and (b) amplitude sensitivity versus wavelength by varying silver thickness, setting analyte RI at $n_a$=1.46.

This indicates that due to the increase of silver thickness, light penetration through the cladding decreases. The resonance peak shifts are 20, 30 and 40 nm for silver thickness of 35, 40 and 45 nm respectively. Figure 3.5(b) shows the same scenario, sensitivity decreases gradually due to the increase of silver thickness. The maximum amplitude sensitivity is achieved 458, 418 and 380 RIU$^{-1}$ for silver thickness of 35, 40 and 45 nm respectively at analyte RI of 1.46. This indicates the inverse relation between the sensitivity and the silver layer thickness. The increase of silver layer thickness leads to less penetration of the core mode electric field into the silver layer, resulting in weak coupling with the surface plasmon modes and subsequently affecting the sensitivity. The presence of evanescent fields in the silver layer decreases due to the larger thickness. The amplitude sensitivity of 458, 418 and 380 RIU$^{-1}$ gives sensor resolution of $2.2\times10^{-5}$, $2.4\times10^{-5}$ and $2.63\times10^{-5}$ respectively by assuming 1% minimum detectable change in the transmitted light intensity. The thickness of the silver layer is optimized at 40 nm for the study of the other parameters. This typical mechanism could be useful for the studies of nanoparticles concentration on the metal surface of a sensor (A Hassani & Skorobogatiy, 2006).

Besides the silver layer thickness, the effects of graphene layer thickness on the loss spectrum and amplitude sensitivity are studied and the related graphs are shown in Figure 3.6.
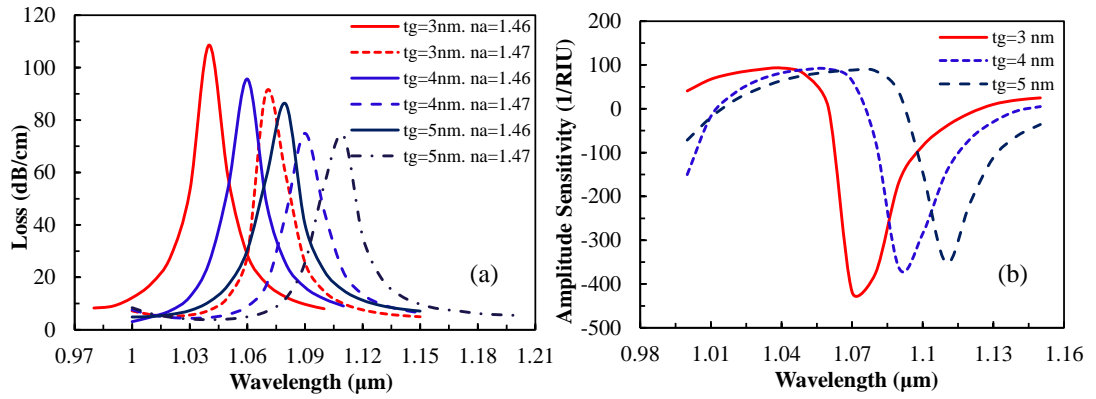


**Figure 3.6:** **(a)** Loss spectrum and (b) amplitude sensitivity as a function of wavelength by varying graphene layer thickness (analyte $n_a$=1.46 and silver layer thickness $t_{ag}$= 40 nm).

In Figure 3.6(a), as thickness of the graphene layer increases (3 nm to 5 nm), light confinement in the core improves, which causes less penetration of the core mode electric field into the cladding region. In Figure 3.6(b), as $t_g$ increases, amplitude sensitivity decreases gradually such that 418, 364 and 351 RIU$^{-1}$ is obtained for $t_g$ of 3, 4 and 5 nm respectively. This amplitude sensitivity leads the sensor resolution of $2.4\times10^{-5}$, $2.75\times10^{-5}$ and $2.85\times10^{-5}$ RIU respectively. The presence of evanescent field on the metal surface decreases due to the increase in $t_g$ which is in agreement with (Dash & Jha, 2014a). For SPR sensing, the graphene layer coating on plasmonic material (silver) shows better sensing performance as compared with silver layer without graphene coating. The performance of the sensor improves by 18% as compared to the silver on bimetallic due to the lower damping loss in graphene (Dash & Jha, 2014a).

In addition, the diameter of metallic core has significant effects on the surface plasmonic waves. By changing the metallic core diameters $d_c$ while retaining the analyte RI $n_a$=1.46, the loss spectrum is shown in Figure 3.7(a).
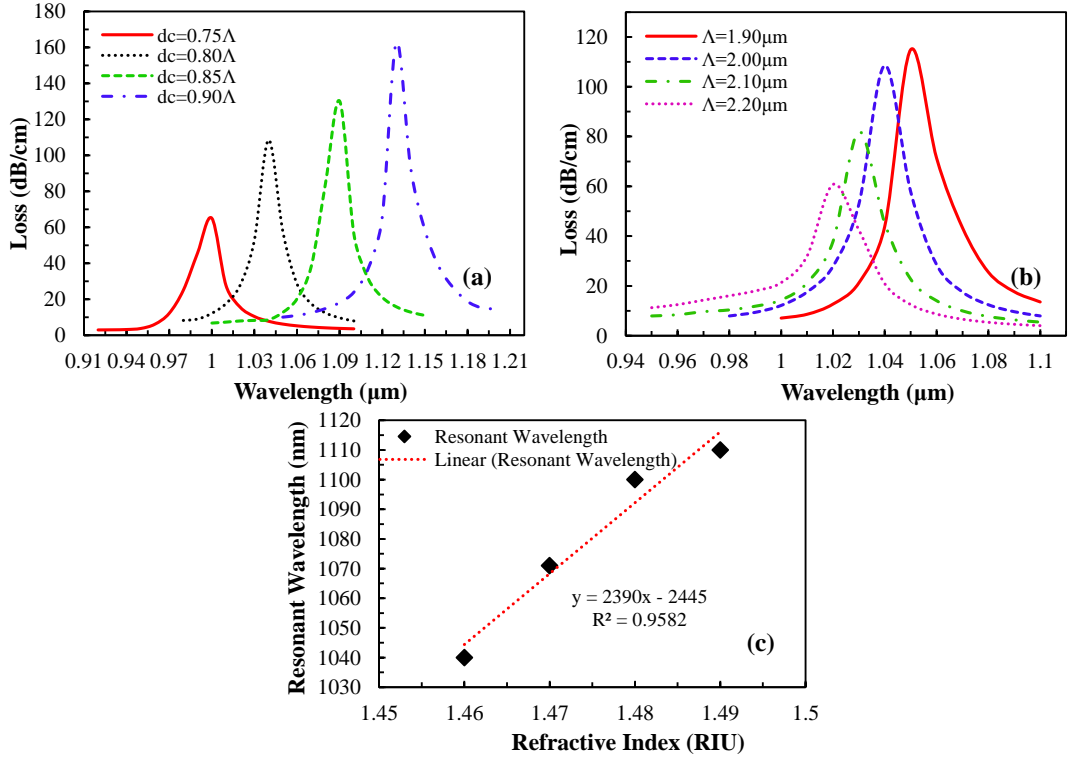
**Figure 3.7:** Loss spectrum versus wavelength with the variation of (a) metallic core diameter $d_c$, (b) pitch size $\Lambda$ (analyte RI, $n_a$=1.46) and (c) linear fitting of the fundamental mode resonant wavelength versus analyte RI.

As $d_c$ increases from $0.75\Lambda$ to $0.90\Lambda$, the resonant peak shifts toward longer wavelength and amplitude of the resonance peak increases gradually, this indicates stronger coupling between the core-guided fundamental mode and SPP modes. In addition, the effect of lattice constant $\Lambda$ on the sensing performance is shown in Figure 3.7(b). By increasing $\Lambda$, the amplitude of loss spectrum decreases whereas the resonant peak moves toward the shorter wavelength. Unlike increasing $d_c$, where the coupling strength between fundamental mode and SPP mode improves, enlarging $\Lambda$ causes the coupling strength to reduce. Therefore, $d_c$ and $\Lambda$ should be optimized simultaneously to achieve the optimum sensing performance, which have been found as $d_c$=0.80$\Lambda$ and $\Lambda$=1.90 µm, respectively. Figure 3.7(c) shows the linear line fitting of the resonant wavelength with respect to the analyte RI. The regression equation is, *y(nm)=2390x-2445* for 1.46$\leq$ *x*$\leq$1.49, where y is the resonant wavelength of the analyte in nm and x is the analyte RI. From Figure 3.7(c), the average sensitivity of the proposed sensor is 2390

nm.RIU$^{-1}$ and $R^2$ value is 0.9582, indicating good fitting of the sensor response. The obtained result is comparable with the results reported in (Yu et al., 2010). Owing to the high sensitivity and linearity, the sensor could be implemented as a standardized sensor for high RI analytes detection.

## 3.5 Summary

In this chapter, numerically investigate a PCF based SPR sensor where the core was deposited with graphene-silver. Graphene layer is used to inhibit oxidation of the active plasmonic material, silver. The metallic channel hole and the fiber cores are infiltrated with the sample, high RI liquid analyte. As the liquid-filled cores satisfy the optimum RI and dispersion relation simultaneously, SPR sensing performance is increased significantly. Amplitude sensitivity as high as 418 RIU$^{-1}$ has been demonstrated, which gives sensor resolution of $2.4 \times 10^{-5}$ RIU, assuming that the sensor is able to detect a minimum 1% change of the transmitted intensity. The proposed senor shows maximum RI sensitivity of 3000 nm/RIU with sensor resolution of $3.33 \times 10^{-5}$ RIU, whereas the average RI sensitivity is 2390 nm/RIU in the sensing range of 1.46 to 1.49. Due to the promising results, the proposed sensor could be a potential candidate for detecting chemical, organic-chemical, and other analytes.

# CHAPTER 4: FLAT FIBER BASED PLASMONIC SENSOR

## 4.1 Introduction

In this chapter, a simple liquid analyte filled multi-core flat fiber (MCFF) based Surface Plasmon Resonance (SPR) refractive index sensor operating in telecommunication wavelengths is proposed for refractive index sensing. Chemically stable gold (Au) and titanium dioxide ($TiO_2$) layers are used at external surface of the fiber structure to realize a simpler detection mechanism. Sensor performance is investigated by wavelength interrogation method and amplitude interrogation method.

## 4.2 Technical Review

Optical fibers are the natural candidate for distributed or remote optical sensing as they are mechanically flexible, immune to electromagnetic interference (EMI), low loss in telecom wavelengths and can be fabricated over kilometer-lengths. On the other hand, planar light wave circuits offer multifunctionality with the capability to sense multiple substances on a single platform. Flat optical fiber is a hybrid format of waveguide that combines the advantages of conventional optical fiber with the multifunctionality of planar waveguides (Adikan et al., 2012; Holmes et al., 2008). Recently, Egorova et al. (2014) and Mahdiraji et al. (2014) fabricated a new class of flat fiber called as Multi-Core Flat Fiber (MCFF), which opens a new window for designing more versatile photonic sensors due to having larger and flat surface functionality and flexibility in employing multiple waveguide channels with similar or different operating wavelengths. In this study, a novel, highly sensitive MCFF structure based SPR sensor is numerically demonstrated. Metallic layer and sensing layer are placed outside the fiber structure which made the proposed sensor simpler in terms of fabrication. The proposed sensor can be fabricated by following the MCFF method (Ghafour Amouzad Mahdiraji, 2015; G Amouzad Mahdiraji et al., 2014; Mahdiraji et al., 2014) and thin layer deposition

sputtering method (Malinský et al., 2012). Besides, selective liquid infiltration of holes in PCF can be done by selectively closing the holes using two-photon direct laser writing (Vieweg et al., 2010) and direct gluing method (Kuhlmey, Eggleton, & Wu, 2009). The detection of analyte can be carried out simply by flowing it through or dripped on the outer surface of metal layer. The proposed sensor can be calibrated with a liquid with known RI, using the flow cell analyte containing process. The effect of sensor structural parameters such as gold thickness, titanium dioxide thickness and core diameter on the plasmonic excitation is analyzed and optimized for the sensing performance as well as reducing the sensor footprint.

## 4.3 MCFF SPR Sensor Design and Theoretical Modeling
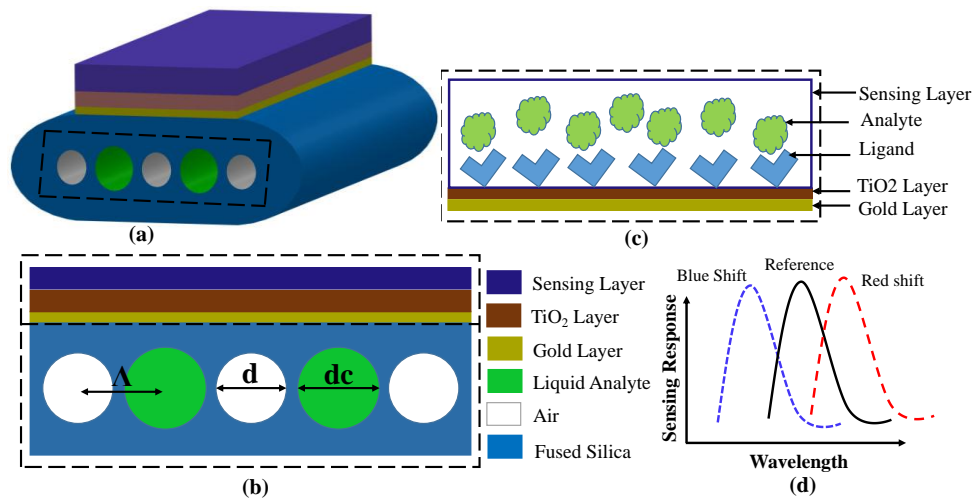


**Figure 4.1:** (a) Schematic of the proposed MCFF in 3D model, (b) cross-section of 2D computational model of MCFF SPR sensor, (c) Analyte flow through sensing layer: Ligands attached with TiO$_2$ layer, (d) Sensing response curve: reference peak (without analyte presence), shift right (red) or left (blue) with the presence of analytes.

Figure 4.1(a) shows the schematic of the proposed MCFF where the identical liquid cores and air-holes are arranged in a line. In principle, the number of liquid cores and air holes are scalable for desirable sensing application and is mainly limited by the fiber drawing technology. To simplify the fabrication process, gold layer, titanium dioxide layer and sensing layer are arranged sequentially on top of the MCFF surface, as shown

in Figure 4.1(b). Figure 4.1(c) is a conceptual diagram where analyte will flow through the sensing medium and bond with the ligands, resulting the shift in resonance peak. Due to the presence of analyte, resonance peak can be either blue or red shifted as shown in Figure 4.1(d). A higher refractive index liquid analyte (varies RI from 1.460 to 1.485) is used in the cores compare to the silica ($SiO_2$) to allow the total internal reflection (TIR) guiding mechanism. The proposed sensor has a pitch size of $\Lambda$=1.20 μm, core diameter $d_c$=1.20 μm and the air hole diameter is $d$=1 μm. Generally, Gold (Au) and silver (Ag) are widely used for the plasmonic applications due to their relatively low loss in the visible and near-infrared region (NIR) (West et al., 2010). Although, silver has low loss in the visible range, it is chemically unstable and it oxidizes easily. Gold is used as the active plasmonic material which is chemically stable and also having the higher resonance shift capability (Dash & Jha, 2014a). On top of the gold layer, a thin transparent high refractive index $TiO_2$ layer is deposited. The presence of $TiO_2$ layer will enhance the interaction of evanescent field with the analyte layer and shifted the resonant wavelengths towards the near-infrared wavelengths. Recently, Di Gao et al. reported the multi-hole based SPR sensor with the $TiO_2$ layer to operate the sensor at near-infrared region (2014). Gold layer is used outside the cladding with the fixed thickness $t$=40 nm and a $TiO_2$ layer above the gold layer with thickness $t_t$ = 80 nm. Sequentially, sensing layer is on top of the $TiO_2$ surface. The refractive index of the fused silica can be obtained by following the Eq. 2.26. The dielectric constant of gold is defined by the Drude-Lorentz model (Vial et al., 2005) and the equation is written as:

$$\varepsilon_{Au} = \varepsilon_{\infty} - \frac{\omega_D^2}{\omega(\omega + j\gamma_D)} - \frac{\Delta\varepsilon.\Omega_L^2}{(\omega^2 - \Omega_L^2) + j\Gamma_L\omega} \tag{4.1}$$

where $\varepsilon_{Au}$ is the permittivity of dielectric material, gold, $\varepsilon_{\infty}$ is the permittivity at high frequency and its value is 5.9673. The angular frequency can be expressed as $\omega = 2\pi C/\lambda$, $C$ is the velocity of light in vacuum. Moreover, $\omega_D$ and $\gamma_D$ are the plasma frequency and

damping frequency respectively, whereas $\Omega_D/2\pi$ = 2113.6 THz and $\gamma_D/2\pi$ = 15.92 THz. Weighting factor is expressed as $\Delta\varepsilon$ = 1.09 while, $\Gamma_L/2\pi$ = 104.86 THz and $\Omega_L/2\pi$ = 650.07 THz are the spectral width and oscillator strength respectively of the Lorentz oscillators.

The refractive index profile of TiO$_2$ is calculated by the following equation (DeVore, 1951).

$$n^2 = 5.913 + \frac{2.441 \times 10^7}{(\lambda^2 - 0.803 \times 10^7)} \tag{4.2}$$

Finite-element method based commercial COMSOL software is used to investigate the guiding properties and sensing performance. Outside the structure, PML and scattering boundary conditions are sequentially used to absorb the radiated light towards the surface.

## 4.4    Results and Discussions of the MCFF-SPR Sensor

MCFF SPR sensors are worked based on the evanescent field which is produced due to light propagation through the core. The core-clad arrangement in a line leads to leakage of light that produces more evanescent field. By keeping the metallic layer close to the cores which help to excite the free electrons of the metal layer easily to introduce the surface plasmon. At a certain wavelength, real effective index value of core-guided mode and real $n_{eff}$ of surface plasmon polaritons mode is equal, this wavelength is called the resonant wavelength. At the resonant wavelength, evanescent field can easily excite the free electrons of metal surface, resulting the generation of surface plasmon waves. The proposed design shows the two fundamental modes (x- and y-component modes), in this work y-component fundamental mode is analyzed to investigate the propagation loss. The x-component fundamental mode shows the same resonance peak similar to y-component but with lower loss depth. The fundamental core guided mode, SPP mode and the resonant spectrum at analyte refractive index $n_a$ = 1.46 is shown in Figure 4.2.
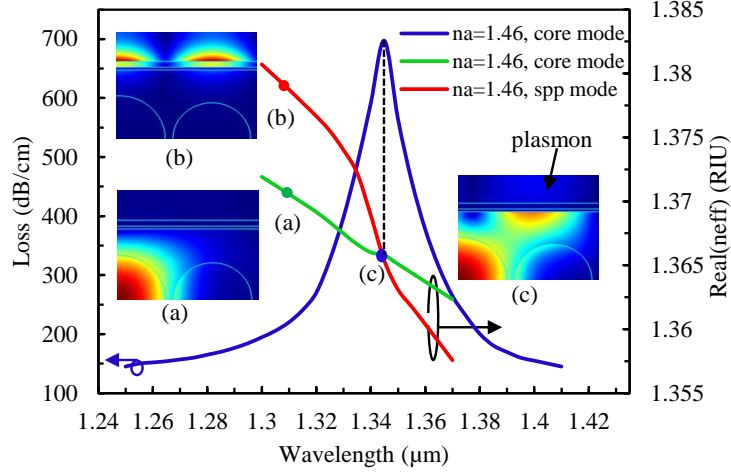
**Figure 4.2:** Dispersion relations of the plasmonic mode (red) and fundamental core mode (green), and loss spectrum (blue) with the structural parameters: $d_c = 1.20$ μm, $d = 1$ μm, $t = 40$ nm, $t_t = 80$ nm.

The real part of $n_{eff}$ of the core guided mode and the SPP mode are presented by the green and red solid line respectively. The effective index of the core-guided fundamental mode (green) and SPP mode (red) coincide at resonant wavelength 1.345 μm, where a sharp loss peak is found. This indicates the maximum energy transfer from the core-guided fundamental mode to the SPP mode. By using the imaginary part of $n_{eff}$, the propagation loss is defined by the following equation (Akowuah et al., 2012).

$$\alpha = 40\pi.Im(n_{eff}) / (ln(10)\lambda) \approx 8.686 \times k_0.Im[n_{eff}] \times 10^4 \text{ dB/cm} \qquad (4.3)$$

where $k_0 = 2\pi/\lambda$ is the wave number in the free space and the wavelength, $\lambda$ is in μm.

It is clearly visible from inset(a) that at the core guided fundamental mode, the electric field is well confined in the liquid core and the SPP mode, and from inset (b), the electric field is introduced on the metal surface outside the resonant wavelength. In inset (c), the fundamental core mode and SPP mode are phase matched at a given wavelength 1.345 μm. At this wavelength, the fundamental mode and the SPP mode are coupled together. A sharp loss peak appears at phase matching wavelength, providing a signature for detection of the analyte. The performance of proposed sensor is evaluated in terms of sensitivity, accuracy, linearity and resolution. The proposed sensor is very sensitive due

to small change of analyte. The small change of analyte RI induces a significant shift of loss peak. Figure 4.3 shows the response of the sensor for analyte RI from 1.46 to 1.485.
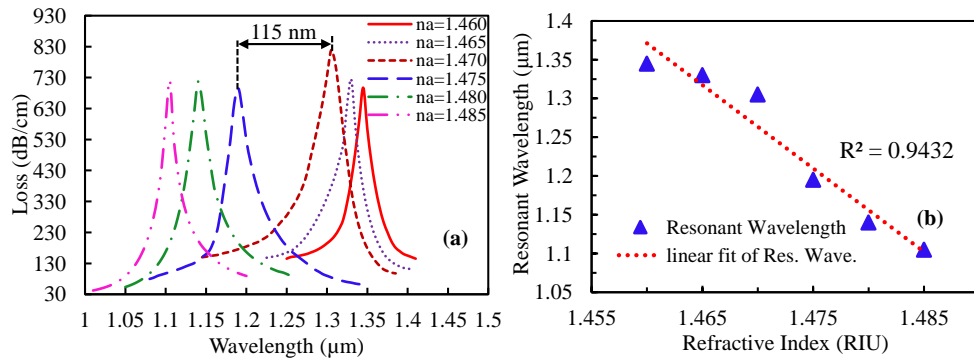


**Figure 4.3:** (a) Loss spectra of the fundamental mode with analyte RI $n_a$ varied from 1.46 1.485, (b) linear fitting of the fundamental mode resonant wavelength vs. analyte RI.

The real part of $n_{eff}$ of plasmonic mode depends strongly on the vicinity layer of analyte RI. Due to the small change of analyte RI, real part of the $n_{eff}$ of SPP mode changes, which causes the change of phase matching wavelength between the cores guided mode and the SPP mode. As depicted in Figure 4.3(a), by increasing the analyte RI, the loss peak shifts toward the shorter wavelengths, which is in agreement with the works reported in (Qin et al., 2014; Shuai, Xia, & Liu, 2012). The increase of analyte RI shifts the Real($n_{eff}$) of the SPP curve in Figure 4.2 (inset (c)) towards higher value collectively. As a result, the phase matching wavelength or resonance peak is shifted towards the lower wavelength. By varying the analyte RI with an iteration of 0.005, resonance wavelength shifts are 15, 25, 115, 50 and 35 nm, respectively towards the lower wavelength, as shown in Table 4.1. The highest sensitivity is observed within the analyte RI of 1.47 to 1.475, which provides the maximum loss peak shift 115 nm, i.e., from 1.305 to 1.190 μm. Moreover, the maximum loss peak value 818 dB/cm is achieved at 1.305 μm wavelength and the minimum loss peak value is achieved 695 dB/cm at 1.190 μm wavelength while the analyte RI are 1.47 and 1.475, respectively. Generally, microstructured optical fiber based SPR sensors show high propagation loss, as a result, it limits the sensor length to generate

the measurable signal to detect the unknown analytes (A Hassani & Skorobogatiy, 2006). The sensitivity of the proposed sensor is analyzed by using the wavelength interrogation and amplitude interrogation method. The sensitivity of wavelength interrogation is measured by the following equation (Alireza Hassani et al., 2008),

$$Sensitivity, \ S_{\lambda \ [nm/RIU]} = \Delta\lambda_{peak} / \Delta n_a \qquad (4.4)$$

where $\Delta\lambda_{peak}$ is the resonance peak shift and $\Delta n_a$ is the variation of the analyte refractive index.

The proposed MCFF sensor shows the maximum sensitivity of 23000 nm/RIU, at the analyte RI of 1.47 and the average sensitivity of the sensor is 9600 nm/RIU. The resonance peaks are found at 1.345, 1.330, 1.305, 1.190, 1.140 and 1.105 µm wavelength where the full-width-at-half-maximum (FWHM) values are 36, 43, 54, 46, 41 and 29 nm for the analyte refractive index 1.46, 1.465, 1.47, 1.475, 1.48 and 1.485, respectively, as shown in Table 4.1. Besides, detection accuracy of a sensor is the reciprocal of FWHM, i.e. $D_n = 1/FWHM$ (Dash & Jha, 2015a). Therefore, lower FWHM values means the sharper resonance curve resulting the higher detection accuracy. Furthermore, as depicted in Figure 4.3(b), the proposed sensor shows the linearity $R^2$ value of 0.9432 in the sensing range of 1.46 to 1.485, which indicates the high linear sensing response. Assuming the minimum spectral resolution of $\Delta\lambda_{min} = 0.1$ nm and considering the maximum peak shift $\Delta\lambda_{peak} = 115$ nm, which is obtained based on the analyte RI variation of $\Delta n_a = 0.005$, as shown in Figure 4.3(a), the RI resolution can be calculated as following equation (Gao et al., 2014).

$$R = \Delta n_a \times \Delta\lambda_{min} / \Delta\lambda_{peak} \ RIU \qquad (4.5)$$

The resolution of the proposed sensor is as high as $4.35 \times 10^{-6}$ RIU, which indicates capability of the sensor in detecting very small RI changes in the order of $10^{-6}$. The resolution of the proposed sensor is better compared to the results reported in (Dash & Jha, 2014b; Shuai, Xia, & Liu, 2012).

**Table 4.1:** Performance analysis with the variation of analyte RI.

| Analyte RI | Resonance peak wavelength (μm) | Resonance peak shift (nm) | Sensitivity [nm/RIU] | FWHM (nm) |
|---|---|---|---|---|
| 1.460 | 1.345 | 15 | 3000 | 36 |
| 1.465 | 1.330 | 25 | 5000 | 43 |
| 1.470 | 1.305 | 115 | 23000 | 54 |
| 1.475 | 1.190 | 50 | 10000 | 46 |
| 1.480 | 1.140 | 35 | 7000 | 41 |
| 1.485 | 1.105 | - | - | 29 |

The performance comparisons of the proposed sensor against the previously reported SPR sensors are presented in Table 4.2.

**Table 4.2:** Performance comparison of simulated SPR sensors.

| Structural configuration of RI sensor | Wave. interrogation sensitivity, nm/RIU | Amp. Sens., RIU-1 | Resolution (using wav. inter.), RIU | Ref. |
|---|---|---|---|---|
| Bragg fiber based SPR sensor | 1,2000 | 269 | $8.3 \times 10^{-6}$ | (Alireza Hassani et al., 2008) |
| Hollow core D-shaped PCF SPR sensor | 6,430 | N/A | N/A | (Tan et al., 2014) |
| Liquid core PCF based SPR sensor | -5,000; 3,700 | N/A | $2.7 \times 10^{-6}$ | (Shuai, Xia, & Liu, 2012) |
| Solid core D-shaped PCF SPR sensor | 7300 | N/A | N/A | (Tian et al., 2012) |
| Graphene based PCF based SPR sensor | N/A | 860 | N/A | (Dash & Jha, 2014a) |
| Solid core honeycomb PCF SPR sensor | 13,750 | 400 | N/A | (Gauvreau et al., 2007) |
| Exposed-core grapefruit fiber | 13,500 | N/A | N/A | (Rhodes et al., 2008) |
| MCFF based SPR sensor | 23,000 | 820 | $4.35 \times 10^{-6}$ | (This work) |

The thickness of the gold layer is influential on the sensing performance as well. The effect of analyte RI and gold thickness changes on the loss spectrums are shown in Figure 4.4. Figure 4.4 shows the blue shift of the loss spectrum with the increase of gold layer thickness. At thickness of $t$=40 nm, the maximum losses of 697 dB/cm and 723 dB/cm are achieved at resonant wavelength 1.345 μm and 1.330 μm due to analyte RI of 1.460 and 1.465, respectively. The variation in Au layer thickness will affect the real $n_{eff}$ of the surface plasmon mode, thus causing the shift in phase matching wavelength. Au layer thickness will affect the real $n_{eff}$ of the surface plasmon mode, thus causing the shift in phase matching wavelength. In addition, it is visible that the loss depth of the sensor is decreased with thicker Au layer as indicated in Figure 4.4. This is because as the thickness of Au layer is increased, the penetration of evanescent field towards the surface is less. The variation in loss depth is a critical issue as it will affect the sensitivity of the sensor in amplitude interrogation mode. Practically, the thickness of the Au layer should be determined specifically for optimum sensing performance in wavelength or amplitude interrogation.
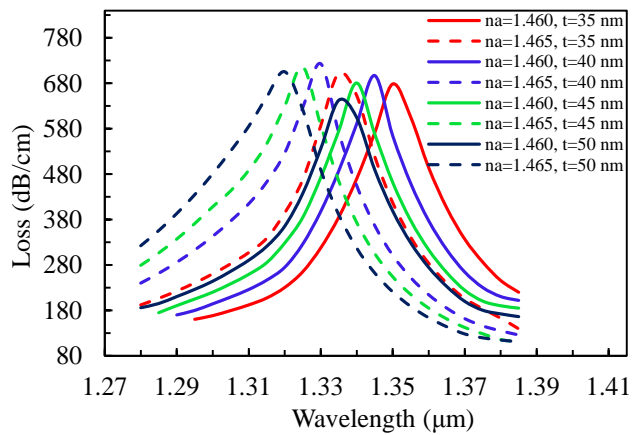


**Figure 4.4:** Loss spectrum of wavelength with the variation of gold thickness t from 35-50 nm, by setting $n_a$=1.46, $d_c$=1.20 μm and $t_t$=80 nm.

Besides the gold layer thickness, effects of TiO$_2$ layer thickness on sensing performance are investigated. TiO$_2$ attracts the core-guided evanescent fields towards the surface and help to facilitate the interaction between the core-guided mode and the SPP

mode. Due to its high refractive index, it turns the sensor operation in near-infrared region (Gao et al., 2014). The effect of loss spectra due to variation of $TiO_2$ thickness from 70 to 85 nm are shown in Figure 4.5(a).
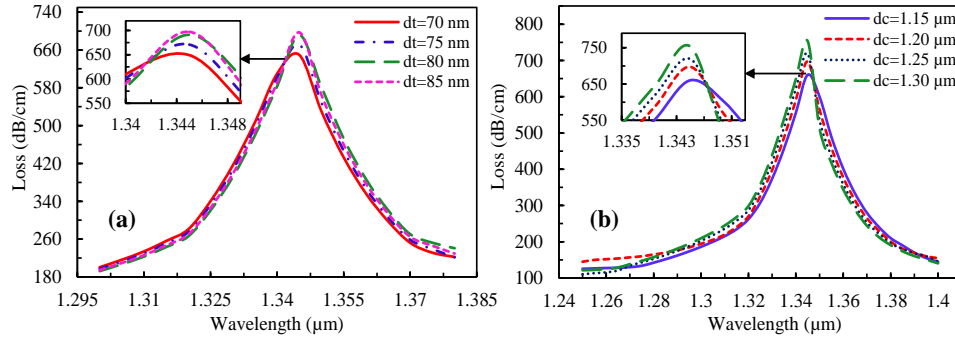


**Figure 4.5:** Loss spectrum analysis with varying the (a) $TiO_2$ thickness, and (2) liquid core-diameter ($d_c$); setting $n_a$= 1.46, $d$= 1 μm, and $t_g$= 40 nm.

It is clearly observed that the loss peaks appear at 1.345 μm wavelength and the loss depths are increase slightly with the increment in $TiO_2$ thickness. The minimum loss value 649 dB/cm is achieved while the $TiO_2$ thickness is 70 nm and it increased to the maximum loss value of 697 dB/cm at the thickness of 85 nm. Due to increase of $TiO_2$ thickness, evanescent field is attracted towards the surface and interacts strongly with the analytes, thereby, the loss depths are gradually increased. The core diameter effects on the sensing performance also considered, as shown in Figure 4.5(b). Due to change of liquid-filled core diameter $d_c$ from 1.15 to 1.30 μm, resonance peaks are found to be around 1.345 μm with very small shift toward the lower wavelength and slightly gaining in the resonance depths. At the core-diameter 1.15 μm, loss value 660 dB/cm is achieved, while it is dramatically increased to 753 dB/cm when the $d_c$ is increased to 1.30 μm. This indicates the stronger coupling between the core-guided fundamental mode and SPP mode with the increase of $d_c$.

Furthermore, the performance of the sensor is evaluated by the mean of amplitude detection method. Spectral manipulation is not necessary in this method as all the measurement operations are done in a specific wavelength (Gauvreau et al., 2007). The

effect of analyte RI and gold thickness variation on amplitude sensitivity is shown in Figure 4.6(a) and (b), respectively, considering the optimum core diameter of $d_c$=1.20 µm. The amplitude sensitivity can be calculated by following the Eq. 3.1.
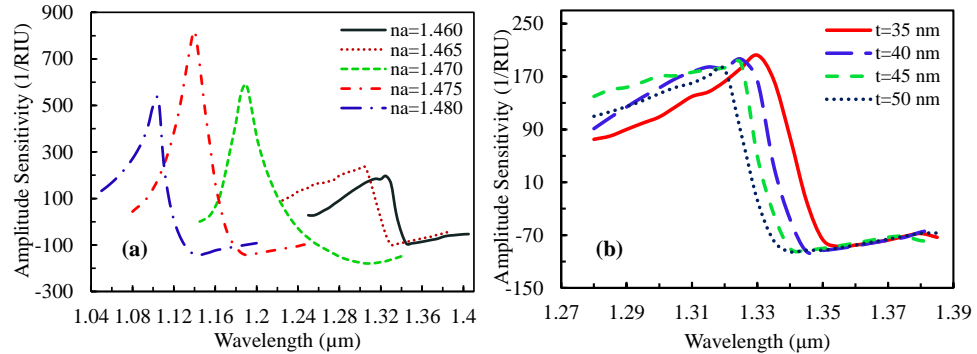


**Figure 4.6:** Dependence of the sensor amplitude sensitivity (a) with the variation of analyte RI; (b) with the variation of gold thickness at analyte RI, $n_a$=1.460.

As shown in Figure 4.6(a), the maximum amplitude sensitivity of 820 RIU$^{-1}$ is obtained at 1140 nm wavelength for the analyte RI $n_a$=1.475. The proposed amplitude sensitivity result is comparable with the results reported in (Gao et al., 2014; Alireza Hassani et al., 2008). The proposed sensor resolution 1.22×10$^{-5}$ RIU is achieved (considering amplitude sensitivity 820 RIU$^{-1}$), by assuming the minimum 1% change of the transmitted intensity is detectable. Amplitude sensitivities of 196, 233, 590 and 534 RIU$^{-1}$ are achieved for the other analyte RI of 1.46, 1.465, 1.47 and 1.48, respectively. The amplitude sensitivity is found to be inversely proportional to the gold thickness as depicted in Figure 4.6(b). The maximum amplitude sensitivity achieved is 202 RIU$^{-1}$ at 1.330 µm for the gold thickness of 35 nm. This implies the sensing resolution of 4.95×10$^{-5}$ RIU with the same assumption of 1% change of the transmitted intensity. Moreover, amplitude sensitivity of 196, 190 and 181 RIU$^{-1}$ are achieved with the gold thicknesses of 40, 45 and 50 nm, respectively. By increasing the gold thickness, sensitivity is decreased significantly, due to the higher damping loss for the thicker gold layer. Owing to the high wavelength sensitivity, amplitude sensitivity and high sensor resolution, the

proposed sensor could be implemented as a standardized sensor for the high RI analytes detection.

## 4.5　Summary

A simple multi-core flat fiber structure based surface plasmon resonance sensor is demonstrated for the first time. The proposed sensor shows a sensitivity as high as 23,000 nm/RIU, which is highest among the reported microstructured SPR sensors. As the liquid-filled cores satisfy the optimum index and dispersion property simultaneously, the SPR sensing performance is increased significantly. The proposed sensor shows the average sensitivity of 9,600 nm/RIU, at the sensing RI range of 1.46-1.485. The proposed sensor shows high sensing resolution as high as $\sim 4.35 \times 10^{-6}$ RIU. Additionally, the proposed sensor offers a maximum amplitude sensitivity and sensor resolution of 820 $RIU^{-1}$ and $1.22 \times 10^{-5}$ RIU, respectively. The results demonstrate the feasibility of MCFF based SPR sensor towards the possibility of integrated SPR sensor-on-a-chip. Multiple cores along the MCFF could enable a real time monitoring of different physical and biological analytes.

# CHAPTER 5: PCF SPR WITH EXTERNAL SENSING APPROACH

## 5.1 Introduction

In this chapter, a simple, two rings, hexagonal lattice PCF biosensor using Surface Plasmon Resonance phenomenon is proposed. An active plasmonic gold layer and the analyte are placed outside the fiber structure instead of inside the air-holes, which will result in a simpler and straight forward fabrication process. The proposed sensor exhibits birefringent behavior that enhances its sensitivity. Numerical investigation of the guiding properties and sensing performance are conducted by FEM. Finally, fabrication tolerance is shown to make the sensor feasible.

## 5.2 Technical Review

Recently, by integrating the SPR phenomenon, PCF has shown great potential for biosensing due to its special characteristics, such as small size and design flexibility (Dash & Jha, 2014a). By modifying the structure and dimension of PCF, it is possible to increase the evanescent field and manipulate the modal characteristics of the propagating light. To enhance the sensitivity and realize the narrow resonance peak, single mode light propagation is more suitable (Shuai, Xia, Zhang, & Liu, 2012). Recently, multi-hole fiber based SPR sensor was proposed by Gao et al. (2014), where all the holes were coated with gold and titanium dioxide. To realize the multi-analytes detection, Akowuah et al. proposed the elliptical air-hole PCF-SPR sensor with four micro fluidic slots (2012). Besides, high refractive index (RI) analytes, selectively gold coated with analyte-filled core had been proposed by Qin et al. (2014). In such PCF based SPR sensors where metal layer need to be coated inside the fiber-holes; one of the major challenge is to achieve uniform coating inside the micrometer diameter capillary holes. Additional drawback is

that the liquid has to be selectively infiltrated into the fiber holes, which limits its practical implementation. To eliminate these practical challenges and limitations, recently, several PCF based SPR sensors are reported where the metal coating and the sensing layers are applied on the outer surface of the fiber structure. Tan et al. (2014) proposed a D-shape PCF providing a flat outer surface for the metal and sensing layers, however, this requires accurate polishing effort to precisely remove a predetermined portion of the PCF. In other studies, proposed two irregular PCF structures where the SPR sensing layer is placed at the outer surface of the fiber (Dash & Jha, 2014a). Fabrication of such irregular PCF structures that requires different sizes of holes to be placed in specific positions in the fiber geometry, which is practically challenging even with very accurate fiber preform drilling systems.

In this chapter, a simple PCF biosensor based on SPR is proposed. Since the sensing layers of the proposed sensor are located at outside of the PCF, detection of the unknown analyte can be carried out simply by flowing it through or dripped on the outer surface of metal layer. Gold is used as the plasmonic material since it is chemically stable in aqueous environment and shows high resonance peak shift (Dash & Jha, 2014a). The proposed sensor in this work could be fabricated easily using standard stack-and-draw PCF drawing method (G Amouzad Mahdiraji et al., 2014) and sputter deposition method (Malinský et al., 2012). In addition, the effect of gold layer for plasmonic excitation are investigated and optimized for the sensing performance, as well as reducing the sensor footprint.

## 5.3    Structural Design and Theoretical Modelling

Figure 5.1(a) shows the cross-section of the proposed PCF preform structure based on the stacking of different capillaries (G Amouzad Mahdiraji et al., 2014). Figure 5.1(b) shows the cross-section of the proposed sensor. Here, propose a two-ring, hexagonal lattice PCF with a small central air hole which facilitates phase matching between the core-guided fundamental mode and the surface plasmon polaritons mode. Two holes in

the first ring next to the central hole are omitted to introduce birefringence effect. Two air-holes in the second ring at the same row with the central air-hole are scaled down to concentrate the evanescent field at two opposite sides of the fiber so that the surface plasmon could be excited efficiently. The proposed PCF structure can be fabricated by introducing solid rods and capillaries with thicker wall, as shown in Figure 6.1(a).
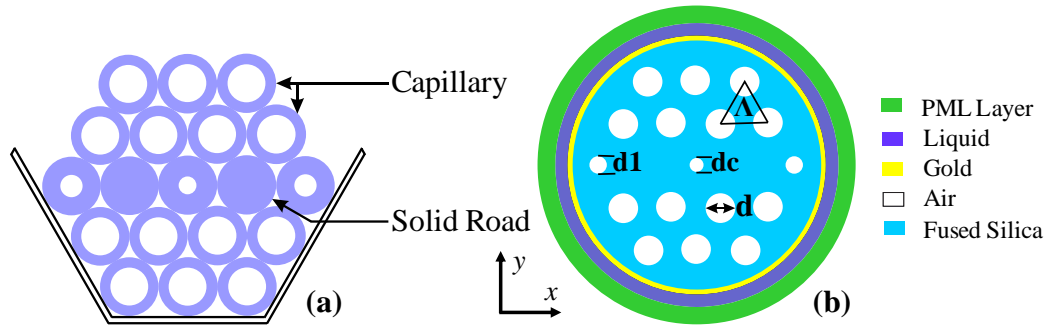


**Figure 5.1:** Cross-section of the proposed (a) PCF's stacked preform, (b) sensor.

All the air-holes are in circular shape. As shown in Figure 5.1(b), air-holes diameters are $d_c = 0.15\Lambda$, $d_l = 0.25\Lambda$ and $d = 0.5\Lambda$. Hole-to-hole distance (pitch size) is $\Lambda = 2$ μm. The refractive index of fused silica used in the modeling follows the Sellmeier equation (Akowuah et al., 2012). At the outer surface of the fiber structure, a thin gold layer with a fixed thickness ($d_g$= 40 nm) is used as the plasmonic material. This kind of thin layer can be integrated outside the fiber structured by using sputtering technique, high pressure CVD technique, etc. (Malinský et al., 2012; Sazio et al., 2006). The dielectric constant of gold is defined by Drude-Lorentz model (Vial et al., 2005). On top of the gold layer is the sample (analyte), which is defined as a dielectric layer. The performance of the proposed sensor is numerically studied using FEM based commercial COMSOL software with a circular PML, which prevents reflection by absorbing the scattered light from the structure.

## 5.4    Results and Performance Analysis

The working principle of the PCF-SPR sensors is based on the interaction of evanescent field with the metal layer. Light propagating in the core produces evanescent field that penetrates through the cladding region. At a resonant wavelength, real part of the core guided effective refractive index and the surface plasmon effective refractive index are equal. The core-clad evanescent field excites the free electrons of the metal surface, as a result, surface plasmon wave is generated. A sharp loss peak appears at the resonant wavelength and the RI of the unknown analyte could be detected via wavelength shift or amplitude variations of this peak. Due to the birefringence, the proposed sensor shows two fundamental modes. As depicted in Figure 5.2(a), $y$-component shows higher effective index profile as compared to $x$-component. Moreover, the proposed sensor shows higher fundamental mode resonance loss peak using the $y$-component as compared to the $x$-component mode. In the following work, $y$-component fundamental mode is considered. The proposed sensor's electric field profile and phase matching property are shown in Figure 5.2 with analyte RI, $n_a$=1.36.
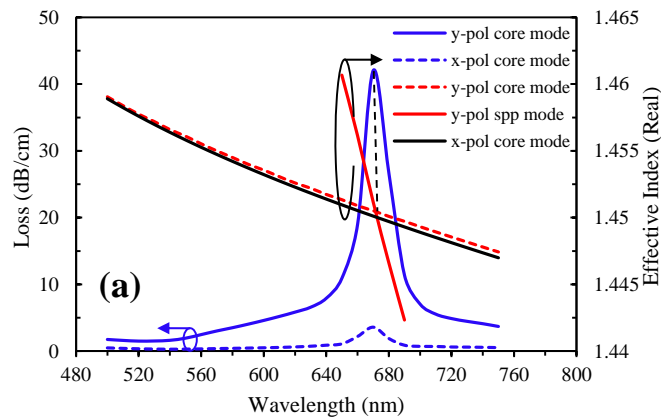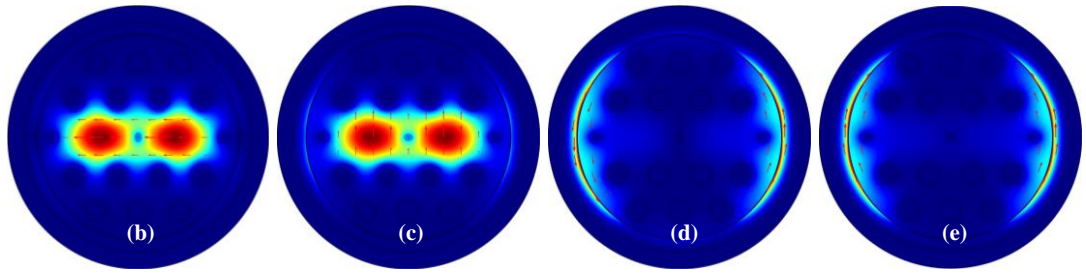
**Figure 5.2:** Field profile of the proposed sensor at analyte RI 1.36, (a) dispersion relations of fundamental mode and SPP mode; (b) and (d) *x*-component fundamental core guided mode and SPP mode, respectively, (c) and (e) *y*-component fundamental core guided mode and SPP mode, respectively.

Figure 5.2(b) and (c) show the core-guided fundamental mode for *x*-component and *y*-component, respectively. When the light is propagating through the core, y-component light is refracted towards the surface compared to the x-component light. It is clearly visible that the *y*-component electric field is stronger in the sensing layer as compared with the *x*-component. The intensity of electric field on the metal surface indicates the sensitivity level. Figure 5.2(d) and (e) show the SPP mode for *x*-component and *y*-component, respectively. Additionally, Figure 5.2(a) shows the phase matching at 670 nm where the effective index of the core-guided fundamental mode and SPP mode coincide for the analyte with RI 1.36. At the resonant peak of 670 nm, largest energy is transferred from core-guided fundamental mode to SPP mode, when both modes are strongly coupled. The phase matching coupling phenomenon is verified by the coincidence of the resonant peak and the intersection between the dispersion relations of the core-guided mode and SPP mode. The confinement loss is calculated by Eq. 4.3.

The real part of the surface plasmon mode effective index is strongly influenced by the analyte refractive index. This in turn determines the wavelength for the phase matching condition between the core guided mode and surface plasmon polaritons modes. Figure 5.3 shows the peak wavelength shift resulted by varying the analyte RI from 1.33 to 1.37. The increase of analyte RI will shift the Real($n_{eff}$) of the SPP curve shown in Figure 5.2(a) towards higher value collectively.
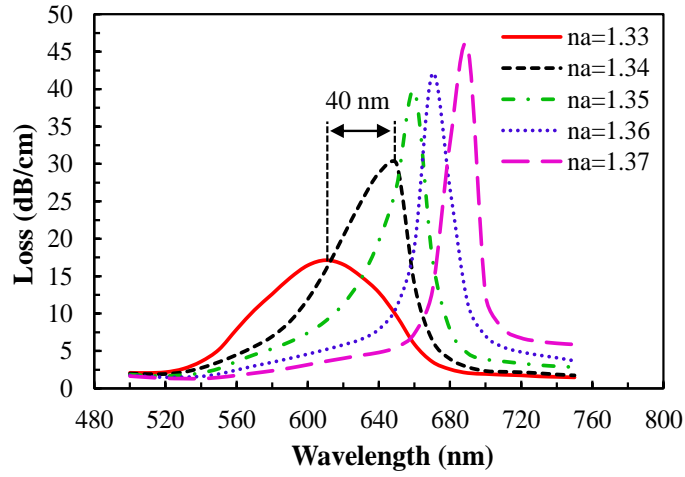
**Figure 5.3:** Fundamental loss spectrums by varying the analyte RI from 1.33 to 1.37 ($d_c$=0.15Λ, $d_l$=0.25Λ, $d$=0.5Λ and $t_g$=40 nm).

As a result, the phase matching wavelength or resonance peak is shifted towards the longer wavelength. By increasing the analyte RI, resonance peak shifts toward the longer wavelength and the loss depth is increased simultaneously due to the lower core-cladding index contrast. Lower resonant depth was observed with analyte of RI at 1.33. This indicates weaker energy transfer from the core guided mode to the SPP mode, which results in the broadening of resonant spectrum (Shuai, Xia, & Liu, 2012). Using wavelength interrogation method, the proposed sensor shows maximum positive sensitivity of 4000 nm/RIU and the sensing resolution is $2.5 \times 10^{-5}$ RIU (by assuming the wavelength resolution is 0.1 nm). The wavelength interrogation sensitivity of the proposed sensor is comparable to work reported in (Gao et al., 2014; Qin et al., 2014; Zhang, Yao, Cui, & Lu, 2013) with simpler structure. The sensitivity of wavelength interrogation is determined by $S_\lambda(\lambda) = \Delta\lambda_{peak}/\Delta n_a$ (Akowuah et al., 2012); where, $\Delta n_a$ is the analyte RI variation and the $\Delta\lambda_{peak}$ is the peak shift. The resonant peaks are found at 660, 670 and 690 nm wavelength for the analyte RI of 1.35, 1.36 and 1.37, respectively. The sensitivity of 1000, 1000 and 2000 nm/RIU are achieved when the analyte RI changes from 1.34-1.35, 1.35-1.36 and 1.36-1.37, respectively. The change of analyte RI will affect the $n_{eff}$ of SPP mode, core mode $n_{eff}$, penetration depth of the SPP field, etc.

simultaneously. The cross effect of those affected properties contributed to arbitrary variation in wavelength shift magnitude. Practically, a calibration factor is required for each range of analyte RI. From the wavelength interrogation method, the proposed sensor shows the higher sensitivity as compared to the amplitude interrogation method. Amplitude interrogation sensitivity is measured at a specific wavelength which makes the technique simpler and cost effective as compared to the wavelength interrogation method (Jiří Homola et al., 1999). By varying the analyte RI, the amplitude sensitivity is shown in Figure 5.4.
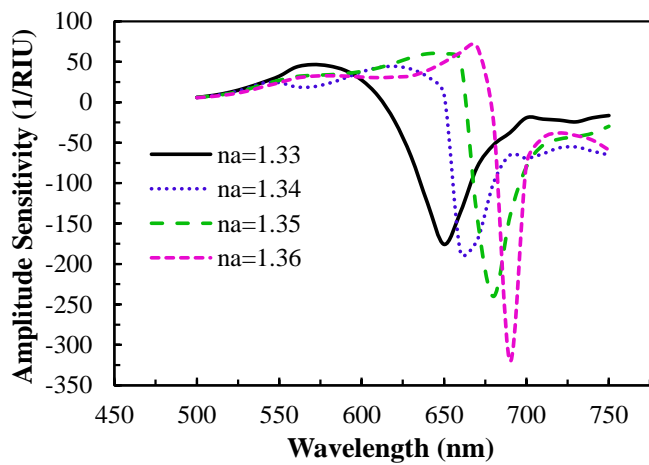


**Figure 5.4:** Amplitude sensitivity is a function of wavelength ($d_c$=0.15Λ, $d_l$=0.25Λ, $d$=0.5Λ and $t_g$=40 nm).

Amplitude sensitivity is calculated by using Eq. 3.1. From Figure 5.4, with the increase of analyte RI, the amplitude sensitivity increases gradually. For detecting analyte with RI of 1.36, the proposed sensor shows the maximum amplitude sensitivity of 320 RIU$^{-1}$ which is comparable to (Gao et al., 2014). Additionally, amplitude sensitivities of 176, 184 and 240 RIU$^{-1}$ are obtained for analytes with RI of 1.33, 1.34 and 1.35 respectively. Besides, the resolution of the proposed sensor is 3.125×10$^{-5}$, by assuming a minimum of 1% transmitted intensity to be detected accurately. Generally, the sensitivity of PCF based SPR sensors depend on the evanescent fields. Stronger evanescent fields results in higher transmission loss in the fiber. However, it increases the interaction with the metal surface

and subsequently improves the sensor sensitivity. Given the high loss at resonant peak, only a few millimeters of sensing length is required to achieve observable signal with the proposed sensor. Therefore, reducing the amount of analyte for detection.

Table 5.1 shows the performance comparison of the reported PCF SPR sensors.

**Table 5.1:** Performance comparison of simulated PCF SPR sensors.

| Characteristics | RI Range | Interrogation | Sensitivity | Resolution (RIU) | Ref. |
|---|---|---|---|---|---|
| Multichannel PCF | 1.33-1.39 | Wavelength | 4,600 nm/RIU | $2\times10^{-5}$ | (Otupiri et al., 2015) |
| Graphene based D-shaped fiber | 1.33-1.37 | Wavelength | 3,700 nm/RIU | $2.7\times10^{-5}$ | (Dash & Jha, 2015b) |
| | | Amplitude | 216 RIU$^{-1}$ | $4.6\times10^{-5}$ | |
| Scaled down hollow-core D-shaped fiber | 1.33-1.34 | Wavelength | 2,900 nm/RIU | N/A | (Luan et al., 2015) |
| | | Amplitude | 120 RIU$^{-1}$ | N/A | |
| | | Phase | 50,300 deg/RIU/cm | N/A | |
| Simple external sensing approach | 1.33-1.37 | Wavelength | 4,000 nm/RIU | $2.5\times10^{-5}$ | (This Work) |
| | | Amplitude | 320 RIU$^{-1}$ | $3.12\times10^{-5}$ | |

The thickness of gold layer has a significant impact on the sensing performance. The change of sensing performance by changing the layer thickness is shown in Figure 5.5. Figure 5.5(a) shows the red shift of the loss spectrum with the increase of gold layer thickness. At thickness of $t_g$=40 nm, the maximum losses of 40 dB/cm and 42 dB/cm occur at 660 nm and 670 nm due to analyte RI of 1.35 and 1.36, respectively. For the wavelength interrogation, it shows the sensitivities of 1000, 1900 and 2000 nm/RIU at the gold thickness of 40, 50 and 60 nm, respectively when the analyte RI is 1.35. As the thickness of Au layer is increased, the $n_{eff}$ of SPP mode bound in Au layer is higher, resulting in the red shift of phase matching wavelength. The loss depth decreases gradually with the increasing thickness of gold layer. The same scenario is also observed for amplitude sensitivity, as shown in Figure 5.5(b), with the increase of gold layer

thickness, amplitude sensitivity decreases gradually. This indicates less penetration of the core mode into the gold layer due to the larger thickness.
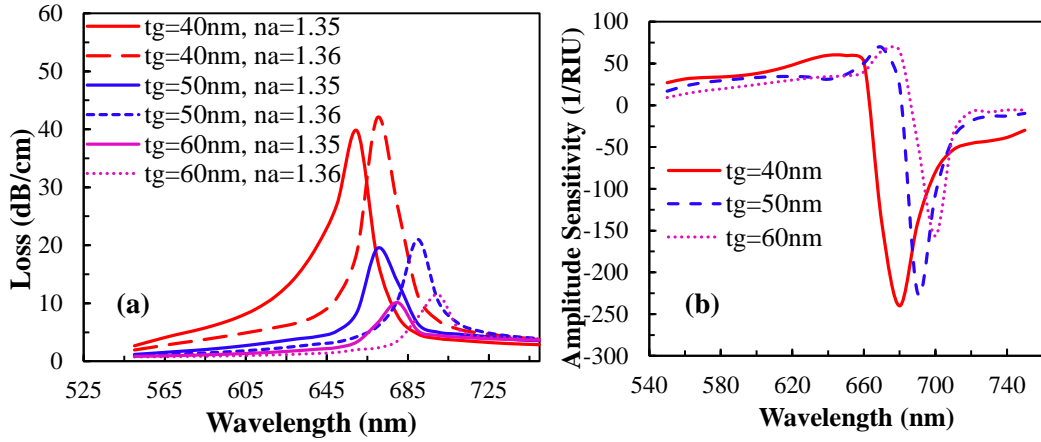


**Figure 5.5:** (a) Loss spectrum and (b) amplitude sensitivity for different gold layer thicknesses ($d_c$=0.15Λ, $d_l$=0.25Λ, and $d$=0.5Λ).

Also, the thicker gold layer will give rise to higher damping loss of gold metal. The maximum sensitivity is 240 RIU$^{-1}$ at 680 nm when the gold thickness is $t_g$=40 nm. The amplitude sensitivity decreases to 225 and 157 RIU$^{-1}$ when the gold thicknesses are 50 and 60 nm, respectively. The gold $t_g$=40 nm is optimized thickness considering better signal to noise ratio. The phase matching point is shifted with the changes of $t_{ag}$ thickness, this mechanism would be useful to study the nanoparticles interaction on the metal surface of a sensor. Additionally, another practical approach is to monitor the concentration of nanoparticles for the study of photodynamic cancer therapy (Cinteza et al., 2006).

Besides, the effects of the changes of structural parameters such as central air-hole diameter ($d_c$), scaled-down air-holes diameter ($d_l$) and the surrounding air-holes diameter ($d$) on plasmonic excitation are shown in Figure 5.6. The other parameters are kept unchanged.
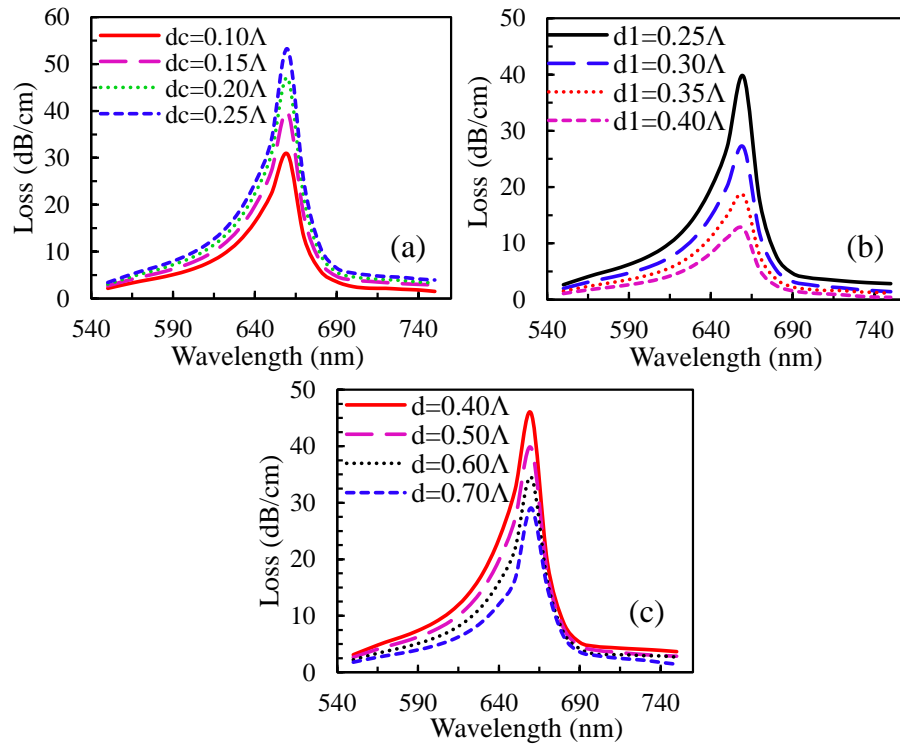
**Figure 5.6:** Effect of confinement loss due to the change of (a) central air-hole diameter, $d_c$, (b) scaled-down air hole diameter ($d_1$) and (c) surrounding air-holes diameter, d (setting the analyte RI $n_a$=1.35 and $t_g$=40 nm).

As shown in Figure 5.6(a), with the increase of central air-hole diameter ($d_c$), loss peak maintains at 660 nm wavelength but the loss depth increases gradually. The size of the central air-hole is optimized as $d_c$=0.15Λ. If the diameter is reduced further, light will propagate entirely in the core which will then reduce the intensity of evanescent field that overlaps the metal-dielectric interface. Also, if the central air-hole diameter is increased, it will lead to the reduction of the effective index of core thereby weakening the guidance along the core. On the other hand, Figure 5.6(b), shows the increase of scaled-down air-hole size ($d_1$), loss peak maintains at the resonant wavelength 660 nm while the loss depth decreases significantly, which indicates light is more confined in the core. Figure 5.6(c) shows the same scenario as Figure 5.6(b), where the increase of air-hole diameter *d* causes light to be more confined in the core. The loss peak is unchanged at 660 nm.

## 5.5    Summary

A simple PCF SPR sensor is proposed by keeping the metallic layer and liquid (sample) outside of the fiber structure. The proposed sensor is numerically studied by using FEM and the sensor parameters are optimized for sensing performance. The proposed sensor shows maximum wavelength interrogation sensitivity of 4000 nm/RIU with resolution as high as $2.5 \times 10^{-5}$ RIU. Besides, the maximum amplitude sensitivity is 320 RIU$^{-1}$ with resolution of $3.125 \times 10^{-5}$ RIU. Proposed sensor is feasible to be fabricated with current PCF stack-and-draw method and sputter deposition technology.

# CHAPTER 6: COPPER-GRAPHENE BASED PLASMONIC BIOSENSOR

## 6.1 Introduction

In this chapter, PCF SPR biosensor is proposed where the plasmonic metal layer and analyte are placed outside the fiber structure which makes the sensor configuration simpler and the sensing process more straightforward. Considering the long-term stability of the plasmonic performance, copper (Cu) is used as the plasmonic material and graphene prevents Cu oxidation as well as to enhance the sensing performance. Numerical investigation of guiding properties and sensing performance are performed by using FEM.

## 6.2 Technical Review

SPR sensors require a metallic component carrying large amounts of free electrons. These free electrons provide the real part of a negative permittivity which is essential for plasmonic materials. Nevertheless, metals are chemically active and prone to oxidization. Oxidization tendency, material losses and corrosion are important factors that weaken the plasmonic property (West et al., 2010). Generally, gold (Au) and silver (Ag) are widely used as a plasmonic material for SPR sensors (Naik et al., 2013; West et al., 2010). Gold is chemically stable in many environments (aqueous environment, etc.) and shows large resonance peak shift. However, it has a broad resonance peak, which reduces the accuracy of analyte detection and it is lossy (Dash & Jha, 2014a). On the contrary, the utmost conductive material, silver, shows lower loss and sharper resonance peak compared to the other plasmonic materials. However, silver is not chemically stable and could be oxidized easily. Silver film with graphene layer coating could solve the oxidation problem (Dash & Jha, 2014a; Kravets et al., 2014). Due to fast oxidation and degradation

properties of silver, silver-graphene is not suitable for long-term plasmonic applications. Recently, Kravers et al. experimentally observed that silver-graphene coated plasmonic materials property deteriorates with time but, copper-graphene coated plasmonic property has shown long-term durability and its plasmonic performance is more stable, which is over a year (2014). Copper (Cu) is the second most conductive material after silver and it is much cheaper compared to both gold and silver. Cu material damping rate is the same as Au, and its interband transition is also close to Au (West et al., 2010). Cu oxidizes easily hence it has not received much attention compared to Au and Ag. However, Cu oxidation could be prevented with graphene layer coating as it is mechanically strong, chemically inert and having hexagonal lattice structure which is impermeable to gas molecules as small as helium and therefore inhibits the penetration of oxygen (Bunch et al., 2008; Schriver et al., 2013).

In this work, copper is utilized in PCF SPR sensor due to its long-term stable sensing performance; and graphene is used to prevent copper oxidation and enhance the sensor performance. Copper-graphene layer and analyte are placed outside the fiber structure to eliminate liquid infiltration and metal coating problem. Owing to the external sensing layer, the unknown analyte can be detected by simply flowing it through or dripped on the outer surface of Cu and graphene layers.

## 6.3    Structural Design and Numerical Analysis

Cross-sections of the PCF stacked preform and proposed sensor is shown in Fig. 7.1(a) and (b), respectively. Figure 7.1(c) shows the experimental setup of the proposed sensor where light from a supercontinuum source is coupled to the circular PCF structure. A circular sample holder is considered surrounding the PCF structure. Analyte sample IN and OUT is maintained through a pump. Finally the transmitted light is coupled to the optical spectrum analyzer (OSA) for the analysis. Considering the central air hole, proposed PCF consists of three hexagonal rings where the air-holes are similar.
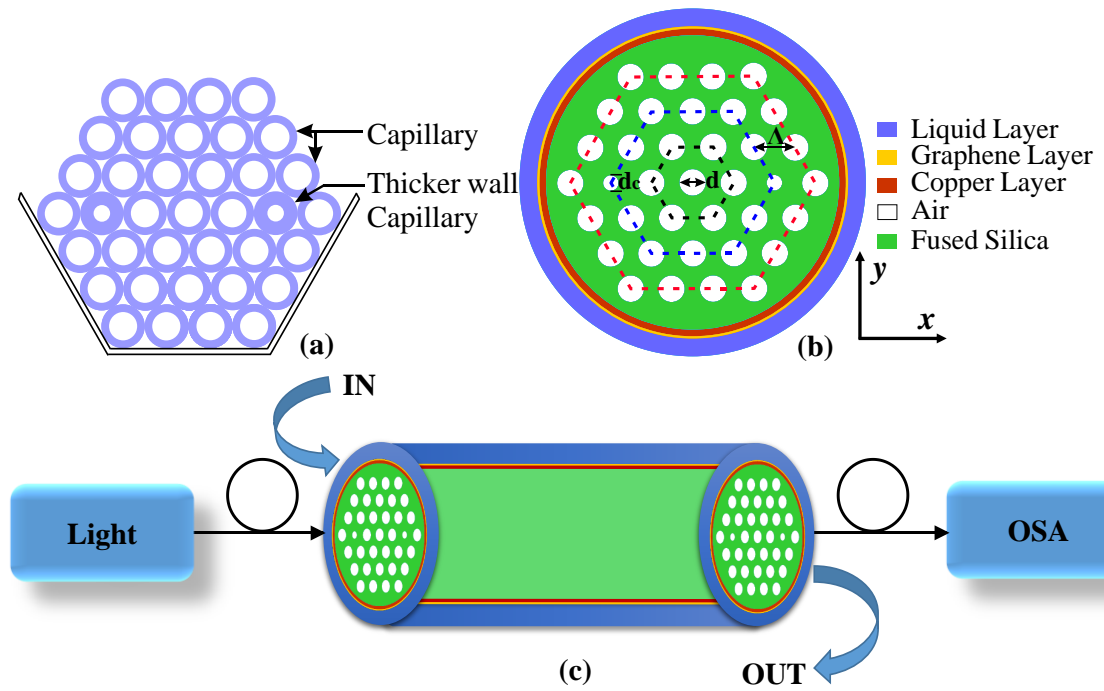
**Figure 6.1:** Cross-section of the proposed (a) PCF's stacked preform, (b) Sensor and (c) Schematic diagram of the experimental set-up.

In the second ring (blue dash line) along the horizontal row of the central hole, the two opposite sides of air-holes are scaled down to allow light propagating through their surrounding silica area. Scaled down holes are placed close to the plasmonic Cu surface to accelerate the excitation of the free electrons. The scaled down air-holes also facilitate coupling of phase-matched core-guided mode and surface plasmon polaritons (SPP) mode. In Figure 6.1(b), two adjacent air-holes are placed with uniform distance (pitch size) $\Lambda=2$ μm and air-holes diameter is, $d=0.50\Lambda$. The small air holes diameter is $d_c=0.30\Lambda$. If reduce the small air holes diameter than this, resulting the stronger light confinement will achieve through the core mode and the plasmon mode excitation will reduce resulting the sensing performance will be diminished. Also increase of diameter $d_c$ leads to the reduction of effective index of core thereby deteriorating the guidance along the cores and spread out over the cladding region. Owing two small air-holes, by introducing thicker wall capillaries, proposed PCF could be fabricated easily by using the standard stack-and-draw method. The refractive index (RI) of fused silica can be

calculated from Eq. 2.26. Outside the fiber structure, Cu layer of thickness $t$=30 nm is used. Cu layer could be deposited using electron-beam evaporation method (Kravets et al., 2014). The complex RI property of Cu has been adopted from (Rakic, Djurišic, Elazar, & Majewski, 1998). On top of the Cu layer, graphene layer thickness has been calculated by $t_g$=0.34 nm $\times$ $L$ (L=1, 2, 3,...), where $L$ is the number of layers. By using transfer printing process and CVD process, monolayer or multilayer graphene can be directly grown or deposited on the Cu surface (Kravets et al., 2014; Salihoglu et al., 2012). The complex RI of graphene is determined from the equation: $n_g$=$3$+$iC_l\lambda/3$, where $\lambda$ is the vacuum wavelength in µm and constant $C_l \approx 5.446$ µm$^{-1}$ (Dash & Jha, 2014a). The fiber structure is surrounded by the analyte to be detected. The guiding properties and the sensing performances are investigated using FEM based commercial software, COMSOL. PML is used as a radiation absorber which absorbs the scattered or radiated light towards the surface.

## 6.4    Results and Performance Analysis

PCF SPR sensors performance depends on the evanescent field which is due to light propagation through the core. Stronger modal field is desired to ensure interaction with the sensing layer (analyte) for better sensing performance. The modal analysis of the proposed sensor has been carried out in $xy$-plane while light is propagating in $z$-direction. $y$-component mode is used for the following work due to the larger evanescent field, stronger interaction with the analytes and higher loss depth as compared to the $x$-component mode. Resonance occurs when the real effective index of core-guided mode is matched with the real ($n_{eff}$) value of SPP mode. At resonance, core-guided mode is coupled to the plasmonic mode, resulting in a sharp loss peak which is called the phase matching point. The phase matching condition of the proposed sensor is shown in Figure 6.2.
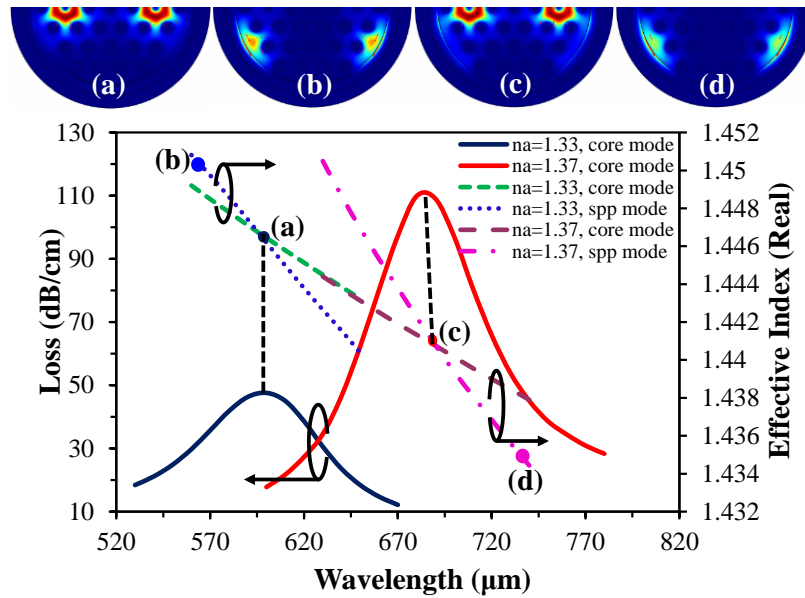
**Figure 6.2:** Dispersion relations of core guided mode (green, maroon), SPP mode (blue, magenta) and loss spectra (black, red); inset (a, c): field distribution of the core-guided mode, inset (b, d): field distribution of the plasmonic mode for analyte RI $n_a$=1.33 and 1.37 respectively.

At analyte RI ($n_a$) 1.33, phase matching is found to be at 600 nm, while at RI 1.37, it shifts towards the longer wavelength and appears at 680 nm wavelength. In Figure 6.2, core-guided fundamental mode field distribution is shown in inset (a, c), where the core-mode and plasmonic mode are coupled together. Inset (b, d) of Figure 6.2 shows the plasmonic mode field distribution. The phase matching coupling is verified by the coincidence of the resonant peak and the intersection between the dispersion relations of the core-guided mode and SPP mode. The confinement loss is obtained from Eq. 4.3. Figure 6.2 also indicates phase matching wavelength changes with analyte RI. The small change of analyte RI strongly affects Re($n_{eff}$) of the vicinity dielectric-metal surface plasmonic mode and changes the phase matching wavelength. The effect of analyte RI on the loss spectrum is shown in Figure 6.3.
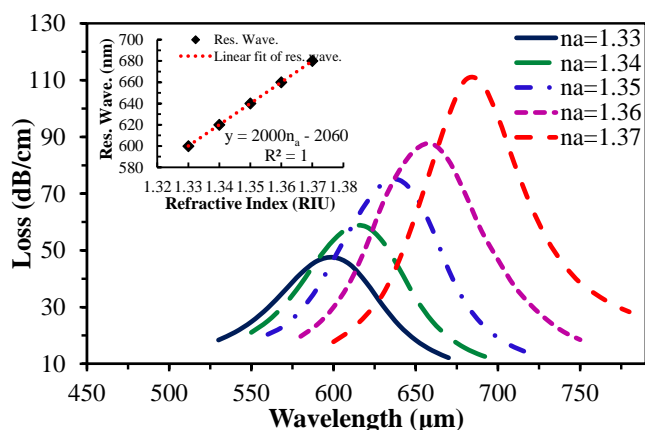
**Figure 6.3:** Fundamental loss spectrum with the variation of analyte RI from 1.33 to 1.37; inset shows the linear fit of resonant wavelength with respect to analyte RI changes ($d_c = 0.30\Lambda$, $d = 0.50\Lambda$, $t = 30$ nm and $t_g = 0.34$ nm (monolayer)).

In Figure 6.3, with analyte RI 1.33, resonance peak appears at 600 nm wavelength with the loss depth of 48 dB/cm. Due to the change of analyte RI from 1.33 to 1.37 (with iteration of 0.01), loss peak shifts towards longer wavelengths and loss depth increases simultaneously. Maximum loss depth of 120 dB/cm is found at resonant wavelength 680 nm when the analyte RI is 1.37, which indicates the maximum energy transferred from the core-guided mode to the SPP mode, resulting in a sharp resonance peak at RI 1.37. Inset of Figure 6.3 shows the linear resonant wavelength shift where linear regression $R^2$ is 1. Using the wavelength interrogation method, proposed sensor shows sensitivity and sensor resolution of 2000 nm/RIU and $5 \times 10^{-5}$ RIU, respectively (by assuming the wavelength resolution is 0.1 nm), which is comparable with the results reported in (Dash & Jha, 2014b). Alternatively, amplitude or phase interrogation sensing scheme could be used, where only measurement at single wavelength is needed for analyte detection. It is simple and cost effective since it does not required spectral manipulation (Otupiri et al., 2014). The amplitude sensitivity is shown in Figure 6.4 by varying the analyte RI. The amplitude sensitivity of the proposed sensor increases with higher analyte RI, as shown in Figure 6.4.
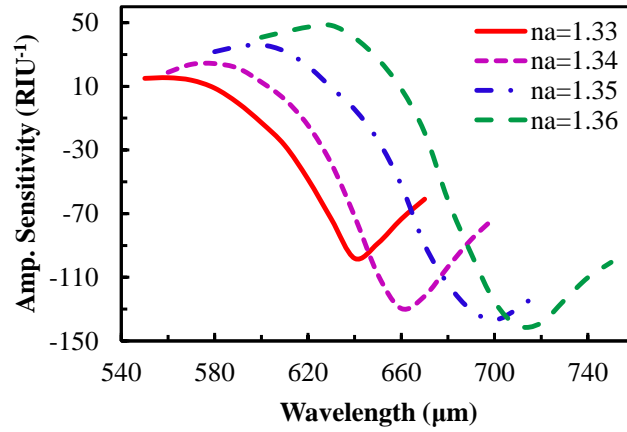
**Figure 6.4:** Amplitude sensitivity spectrum with varying the analyte RI 1.33-1.36.

The interaction between evanescent field and plasmon mode increases with the increase of analyte RI. Maximum sensitivity of 140 $RIU^{-1}$ is achieved with analyte RI 1.36, which gives the sensor resolution of $7.1\times10^{-5}$ RIU, considering minimum 1% transmitted intensity can be detected precisely. Additionally, amplitude sensitivities 98, 130 and 137 $RIU^{-1}$ are achieved for the analyte RI of 1.33, 1.34 and 1.35, respectively. Table 6.1 shows the performance comparisons of the reported sensors.

**Table 6.1:** Performance comparison of simulated PCF SPR sensors.

| Characteristics | RI Range | Interrogation | Sensitivity | Resolution (RIU) | Ref. |
|---|---|---|---|---|---|
| Multi-hole fiber based SPR sensor | 1.33-1.35 | Wavelength | 2,000 nm/RIU | $5\times10^{-5}$ | (Gao et al., 2014) |
| | | Amplitude | 370 $RIU^{-1}$ | $2.7\times10^{-5}$ | |
| Selectively ITO coated polymer PCF | 1.33-1.35 | Wavelength | 2,000 nm/RIU | $5\times10^{-5}$ | (Dash & Jha, 2014b) |
| Selectively filled silver nanowires | 1.330-1.335 | Wavelength | N/A | $4.55\times10^{-5}$ | (Mishra et al., 2015) |
| | | Amplitude | 203 $RIU^{-1}$ | $4.9\times10^{-5}$ | |
| Copper-graphene based SPR sensor | 1.33-1.37 | Wavelength | 2,000 nm/RIU | $5\times10^{-5}$ | (This work) |
| | | Amplitude | 140 $RIU^{-1}$ | $7.1\times10^{-5}$ | |

Besides the effects of analyte RI, copper layer thickness also has significant effects on the sensing performance, as shown in Figure 6.5. Figure 6.5(a) shows the loss value increases with the decrease of Cu thickness and the resonant wavelength is red shifted.
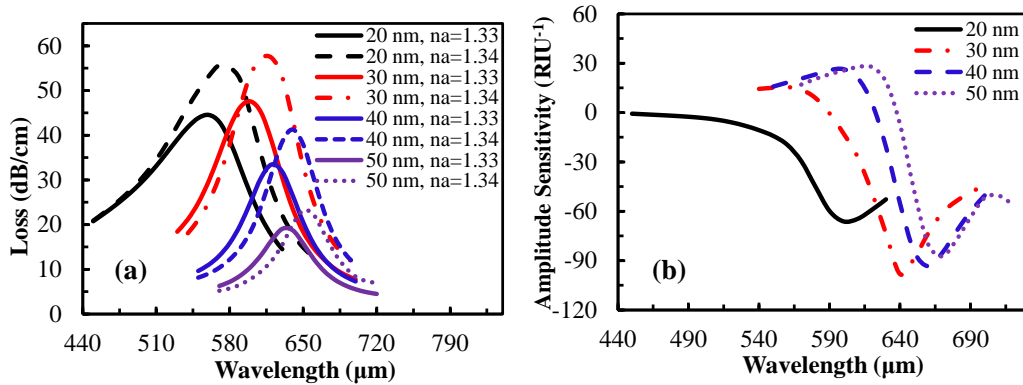


**Figure 6.5:** (a) Loss spectrum and (b) amplitude sensitivity effects with varying Cu thickness 30 to 50 nm; ($d_c = 0.30\Lambda$, $d = 0.50\Lambda$, and $t_g = 0.34$ nm).

However, after surpassing a certain thickness level, as Cu thickness decreases, loss value decreases and exhibits wider resonance curve. At the analyte RI 1.34, maximum loss value of 48 dB/cm is achieved for Cu thickness of 30 nm at 600 nm wavelength and decreases significantly to 19 dB/cm and resonant wavelength shifts to 630 nm when $t$=50 nm. By using wavelength interrogation, the sensitivities are 2000, 2000, 1800 and 1500 nm/RIU when the Cu thicknesses are 20, 30, 40 and 50 nm, respectively. Thicker Cu layer introduces more damping which causes the evanescent field penetration towards the surface and the presence of surface plasmons on the sensing layer weakened significantly. The same scenario also observed for amplitude sensitivity, shown in Figure 6.5(b). The maximum amplitude sensitivity 98 RIU$^{-1}$ is achieved at 640 nm wavelength when the Cu thickness is 30 nm. When the Cu thickness is increased to 50 nm, amplitude sensitivity decreases gradually to 87 RIU$^{-1}$ and resonant wavelength shifts towards the longer wavelength 670 nm. In contrast, at $t$=20 nm, sensor shows the amplitude sensitivity of 66 RIU$^{-1}$ with broaden amplitude peak. The maximum amplitude sensitivity leads to sensor resolution of $1\times10^{-4}$ RIU.

Additionally, graphene has significant effects on sensing performance. Due to its large surface to volume ratio, it interacts with the analytes on the surface resulting in increased sensing performance. The effects of the number of graphene layers on the sensing performance are shown in Figure 6.6.
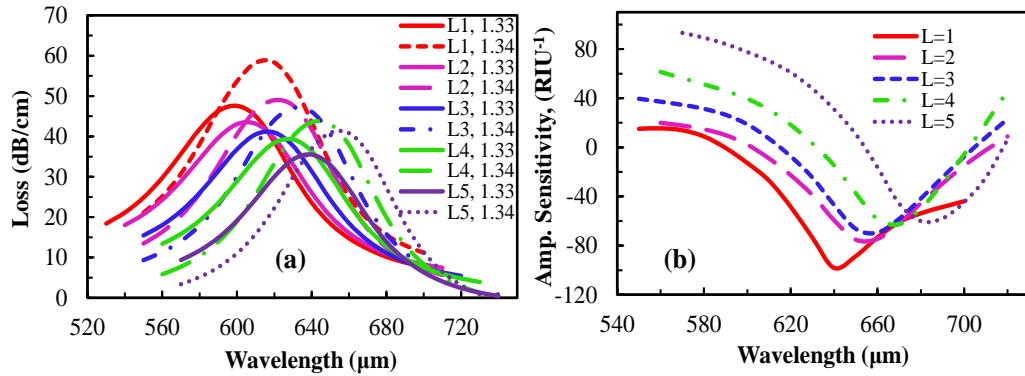


**Figure 6.6:** (a) Loss spectrum and (b) amplitude sensitivity effects with varying the graphene layers from L= 1 to 5.

In Figure 6.6(a), loss depth decreases gradually with the increase of graphene layers and analyte RI. At analyte RI 1.33, the sensor shows red shift of resonant wavelength and the loss value decreases gradually from 48 to 35 dB/cm when thickness of graphene is increased from single layer ($t_g$=0.34 nm×1) to 5 layers ($t_g$=0.34 nm×5), respectively. Moreover, amplitude sensitivity also decreases from 98 to 60 RIU$^{-1}$ with the increase of graphene layer from 1 to 5, respectively. As the graphene is mechanically strong and chemically inert, single or double layer could be able to prevent the oxidation.

Typically, silver has been widely used as a plasmonic material due to its low material losses and sharper resonance peak. As a comparison, amplitude sensitivity for Cu-graphene and Ag-graphene combinations of the proposed sensor is shown in Figure 6.7. Ag-graphene and Cu-graphene sensors achieved amplitude sensitivities of 117 and 98 RIU$^{-1}$, respectively. Although Ag-graphene shows slightly higher amplitude sensitivity as compared to Cu-graphene, yet, Cu-graphene combination has even sharper

resonance peak with more stable plasmonic performance in the long term (Kravets et al., 2014).
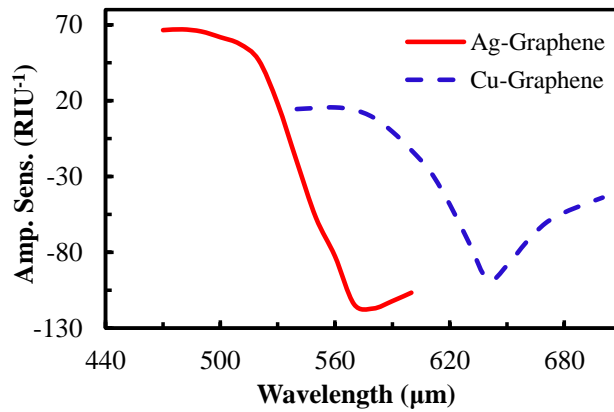


**Figure 6.7:** Comparison of amplitude sensitivity with graphene coated Cu and Ag layer, setting $n_a$= 1.33, $d_c$ = 0.30Λ, $d$ = 0.50Λ, $t$ = $t_{Ag}$= 30 nm and $t_g$= 0.34 nm.

## 6.5    Summary

In summary, a simple copper-graphene based PCF SPR sensor is proposed. Guiding properties and sensing performance of the proposed sensor are numerically investigated by FEM. Proposed sensor shows the maximum wavelength interrogation sensitivity of 2000 nm/RIU and achieve sensor resolution of $5×10^{-5}$ RIU. Furthermore, it shows the amplitude sensitivity of 140 RIU$^{-1}$ with the sensor resolution $7.1×10^{-5}$ RIU. The proposed sensor structure is simpler among the reported PCF SPR sensors which could be realized using the standard stack-and-draw fabrication method and sputtering, CVD deposition method.

# CHAPTER 7: CONCLUSION AND FUTURE WORKS

## 7.1 Conclusion

In this study, four different PCF based SPR sensors are developed. Guiding properties are numerically investigated by commercial COMSOL software. The sensors performance is observed based on wavelength and amplitude interrogation methods. A short summary of proposed PCF SPR sensors are given below:

**Silver-graphene coated PCF SPR sensor:** Considering the selective multiple metallic channel problem, a single metallic channel (silver with graphene coated) based PCF SPR sensor is proposed which is comparatively simpler in the fabrication point of view. Furthermore, only two liquid-filled cores are considered which are placed near to the metallic channel for easy excitation of free electrons to produce SPW. Silver is used as a plasmonic material with a thin graphene layer to prevent oxidation. According to the wavelength interrogation sensitivity, proposed sensor shows the RI sensitivity of 3000 nm/RIU with sensor resolution of $3.33 \times 10^{-5}$ RIU, whereas the average RI sensitivity is 2390 nm/RIU in the sensing range of 1.46 to 1.49. In addition, it shows the amplitude sensitivity as high as 418 $RIU^{-1}$ which gives the sensor resolution of $2.4 \times 10^{-5}$ RIU. However, metal layer coating inside the air-hole surface is quite challenging; as well as observing the internal sensing is difficult.

**Flat fiber based SPR sensor:** Flat fiber based SPR sensor is proposed for the first time in this study. Utilizing the advantage of flat surface, metal layer can be incorporated easily as well as it turns the simple sensing process. Due to manage the metallic layer close to the cores which helps to easy excitation of free electrons. Using the proposed sensor, average wavelength interrogation sensitivity of 9,600 nm/RIU (Refractive Index Unit) and highest sensitivity of 23,000 nm/RIU are obtained in the sensing range of 1.46-1.485 and 1.47-1.475, respectively. Moreover, refractive index resolution of $4.35 \times 10^{-6}$ is

obtained. Additionally, proposed sensor shown the maximum amplitude interrogation sensitivity of 820 RIU$^{-1}$, with the sensor resolution $1.22\times10^{-5}$ RIU. The proposed flat fiber sensor provided the highest wavelength interrogation sensitivity among all the reported fiber based SPR sensors. The only small challenging part of this sensor is to selectively infiltrate the liquid.

**PCF SPR biosensor with external sensing approach:** A simple PCF SPR sensor is proposed where the metallic layer and sensing layer are placed outside the fiber structure. Due to outside sensing layer, sensing mechanism will be simple. By using wavelength and amplitude interrogation methods, the proposed sensor could provide maximum sensitivities up to 4000 nm/RIU and 320 RIU$^{-1}$ respectively. The resolutions of the sensor are $2.5\times10^{-5}$ and $3.125\times10^{-5}$ RIU for wavelength and amplitude interrogation methods. In this sensor, the irregular air-holes in the fiber structure can be easily and practically fabricated by introducing thicker wall capillary.

**Copper-graphene based plasmonic biosensor:** In this work, for the first time, copper is utilized as the plasmonic material for PCF SPR sensor. Graphene layer is used to diminish the oxidation problem. It shows the linear sensing response over the sensing range. It shows average wavelength interrogation sensitivity of 2000 nm/RIU over the analyte refractive indices range from 1.33 to 1.37, which leads the sensor resolution of $5\times10^{-5}$ RIU.

The proposed sensors in this study, particularly those with external sensing approaches, breakthrough the PCF SPR sensor technology, that would be very useful for implementing the fiber SPR sensor practically.

## 7.2    Future Works

PCF SPR sensing is a promising and competitive sensing technology. However, at the device development front, PCF SPR sensors are still in an early stage. Most of the work

reported in the literature involves proof of concept demonstrations, theoretical and computational models. The application of established theoretical models to sensor implementation is limited. Although some experimental devices reported in the literature, their applications are found in limited research domains. Therefore, the performances of the modelled sensors are still in question. Potential future work should focus on (i) proof of concept demonstration to real PCF SPR sensor development, (ii) detection of analytes from more chemical and biological samples. One possible development direction for the PCF SPR sensors is portable and rapid lab-on-a-chip assays for point-of-care diagnostics.

Future works that can be carried out for further improving the findings in this study are as following:

(i) Fabricating the proposed PCFs and combine the plasmonic metal layer outside the fiber structure to establish the SPR phenomena.

(ii) Observe the sensing performance practically and compare the experimental results and simulation results.

The PCF SPR sensor shows a promising ability in the detection of chemical and biological analytes. The performance of the PCF SPR biosensor technology will continue to evolve with the advances in fabrication technology and the development in metal nanoparticles. We envision that in future the PCF SPR sensor will become one of the most popular optical biosensors which will be used in many important sectors such as medical diagnostics, environmental monitoring, and food safety and security.

# REFERENCES

Adikan, F. R. M., Sandoghchi, S. R., Yi, C. W., Simpson, R. E., Mahdi, M. A., Webb, A. S., Holmes, C. (2012). Direct UV written optical waveguides in flexible glass flat fiber chips. *Selected Topics in Quantum Electronics, IEEE Journal of, 18*(5), 1534-1539.

Ahmmed, R., Ahmed, R., & Razzak, S. A. (2013). *Design of large negative dispersion and modal analysis for hexagonal, square, FCC and BCC photonic crystal fibers.* Paper presented at the Informatics, Electronics & Vision (ICIEV), 2013 International Conference on.

Akimoto, T., Sasaki, S., Ikebukuro, K., & Karube, I. (1999). Refractive-index and thickness sensitivity in surface plasmon resonance spectroscopy. *Applied optics, 38*(19), 4058-4064.

Akowuah, E. K., Gorman, T., Ademgil, H., Haxha, S., Robinson, G. K., & Oliver, J. V. (2012). Numerical analysis of a photonic crystal fiber for biosensing applications. *Quantum Electronics, IEEE Journal of, 48*(11), 1403-1410.

Amouzad Mahdiraji, G. (2015). *Low-Crosstalk Semi-Trench-Assisted Multicore Flat Fiber.* Paper presented at the Optical Fiber Communication Conference.

Amouzad Mahdiraji, G., Chow, D. M., Sandoghchi, S., Amirkhan, F., Dermosesian, E., Yeo, K. S., . . . Yu Gang, S. (2014). Challenges and solutions in fabrication of silica-based photonic crystal fibers: An experimental study. *Fiber and Integrated Optics, 33*(1-2), 85-104.

Aoni, R. A., Ahmed, R., & Razzak, S. (2013). *Design and Simulation of Duel-Concentric-Core Photonic Crystal Fiber for Dispersion Compensation.* Paper presented at the CIOMP-OSA Summer Session on Optical Engineering, Design and Manufacturing.

Ashwell, G., & Roberts, M. (1996). Highly selective surface plasmon resonance sensor for NO 2. *Electronics Letters, 32*(22), 2089-2091.

Berger, C. E., & Greve, J. (2000). Differential SPR immunosensing. *Sensors and Actuators B: Chemical, 63*(1), 103-108.

Biswas, T., Chattopadhyay, R., & Bhadra, S. K. (2014). Plasmonic hollow-core photonic band gap fiber for efficient sensing of biofluids. *Journal of Optics, 16*(4), 045001.

Botten, L. C., McPhedran, R. C., de Sterke, C. M., Nicorovici, N. A., Asatryan, A. A., Smith, G. H., Kuhlmey, B. T. (2005). From multipole methods to photonic crystal device modeling. *Electromagnetic theory and applications for photonic crystals (optical engineering)*, 47-122.

Bunch, J. S., Verbridge, S. S., Alden, J. S., van der Zande, A. M., Parpia, J. M., Craighead, H. G., & McEuen, P. L. (2008). Impermeable atomic membranes from graphene sheets. *Nano letters, 8*(8), 2458-2462.

Cahill, C. P., Johnston, K. S., & Yee, S. S. (1997). A surface plasmon resonance sensor probe based on retro-reflection. *Sensors and Actuators B: Chemical, 45*(2), 161-166.

Cheng, D. K. (1989). *Field and wave electromagnetics* (Vol. 2): Addison-wesley New York.

Cheng, Y.-C., Su, W.-K., & Liou, J.-H. (2000). Application of a liquid sensor based on surface plasma wave excitation to distinguish methyl alcohol from ethyl alcohol. *Optical Engineering, 39*(1), 311-314.

Choi, S. H., Kim, Y. L., & Byun, K. M. (2011). Graphene-on-silver substrates for sensitive surface plasmon resonance imaging biosensors. *Optics express, 19*(2), 458-466.

Cinteza, L. O., Ohulchanskyy, T. Y., Sahoo, Y., Bergey, E. J., Pandey, R. K., & Prasad, P. N. (2006). Diacyllipid micelle-based nanocarrier for magnetically guided delivery of drugs in photodynamic therapy. *Molecular pharmaceutics, 3*(4), 415-423.

Cooper, M. A. (2002). Optical biosensors in drug discovery. *Nature Reviews Drug Discovery, 1*(7), 515-528.

Daghestani, H. N., & Day, B. W. (2010). Theory and applications of surface plasmon resonance, resonant mirror, resonant waveguide grating, and dual polarization interferometry biosensors. *Sensors, 10*(11), 9630-9646.

Dash, J. N., & Jha, R. (2014a). Graphene-based birefringent photonic crystal fiber sensor using surface plasmon resonance. *Photonics Technology Letters, IEEE, 26*(11), 1092-1095.

Dash, J. N., & Jha, R. (2014b). SPR Biosensor Based on Polymer PCF Coated With Conducting Metal Oxide. *IEEE Photonics Technology Letters, 26*(6), 595-598. doi:10.1109/lpt.2014.2301153

Dash, J. N., & Jha, R. (2015a). On the Performance of Graphene-Based D-Shaped Photonic Crystal Fibre Biosensor Using Surface Plasmon Resonance. *Plasmonics*, 1-9.

Dash, J. N., & Jha, R. (2015b). On the Performance of Graphene-Based D-Shaped Photonic Crystal Fibre Biosensor Using Surface Plasmon Resonance. *Plasmonics, 10*, 1123–1131.

DeVore, J. R. (1951). Refractive indices of rutile and sphalerite. *JOSA, 41*(6), 416-417.

Dular, P., Meunier, G., Piriou, F., Ould Agha, Y., Zolla, F., Nicolet, A., & Guenneau, S. (2008). On the use of PML for the computation of leaky modes: an application to microstructured optical fibres. *COMPEL-The international journal for computation and mathematics in electrical and electronic engineering, 27*(1), 95-109.

Egorova, O., Semjonov, S., Senatorov, A., Salganskii, M., Koklyushkin, A., Nazarov, V., Dianov, E. (2014). Multicore fiber with rectangular cross-section. *Optics letters, 39*(7), 2168-2170.

Emmerich, G. Surface Plasmon Resonance: Technology Overview and Practical Applications.

Fang, Y. (2006). Label-free cell-based assays with optical biosensors in drug discovery. *Assay and drug development technologies, 4*(5), 583-595.

Fu, X., Lu, Y., Huang, X., & Yao, J. (2011). Surface plasmon resonance sensor based on photonic crystal fiber filled with silver nanowires. *Opt. Appl, 41*(4), 941-951.

Gallagher, D. F., & Felici, T. P. (2003). *Eigenmode expansion methods for simulation of optical propagation in photonics: pros and cons*. Paper presented at the Integrated Optoelectronics Devices.

Gao, D., Guan, C., Wen, Y., Zhong, X., & Yuan, L. (2014). Multi-hole fiber based surface plasmon resonance sensor operated at near-infrared wavelengths. *Optics Communications, 313*, 94-98.

Gauvreau, B., Hassani, A., Fassi Fehri, M., Kabashin, A., & Skorobogatiy, M. A. (2007). Photonic bandgap fiber-based surface plasmon resonance sensors. *Optics express, 15*(18), 11413-11426.

Guo, J., Liu, Y.-g., Wang, Z., Han, T., Huang, W., & Luo, M. (2014). Tunable fiber polarizing filter based on a single-hole-infiltrated polarization maintaining photonic crystal fiber. *Optics express, 22*(7), 7607-7616.

Gupta, B., & Verma, R. (2009). Surface plasmon resonance-based fiber optic sensors: principle, probe designs, and some applications. *Journal of Sensors, 2009*.

Hassani, A., Gauvreau, B., Fehri, M. F., Kabashin, A., & Skorobogatiy, M. (2008). Photonic crystal fiber and waveguide-based surface plasmon resonance sensors for application in the visible and near-IR. *Electromagnetics, 28*(3), 198-213.

Hassani, A., & Skorobogatiy, M. (2006). Design of the microstructured optical fiber-based surface plasmon resonance sensors with enhanced microfluidics. *Optics express, 14*(24), 11616-11621.

Hassani, A., & Skorobogatiy, M. (2009). Photonic crystal fiber-based plasmonic sensors for the detection of biolayer thickness. *JOSA B, 26*(8), 1550-1557.

Holmes, C., Adikan, F. R., Webb, A. S., Gates, J. C., Gawith, C. B., Sahu, J. K., Payne, D. N. (2008). *Evanescent field sensing in novel flat fiber*. Paper presented at the Conference on Lasers and Electro-Optics.

Homola, J. (2003). Present and future of surface plasmon resonance biosensors. *Analytical and bioanalytical chemistry, 377*(3), 528-539.

Homola, J. (2006). *Surface plasmon resonance based sensors* (Vol. 4): Springer Science & Business Media.

Homola, J. (2008). Surface plasmon resonance sensors for detection of chemical and biological species. *Chemical reviews, 108*(2), 462-493.

Homola, J., Yee, S. S., & Gauglitz, G. (1999). Surface plasmon resonance sensors: review. *Sensors and Actuators B: Chemical, 54*(1), 3-15.

Ismach, A., Druzgalski, C., Penwell, S., Schwartzberg, A., Zheng, M., Javey, A., Zhang, Y. (2010). Direct chemical vapor deposition of graphene on dielectric surfaces. *Nano letters, 10*(5), 1542-1548.

Jie, Z., Dakai, L., & Zhenwu, Z. (2007). Reflective optical fiber surface plasma wave resonance sensor. *Acta Optica Sinica, 27*(3), 404.

Johnson, S., & Joannopoulos, J. (2001). Block-iterative frequency-domain methods for Maxwell's equations in a planewave basis. *Optics express, 8*(3), 173-190.

Johnston, K. S., Karlsen, S. R., Jung, C. C., & Yee, S. S. (1995). New analytical technique for characterization of thin films using surface plasmon resonance. *Materials chemistry and physics, 42*(4), 242-246.

Jorgenson, R., & Yee, S. (1993). A fiber-optic chemical sensor based on surface plasmon resonance. *Sensors and Actuators B: Chemical, 12*(3), 213-220.

Kajenski, P. J. (1997). Tunable optical filter using long-range surface plasmons. *Optical Engineering, 36*(5), 1537-1541.

Kanso, M., Cuenot, S., & Louarn, G. (2007). Roughness effect on the SPR measurements for an optical fibre configuration: experimental and numerical approaches. *Journal of Optics A: Pure and Applied Optics, 9*(7), 586.

Khan, I. (2012). *Optical fiber based microwaves sensor using surface plasmon resonance.* Paper presented at the Informatics, Electronics & Vision (ICIEV), 2012 International Conference on.

Kim, J. A., Hwang, T., Dugasani, S. R., Amin, R., Kulkarni, A., Park, S. H., & Kim, T. (2013). Graphene based fiber optic surface plasmon resonance for bio-chemical sensor applications. *Sensors and Actuators B: Chemical, 187*, 426-433.

Kiraly, B., Iski, E. V., Mannix, A. J., Fisher, B. L., Hersam, M. C., & Guisinger, N. P. (2013). Solid-source growth and atomic-scale characterization of graphene on Ag (111). *Nature communications, 4*.

Knoll, W. (1998). Interfaces and thin films as seen by bound electromagnetic waves. *Annual Review of Physical Chemistry, 49*(1), 569-638.

Koshiba, M. (1992). Optical waveguide theory by the finite element method.

Koshiba, M., & Saitoh, K. (2001). Numerical verification of degeneracy in hexagonal photonic crystal fibers. *Ieee Photonics Technology Letters, 13*(12), 1313-1315.

Kotynski, R., Antkowiak, M., Berghmans, F., Thienpont, H., & Panajotov, K. (2005). Photonic crystal fibers with material anisotropy. *Optical and quantum electronics, 37*(1-3), 253-264.

Kravets, V., Jalil, R., Kim, Y.-J., Ansell, D., Aznakayeva, D., Thackray, B., . . . Radko, I. (2014). Graphene-protected copper and silver plasmonics. *Scientific reports, 4*.

KretschmannE, R. (1968). Radiativedecayofnon radiative surface plasmons excited by light. *Z Naturforsch, 23*, 2135－2136

Kuhlmey, B. T., Eggleton, B. J., & Wu, D. K. (2009). Fluid-filled solid-core photonic bandgap fibers. *Journal of Lightwave Technology, 27*(11), 1617-1630.

Liedberg, B., Nylander, C., & Lunström, I. (1983). Surface plasmon resonance for gas detection and biosensing. *Sensors and actuators, 4*, 299-304.

Lu, Y., Hao, C.-J., Wu, B.-Q., Huang, X.-H., Wen, W.-Q., Fu, X.-Y., & Yao, J.-Q. (2012). Grapefruit fiber filled with silver nanowires surface plasmon resonance sensor in aqueous environments. *Sensors, 12*(9), 12016-12025.

Lu, Y., Hao, C.-J., Wu, B.-Q., Musideke, M., Duan, L.-C., Wen, W.-Q., & Yao, J.-Q. (2013). Surface plasmon resonance sensor based on polymer photonic crystal fibers with metal nanolayers. *Sensors, 13*(1), 956-965.

Lu, Y., Yang, X., Wang, M., & Yao, J. (2015). Surface plasmon resonance sensor based on hollow-core PCFs filled with silver nanowires. *Electronics Letters, 51*(21), 1675-1677.

Luan, N., Wang, R., Lv, W., & Yao, J. (2015). Surface plasmon resonance sensor based on D-shaped microstructured optical fiber with hollow core. *Optics express, 23*(7), 8576-8582.

Maharana, P. K., & Jha, R. (2012). Chalcogenide prism and graphene multilayer based surface plasmon resonance affinity biosensor for high performance. *Sensors and Actuators B: Chemical, 169*, 161-166.

Mahdiraji, G. A., Amirkhan, F., Chow, D. M., Kakaie, Z., Yong, P. S., Dambul, K. D., & Adikan, F. R. M. (2014). Multicore Flat Fiber: A New Fabrication Technique. *Photonics Technology Letters, IEEE, 26*(19), 1972-1974.

Malinský, P., Slepička, P., Hnatowicz, V., & Švorčík, V. (2012). Early stages of growth of gold layers sputter deposited on glass and silicon substrates. *Nanoscale research letters, 7*(1), 1-7.

Mishra, A. K., Mishra, S. K., & Gupta, B. D. (2015). SPR based fiber optic sensor for refractive index sensing with enhanced detection accuracy and figure of merit in visible region. *Optics Communications, 344*, 86-91.

Myszka, D. G. (1999). Improving biosensor analysis. *Journal of Molecular Recognition, 12*(5), 279-284.

Naik, G. V., Shalaev, V. M., & Boltasseva, A. (2013). Alternative plasmonic materials: beyond gold and silver. *Advanced Materials, 25*(24), 3264-3294.

Niggemann, M., Katerkamp, A., Pellmann, M., Bolsmann, P., Reinbold, J., & Cammann, K. (1996). Remote sensing of tetrachloroethene with a micro-fibre optical gas sensor based on surface plasmon resonance spectroscopy. *Sensors and Actuators B: Chemical, 34*(1), 328-333.

Ortega-Mendoza, J. G., Padilla-Vivanco, A., Toxqui-Quitl, C., Zaca-Morán, P., Villegas-Hernández, D., & Chávez, F. (2014). Optical Fiber Sensor Based on Localized Surface Plasmon Resonance Using Silver Nanoparticles Photodeposited on the Optical Fiber End. *Sensors, 14*(10), 18701-18710.

Otto, A. (1968). Excitation of nonradiative surface plasma waves in silver by the method of frustrated total reflection. *Zeitschrift für Physik, 216*(4), 398-410.

Otupiri, R., Akowuah, E., & Haxha, S. (2015). Multi-channel SPR biosensor based on PCF for multi-analyte sensing applications. *Optics express, 23*(12), 15716-15727.

Otupiri, R., Akowuah, E., Haxha, S., Ademgil, H., AbdelMalek, F., & Aggoun, A. (2014). A novel birefrigent photonic crystal fiber surface plasmon resonance biosensor. *Photonics Journal, IEEE, 6*(4), 1-11.

Palik, E. D. (1998). *Handbook of optical constants of solids* (Vol. 3): Academic press.

Pearce, G., Hedley, T., & Bird, D. (2005). Adaptive curvilinear coordinates in a plane-wave solution of Maxwell's equations in photonic crystals. *Physical Review B, 71*(19), 195108.

Poletti, F. (2007). *Direct and inverse design of microstructured optical fibres.* University of Southampton.

Qin, W., Li, S., Yao, Y., Xin, X., & Xue, J. (2014). Analyte-filled core self-calibration microstructured optical fiber based plasmonic sensor for detecting high refractive index aqueous analyte. *Optics and Lasers in Engineering, 58*, 1-8.

Rakic, A. D., Djurišic, A. B., Elazar, J. M., & Majewski, M. L. (1998). Optical properties of metallic films for vertical-cavity optoelectronic devices. *Applied optics, 37*(22), 5271-5283.

Rhodes, C., Cerruti, M., Efremenko, A., Losego, M., Aspnes, D., Maria, J.-P., & Franzen, S. (2008). Dependence of plasmon polaritons on the thickness of indium tin oxide thin films. *Journal of Applied Physics, 103*(9), 093108.

Ritchie, R. (1957). Plasma losses by fast electrons in thin films. *Physical Review, 106*(5), 874.

Salihoglu, O., Balci, S., & Kocabas, C. (2012). Plasmon-polaritons on graphene-metal surface and their use in biosensors. *Applied Physics Letters, 100*(21), 213110.

Sazio, P. J., Amezcua-Correa, A., Finlayson, C. E., Hayes, J. R., Scheidemantel, T. J., Baril, N. F., Margine, E. R. (2006). Microstructured optical fibers as high-pressure microfluidic reactors. *science, 311*(5767), 1583-1586.

Schildkraut, J. S. (1988). Long-range surface plasmon electrooptic modulator. *Applied optics, 27*(21), 4587-4590.

Schriver, M., Regan, W., Gannett, W. J., Zaniewski, A. M., Crommie, M. F., & Zettl, A. (2013). Graphene as a long-term metal oxidation barrier: worse than nothing. *ACS nano, 7*(7), 5763-5768.

Sharma, A. K., Jha, R., & Gupta, B. (2007). Fiber-optic sensors based on surface plasmon resonance: a comprehensive review. *Sensors Journal, IEEE, 7*(8), 1118-1129.

Shi, F., Peng, L., Zhou, G., Cang, X., Hou, Z., & Xia, C. (2015). An Elliptical Core D-Shaped Photonic Crystal Fiber-Based Plasmonic Sensor at Upper Detection Limit. *Plasmonics*, 1-6.

Shuai, B., Xia, L., & Liu, D. (2012). Coexistence of positive and negative refractive index sensitivity in the liquid-core photonic crystal fiber based plasmonic sensor. *Optics express, 20*(23), 25858-25866.

Shuai, B., Xia, L., Zhang, Y., & Liu, D. (2012). A multi-core holey fiber based plasmonic sensor with large detection range and high linearity. *Optics express, 20*(6), 5974-5986.

Sincerbox, G. T., & Gordon, J. C. (1981). Small fast large-aperture light modulator using attenuated total reflection. *Applied optics, 20*(8), 1491-1496.

Slavík, R., Homola, J., & Čtyroký, J. (1999). Single-mode optical fiber surface plasmon resonance sensor. *Sensors and Actuators B: Chemical, 54*(1), 74-79.

Snyder, A. W., & Love, J. (2012). *Optical waveguide theory*: Springer Science & Business Media.

Stemmler, I., Brecht, A., & Gauglitz, G. (1999). Compact surface plasmon resonance-transducers with spectral readout for biosensing applications. *Sensors and Actuators B: Chemical, 54*(1), 98-105.

Su, Y.-T., Chen, S.-J., & Yeh, T.-L. (2005). *A common-path phase-shift interferometry surface plasmon imaging system.* Paper presented at the Biomedical Optics 2005.

Takeyasu, N., Tanaka, T., & Kawata, S. (2005). Metal deposition deep into microstructure by electroless plating. *Japanese journal of applied physics, 44*(8L), L1134.

Tan, Z., Li, X., Chen, Y., & Fan, P. (2014). Improving the sensitivity of fiber surface plasmon resonance sensor by filling liquid in a hollow core photonic crystal fiber. *Plasmonics, 9*(1), 167-173.

Tian, M., Lu, P., Chen, L., Lv, C., & Liu, D. (2012). All-solid D-shaped photonic fiber sensor based on surface plasmon resonance. *Optics Communications, 285*(6), 1550-1554.

Vial, A., Grimault, A.-S., Macías, D., Barchiesi, D., & de La Chapelle, M. L. (2005). Improved analytical fit of gold dispersion: Application to the modeling of extinction spectra with a finite-difference time-domain method. *Physical Review B, 71*(8), 085416.

Viale, P., Février, S., Gérôme, F., & Vilard, H. (2005). *Confinement loss computations in photonic crystal fibres using a novel perfectly matched layer design.* Paper presented at the Femlab Conference.

Vieweg, M., Gissibl, T., Pricking, S., Kuhlmey, B., Wu, D., Eggleton, B., & Giessen, H. (2010). Ultrafast nonlinear optofluidics in selectively liquid-filled photonic crystal fibers. *Optics express, 18*(24), 25232-25240.

Wang, Y. (1995). Voltage induced color selective absorption with surface plasmons. *Applied Physics Letters, 67*(19), 2759-2761.

West, P. R., Ishii, S., Naik, G. V., Emani, N. K., Shalaev, V. M., & Boltasseva, A. (2010). Searching for better plasmonic materials. *Laser & Photonics Reviews, 4*(6), 795-808.

White, T., Kuhlmey, B., McPhedran, R., Maystre, D., Renversez, G., De Sterke, C. M., & Botten, L. (2002). Multipole method for microstructured optical fibers. I. Formulation. *JOSA B, 19*(10), 2322-2330.

Wong, W. R., Krupin, O., Sekaran, S. D., Mahamd Adikan, F. R., & Berini, P. (2014). Serological diagnosis of dengue infection in blood plasma using long-range surface plasmon waveguides. *Analytical chemistry, 86*(3), 1735-1743.

Wu, C., Tse, M.-L. V., Liu, Z., Guan, B.-O., Lu, C., & Tam, H.-Y. (2013). In-line microfluidic refractometer based on C-shaped fiber assisted photonic crystal fiber Sagnac interferometer. *Optics letters, 38*(17), 3283-3286.

Wu, L., Chu, H., Koh, W., & Li, E. (2010). Highly sensitive graphene biosensors based on surface plasmon resonance. *Optics express, 18*(14), 14395-14400.

Wu, Y., Yao, B., Zhang, A., Rao, Y., Wang, Z., Cheng, Y., . . . Chiang, K. (2014). Graphene-coated microfiber Bragg grating for high-sensitivity gas sensing. *Optics letters, 39*(5), 1235-1237.

Yeh, P., Yariv, A., & Hong, C.-S. (1977). Electromagnetic propagation in periodic stratified media. I. General theory. *JOSA, 67*(4), 423-438.

Yu, X., Zhang, Y., Pan, S., Shum, P., Yan, M., Leviatan, Y., & Li, C. (2010). A selectively coated photonic crystal fiber based surface plasmon resonance sensor. *Journal of Optics, 12*(1), 015005.

Yuan, G., Gao, L., Chen, Y., Liu, X., Wang, J., & Wang, Z. (2014). Improvement of optical sensing performances of a double-slot-waveguide-based ring resonator

sensor on silicon-on-insulator platform. *Optik-International Journal for Light and Electron Optics, 125*(2), 850-854.

Zhang, P.-p., Yao, J.-q., Cui, H.-x., & Lu, Y. (2013). A surface plasmon resonance sensor based on a multi-core photonic crystal fiber. *Optoelectronics Letters, 9*, 342-345.

Zhao, Y., Deng, Z.-q., & Li, J. (2014). Photonic crystal fiber based surface plasmon resonance chemical sensors. *Sensors and Actuators B: Chemical, 202*, 557-567.

Zynio, S. A., Samoylov, A. V., Surovtseva, E. R., Mirsky, V. M., & Shirshov, Y. M. (2002). Bimetallic layers increase sensitivity of affinity sensors based on surface plasmon resonance. *Sensors, 2*(2), 62-70.

# LIST OF PUBLICATIONS

## Journal Papers:

➤ **Ahmmed A. Rifat,** G. Amouzad Mahdiraji, Rajib Ahmed, Desmond M. Chow , Y. M. Sua, Y. G. Shee, M. R. A. Adikan, "Copper-Graphene Based Photonic Crystal Fiber Plasmonic Biosensor", IEEE Photonics Journal, Issue: 1, vol: 8, 2016. (ISI-cited-Q1)

➤ **A. A. Rifat,** G. Amouzad Mahdiraji, Y. M. Sua, Y. G. Shee, Rajib Ahmed, Desmond M. Chow, F. R. Mahamd Adikan, "Surface Plasmon Resonance Photonic Crystal Fiber Biosensor: A Practical Sensing Approach", IEEE Photonics Technology Letters, Issue: 15, Vol. 27, pp: 1628-1631, 2015. (ISI-cited-Q1)

➤ **Ahmmed A. Rifat**, G. Amouzad Mahdiraji, Desmond M. Chow, Y. G. Shee, Rajib Ahmed, Desmond M. Chow, F. R. M. Adikan, "Photonic Crystal Fiber based Surface Plasmon Resonance Sensor with Selective Analyte Channels and Graphene-Silver Deposited Core", Sensors, Vol. 15, pp. 11499-11510, 2015. (ISI-cited-Q1)

➤ **Ahmmed A. Rifat,** G. Amouzad Mahdiraji, Y. M. Sua, Rajib Ahmed, Y. G. Shee, M. R. A. Adikan, "Highly Sensitive Multicore Flat Fiber Surface Plasmon Resonance Refractive Index Sensor", Optics Express (Accepted, in press). (ISI-cited-Q1)

## Proceeding/Conference Papers:

➤ **A. A. Rifat,** G. Amouzad Mahdiraji, Y. G. Shee, Md. Jubayer Shawan, F. R. Mahamd Adikan, "A Novel Photonic Crystal Fiber Biosensor Based on Surface Plasmon Resonance", 4th Photonics Global Conference (ICMAT-2015), 28 June - 03 July, 2015, Singapore.

➤ **A. A. Rifat,** G. A. Mahdiraji, Y.G. Shee, F.R.M. Adikan, "Flat Fiber Based Surface Plasmon Resonance Sensor", Siegman International School on Lasers: 2015, Organized by Max Planck Institute, Germany, 02-07 August, 2015 (Awarded partial travel grant from Optical Society of America (OSA) to attend this conference).

➤ **A. A. Rifat,** Ghafour Amouzad Mahdiraji, Y.G. Shee, F.R.M. Adikan, "Design of Dispersion Manage, Low Confinement Loss and High Nonlinearity Photonic Crystal Fiber for Communication Applications", 6th AUN/SEED-Net Regional Conference on Electrical Engineering, 4-5th March, 2014, Malaysia.